POLITECNICO DI MILANO

Scuola di Architettura Urbanistica Ingegneria delle Costruzioni

Ingegneria dei Sistemi Edilizi LM-24

FIBERS ORIENTATION AND MECHANICAL PERFORMANCE OF HPFRC IN 3D PRINTED MOLDS

Rapporteur: Prof. Liberato Ferrara

Supervisor: PhD Timothy Wangler

Master's thesis:

Nicholas Leomanni Matr.883957

Anno accademico: 2018/2019

ACKNOWLEDGMENTS

My first gratitude goes to Prof. Ing. Liberato Ferrara, without whom this thesis would not have life, for his confidence in proposing me a thesis in Zurich, I hope I did not disappoint his expectations. I am grateful to Dr. Wangler Timothy, a man of great wisdom and able to address me on the right way during my stay abroad. I thank Dr. Michele Griffa for welcoming me to EMPA and supporting me during all the difficulties encountered in fiber orientation analysis, and to Dr. Münch Beat for having had the ingenious intuition to obtain the results required in a record time. My gratitude goes to PhD. Nicolas Ruffray for his invaluable help during the optimization of the FRC mix design, and to PhD Andrei Mihail Jipa for contributing with the 3D printing of the molds. Also, I thank Dr. Robert Zboray and Dr. Thomas Lüthi for performing the required tomograms and Heinz Richner for introducing me to the lab and helping me to ground the specimen surface. My finally gratitude goes to all my family. Starting from my mother who made my abroad thesis possible, supporting me in the best way as a great woman can do. Then, my girlfriend Tanya who gave me courage to face the difficulties and to never give up. I thank everyone, uncles, grandmother and friends for being by my side during this personal growth.

RINGRAZIAMENTI

Il primo ringraziamento va al Prof. Ing. Liberato Ferrara, senza il quale questa tesi non avrebbe avuto origine, per la sua fiducia nel propormi una tesi a Zurigo, spero di non aver deluso le sue aspettative. Ringrazio il Dr. Wangler Timothy, uomo di grande saggezza e capace di indirizzarmi sulla via giusta durante il soggiorno all'estero. Ringrazio il Dr. Michele Griffa per avermi accolto all'EMPA e avermi sostenuto durante tutte le difficoltà riscontrate nel fiber orientation analysis, e a Dr. Münch Beat per aver avuto la geniale intuizione per ottenere i risultati richiesti in un tempo record. Ringrazio il PhD. Nicolas Ruffray per il suo aiuto prezioso durante l'ottimizzazione del mix design del FRC, e il PhD. Andrei Mihail Jipa per aver contribuito con la stampa delle molds. Inoltre, ringrazio Dr. Robert Zboray e Dr. Thomas Lüthi per aver eseguito i tomogrammi richiesti e Heinz Richner per avermi introdotto nel laboratorio aiutandomi a grounding la superficie dei campioni. Infine, ringrazio la mia famiglia. A partire da mia madre che ha reso possibile la tesi all'estero, sostenendomi nel migliore dei modi come una grande donna sa fare. Poi, la mia ragazza Tanya che mi ha dato coraggio nell'affrontare le difficoltà e a non mollare mai. Ringrazio tutti quanti, zii, nonna ed amici per essere stati sempre al mio fianco durante questa crescita personale.

ABSTRACT

Governing the dispersion and the orientation of fibres in concrete through a suitably balanced set of fresh state properties and a carefully designed casting procedure, is a feasible and cost-effective way to achieve a superior mechanical performance of fibre reinforced cementitious composites, which may be required by the intended application, even keeping the fibre content at relatively low values. The purpose of this work is to investigate how the fibers orientation induced through the 3D modeling of the formwork allows an increase in flexural strength in high-performance fiber-reinforced concretes. To achieve this, a series of 16 toothed parallelepiped specimens, divided by tooth height category, with a total height of 32mm, width of 116mm and length of 360mm were casted. The work was intended to verify whether the casting methods and the geometry (which was designed to "reproduce" the peculiarities of 3D printed elements). Initially, a detailed analysis which deals with the use of 3D modeling technology in the construction field, outlining its limits and advantages was carried out. Subsequently, a brief description of the characteristics of fiber reinforced concrete and its fields of application precedes the actual experience. In it takes place the journey that starts, as in all the recipes of a Michelin-starred restaurant, from the list of ingredients to create toothed parallelepiped samples in fiber-reinforced cement and continues with the method used to obtain the required results, up to the assembly of the food on the plate, in which the results will attract the reader's curiosity. Furthermore, it was explained how the modalities of the fresh concrete flow and the geometrical characteristics of the formwork induce a predetermined orientation of the fibers with which to govern them during the casting. To conclude, a report that bonds the orientation parameters and the bending resistant capacity of the specimens has been carefully found.

SOMMARIO

Governare la dispersione e l'orientamento delle fibre nel calcestruzzo attraverso un insieme opportunamente bilanciato di proprietà di stato fresco e una procedura di colata accuratamente progettata, è un modo fattibile ed economico per ottenere prestazioni meccaniche superiori di materiali compositi fibrorinforzati, che possono essere richiesti dall'applicazione prevista, mantenendo anche il contenuto di fibre a valori relativamente bassi. Lo scopo di questo lavoro è quello di studiare come l'orientamento delle fibre indotto attraverso la modellazione 3D della cassaforma consenta un aumento della resistenza alla flessione in calcestruzzi rinforzati con fibre ad alte prestazioni. Per ottenere ciò, sono stati scelti una serie di 16 campioni parallelepipedi a denti, divisi per categoria di altezza del dente, con un'altezza totale di 32 mm, larghezza di 116 mm e lunghezza di 360 mm. Il lavoro aveva lo scopo di verificare se i metodi di fusione e la geometria. In prima analisi è stata effettuata una dettagliata analisi sull'impiego di tecnologia di modellazione 3D nel campo delle costruzioni, delineando i suoi limiti e i vantaggi. Successivamente, una breve descrizione delle caratteristiche del fiber reinforced concrete e i suoi campi di applicazione precede l'esperienza vera e propria. In essa si svolge il viaggio che parte, come in tutte le ricette di un ristorante stellato Michelin, dall'elenco degli ingredienti per creare i campioni parallelepipedi dentellati in cemento fibrorinforzato e prosegue con il metodo utilizzato per ottenere i risultati richiesti, fino alla fase di assemblamento del cibo nel piatto, in cui i risultati attireranno la curiosità del lettore. Inoltre, è stato spiegato come le modalità del flusso fresco di calcestruzzo e le caratteristiche geometriche del cassero inducano un orientamento prestabilito delle fibre con il quale governarle in fase di getto. Per concludere, una relazione che lega i parametri di orientamento e la capacità resistente a flessione dei provini è stata accuratamente trovata.

TABLE OF CONTENTS

LIST OF FIGURES

LIST OF TABLES

LIST OF EQUATIONS

CHAPTER 1 - INTRODUCTION

In recent years, technology developments in the field of digital design and robotics, as well as in the modeling and design of cement materials have made great strides, allowing the introduction of new automated construction methods. In this line of thinking, in which cement is employed as a building material, the techniques and technologies of Digital Fabrication with Concrete (DFC) have been introduced. However, since the characteristics of the DFC are very different from those of conventional manufacturing techniques, it is necessary a rethinking, or rather a reconstruct and reorganize of all the production phases and designs that previously perfectly suited a conventional method, but that now require of a makeover.

The research study of this master thesis will initially deal with the state of the art of the last decades, focusing on the combination of conventional reinforcement method and the application of DFC with integrated reinforcement in various ongoing research activities, outlining the technical challenges and the economic and the environmental potential of the DFC. Subsequently, the Fiber Reinforced Concrete (FRC) will be explained in its properties and characteristics of the fibers in relation to the cement material according to applications. Furthermore, a brief introduction to 3D printing and its two main printing methods will be given. In the second part, the materials and methods used to perform the experimental work will be discussed. First of all, the materials will be listed, giving more information about the superplasticizer and the steel fibers used, as they are considered the main factors, together with cement, to obtain a good mix design. The latter, in fact, will be optimized with the purpose of obtaining a workability and homogeneity of the cement mixture required. Once

the formworks have been obtained using 3D printing technology, different types of specimens will be submitted to the X-ray analysis. Finally, the fiber orientation data processing according to the polar coordinates will precede the three-point flexural tests.

The main purpose of this thesis is to uncover a relationship between the orientation of the fibers and the mechanical performance of the specimens in terms of flexural strength. Furthermore, the variation of the density of the fibers within the sample will be highlighted, the role that the fresh cement casting plays with the orientation of the fibers and observe how they are oriented with the choice of a mold form of the predetermined formwork according to the phenomenon of the "wall effect".

CHAPTER 2 - STATE OF THE ART. 3D-PRINTING AND FIBERS

2.1 Introduction

Over the last decade, developments in digital design and modelling, robotics, as well as in the engineering of cementitious materials, have allowed the introduction of new automated construction methods. Consequently, an ensemble of innovative fabrication technologies is now in continuous development all over the world.
Many of them are not easy to classify and are identified by a range of generalized names. Generally, each of them shares the following characteristic:

- introduction of new functionalities;
- introduction of bespoke fabrication;
- a high degree of freedom for shapes;
- robotized material placement;
- lack of conventional formwork system.

For the purpose of discussing the new technologies or techniques having concrete as the main construction material, they are collectively identified as Digital Fabrication with Concrete (DFC). However, since the characteristics of DFC are quite different from those of conventional fabrication techniques, it is necessary to reconstruct and reorganize the manufacturing, product material design, manufacturing process, assembly in a structural system and performance evaluation of the final product starting from building components up to full-scale houses. In concrete constructions a key point is that traditional cementitious

materials have insufficient tensile capacity and ductility and for this reason their implementation is made possible in combination with tensile reinforcement. Reinforcement concepts and principles implemented in conventional concrete constructions are not generally applicable to DFC. Therefore, a rethinking of the fundamental concepts of reinforcement technology, dimensioning and detailing is required in order to open the way for market applications of digitally fabricated concrete structures. The analysis of the first part of the state of the art will focus on an in-depth description of Digital Fabrication with Concrete (DFC). Starting from the combination with the conventional reinforcement method and the application of DFC with integrated reinforcement in various ongoing research activities, up to outline the technical challenges and economic-environmental potential. In the second part, Fiber Reinforced Concrete (FRC) will be treated in its properties, current legislation and the various experiences and researches that have highlighted the peculiarities of the use of this material. Finally, the possibility of orienting the fibers through rheology or the magnetic field by introducing the application of 3D-printing in the thesis experience will be discussed.

2.2 Digital Fabrication with Concrete (DFC)

Talking about Digital Fabrication with Concrete (DFC) it is crucial to recognize that replicating existing schemes into new technologies can be potentially detrimental for the economy of the new technology as well as structural performance and construction speed. Therefore, it is interesting to investigate how digital fabrication can improve the performance of concrete construction and define new design criteria appropriate for each specific DFC technique. In order to classify the criteria, it will be necessary to expose the advantages and disadvantages of current reinforcement technologies. Nowadays, the legislation requires using a “minimum reinforcement” inside the concrete. This is due to two main factors: the tensile strength, roughly equal to 10% of the compression strength, that is neglected during structural calculations, and the shrinkage phenomenon, which involves not negligible initial stresses. In addition, reinforcement avoids brittle failures at cracking, ensure sufficiently ductile behavior to enable stress redistribution (concerning bearing capacity), limit deformations and crack widths under service conditions and thus

contribute to provide the required durability. Conventional reinforcement can be categorized as internal or external, metallic or non-metallic, and passive or prestressed (active). With the use of steel bars, yield strengths of 450-500 MPa are achieved, while high strength steel wires or strands are typically used as prestressed reinforcement, with tensile strengths in the order of 1500–1800 MPa. Over the last decades, the use of fibers replacing or complementing conventional reinforcement has become more frequent. However, compared to conventional reinforced concrete (RC), fibre reinforced concrete (FRC) is limited in terms of strength and, more importantly, of ductility. Ultra-high-performance fibre reinforced concretes (UHPFRC) represent the cutting edge in terms of achievable strain hardening post-cracking behaviour, but its use is so far restricted to special, typically precast applications due to the elevated costs and complex handling on site. The technological development, in terms of effective fibre incorporation in the cementitious matrices, has mainly considered the control of distribution and orientation of fibers in the fresh and hardened material. Given that this technological aspect might be difficult to control in many on-site situations, the use of FRC has been typically limited to applications with no primary structural function such as industrial floors. In addition to the mechanical and technological limitations related to the FRC material itself, the major barrier to the widespread use of FRCs in structural applications is the limited coverage of methodology and applications in design codes, only recent fib Model Code 2010 has provided the first consistent set of design rules applicable to this category of advanced cement based materials.

In terms of reinforcement installation, available methods are coupled with conventional concrete casting processes, either for in situ or prefabricated reinforced concrete structures. At casting, the concrete is filled into the formwork from top to bottom in layers, being compacted using immersion vibrators or vibrating tables.

In recent decades, self-compacting concrete (SCC) which does not require vibration for its consolidation has found a more widespread application, especially in the use of elements with a large amount of reinforcement. After this general overview of conventional techniques typically adopted, it is evident that the fundamental mechanical behavior of digitally fabricated RC elements will not differ from conventionally built RC. Moreover, the design methods based on mechanical models are applicable to additively manufactured elements, as well provided that the models are enhanced to account for fabrication method-

specific effects (anisotropy, shape-related mechanical effects, and weak layers). However, many current design provisions are based on semi-empirical models, calibrated on experimental testing of traditional RC elements. Such models need to be revised and adapted to fit the mechanical performance of digitally fabricated elements, or even abandoned for some technologies since empirical models will never be able to cover the entire range of complex geometries achievable by digital fabrication. Below are listed several ongoing research activities related to DFC with integrated reinforcement.

2.2.1 Smart dynamic casting

Smart Dynamic Casting (SDC) is a robotic prefabrication technique for non-standard concrete structures developed at ETH Zurich that extends the slip-forming technology using either a free slipping trajectory (Fig. 1) or flexible actuated formworks to produce variable cross sections and geometries (Fig. 2 and 3). SDC technology allows the digital fabrication of complex column structures in a continuous casting process with similar mechanical performances as conventionally built structures, even in cases where reinforcement is required. Hence, this is an example of a DFC process in which the reinforcement issue can be addressed by standard technologies and design processes, following similar lines as in conventional construction. Currently, the reinforcement integrated in the SDC technique is fabricated before concrete casting using three-dimensional numerically controlled bending processes, which allow applying standard and inexpensive deformed steel bars to complex digitally fabricated structures. This technology has been used for the production of a large number of variable cross-section 3 m tall mullions for the DFAB HOUSE in the NEST building at Empa in Dübendorf, Switzerland. In this application, the architectural design concept required a variable spacing between the mullions, leading to different structural requirements for each mullion, including transverse loading by wind pressure and suction.

Figure 1, 2 and 3 – Different uses of slip-forming technology

2.2.2 Mesh mould

Mesh Mould (MM) is also a digital fabrication technique developed at ETH Zurich, in which the reinforcement and formwork production are unified in a robotically controlled system. In MM, an industrial robot ("in-situ fabricator") equipped with a specially designed end-effector automatically fabricates on site a dense, three-dimensional welded reinforcement mesh (Fig. 4), currently designed using conventional structural concrete design specifications. This double side fine mesh is infilled with a special concrete mix that achieves sufficient compaction without flowing out the mesh and is subsequently finished with a cover layer to serve as a freeform RC structural element. An analogy could be made with ferrocement technology conceived and promoted by Pier Luigi Nervi, in which optimum complex structural shapes can be produced without formwork. As in the SDC technique, concrete is continuously cast in the core of the MM structure, reducing the potential layering issues inherent to other digital fabrication processes. MM uses conventional deformed bars in the mesh production with a grid spacing of around 40 mm, currently limited to 6mm and 4.5mm diameter respectively in each direction because of the bending, cutting and welding capabilities of the end effector. The mesh spacing varies depending on the mechanical requirements and the local curvature. The use of FRC to infill

the mesh is a complementary reinforcement that has been proven to enhance the strength of MM elements and reduces concrete flow out of the mesh.

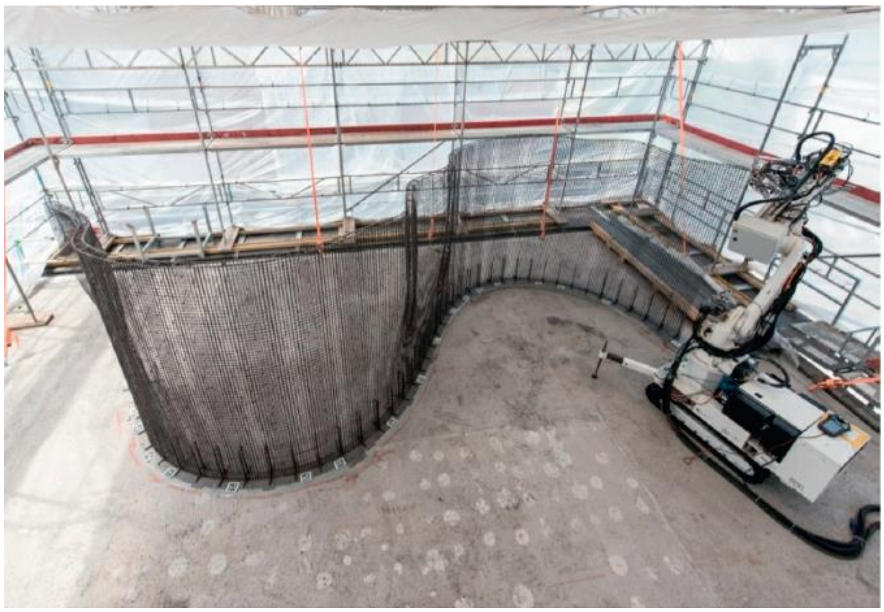

Figure 4 – Production of 14m long mesh for a double curved load bearing wall for the DFAB HOUSE, NEST building at Empa in Dübendorf, Switzerland

2.2.3 External reinforcement arrangement

The main scope of the external reinforcement arrangement approach is the manufacturing of steel rebar/tendon reinforced concrete (RC) members using DFC technology of concrete without interfering with reinforcement during fabrication. The approach is based on the idea that a RC member beam can be ideally cut into several "segments" which are printed separately using a specific digital fabrication technology for concrete and, in a second stage, assembled with a steel reinforcing system to create the final structural element. Each concrete segment of the structural member can be manufactured through the width direction or longitudinal axis of the member itself. Once the number and dimensions of segments are defined, each concrete segment can be designed to accomplish weight reduction targets and proper mechanical performances related to the internal forces acting on the structural element. To this end, concrete segments can be topologically optimized with a number of voids, to save material while still guaranteeing the required mechanical performances. In addition, functional voids can be foreseen before the printing process, that can be used as

specific geometrical detail to accommodate sensors or tendons. The DFC technological strategy consists in printing several concrete segments, each one designed according to a specific mechanical model to resist variable bending moments and shear forces. Besides the printing stage, this approach requires the beam segments to be designed in an integrated manner with the reinforcement system in order to guarantee proper tensile reinforcement and to lock the segments in a single continuous element. Following an example of reinforcement scheme adopted in the prototypes presented by Asprone et al. [1] which consists in two separate external steel reinforcing layers installed on both sides of the beams connected each other through orthogonal threated rods (Fig. 5). The latter are positioned into the holes of each concrete segment and secured with a high strength low-viscosity cement-based mortar. Asprone implemented, as one of the possible mechanical optimization strategies, the classical strut-and-tie model for the design of a straight 3.0 m long RC beam characterized by a rectangular cross-section having 0,20m and 0,45m of width and height, respectively (Fig. 6).

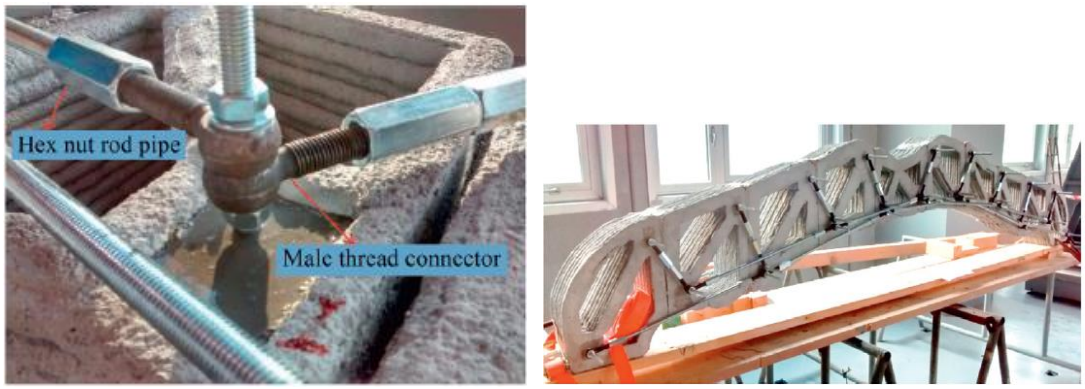

Figure 5 and 6 – On the left external steel reinforcement connection details and on the right variable cross-section RC beams obtained through the DFC technique of external reinforcement arrangement.

If prestressing external reinforcement is used, strategies and detail solutions known from conventional externally prestressed structures, particularly precast segmental bridges, can be applied, paying specific attention to creep and shrinkage behaviour. Following the same structural design principle, a real scale example is the pedestrian and bicycle bridge developed at the Eindhoven University of Technology, which was recently placed in Gemert, the Netherlands. It is constructed from 6 segments, printed to a height of 99 cm each. After printing, the segments were rotated by 90°, positioned next to each other and connected by post-tensioned prestressing tendons that were anchored in conventional cast blocks. An epoxy adhesive was applied to the seams.

2.2.4 3D printed concrete formworks

In a limited number of projects, a different strategy has been adopted, for example the 3D printed concrete as lost formwork for conventional reinforced concrete. In this case, DFC is unreinforced, typically not structurally active and the reinforcement is placed during manufacturing in a "passive" way. The inclusion of passive reinforcement using conventional steel elements represents a more straightforward approach than the above-described technologies. This approach has been combined with several DFC techniques currently available on the market. A typical representative example is the production of RC walls using contour crafting technique in which custom-made reinforcement ties are manually inserted between layers with a spacing of 30 cm and 13 cm in the horizontal and vertical direction, respectively. Even though this approach allows for an easy and, probably, cost-effective implementation of reinforcement, some limitations appear to be not negligible from the structural design point of view. Indeed, one of these concerns about the interface between printed and cast concrete, structural efficiency, and flexibility. These aspects restrict the range of structural applications to those characterized by simple loading conditions or, in general, to those not requiring complex resistant mechanisms, such as the production of vertical elements subjected to compression loads.

Figure 7 – Digital manufacturing of a free-shaped wall-like concrete bench using the 'Concrete Printing' approach

2.2.5 Printable fibre reinforced concrete

The addition of fibres to the 3D printable concrete matrix is an obvious solution strategy that has been explored on a very small scale by Hambach and Volkmer [2], who added 3–6mm basalt, glass and carbon fibres to a printable mixture, and Panda [3], who compared glass fibres of different lengths (3, 6 and 8 mm) and varying the volume percentage of fibres (vol%). The studies reported a significant increase in flexural tensile strength as well as an orientation effect of the fibres in the direction of the filament flow.

2.2.6 3D construction printing with directly entrained reinforcement cable

The most advanced concept currently under development at the Eindhoven University of Technology, is the direct in-print entrainment of reinforcement cable into the concrete filament during printing. This concept builds on an idea presented by Khoshnevis [4] that included a reinforcement wire coil that would not only provide longitudinal tensile strength, but also ductility though the layer interfaces, as half of the coil sticks out of the preceding layer.In this concept, the reinforcement cable should be sufficiently strong and ductile, but also highly flexible to allow it to follow all 3D freeform lines that can be produced with the concrete filament. High strength steel cables for synchronous belts provide such a combination of properties (Fig. 8). Several experiments have been conducted, using 3 types of cable (A, B and C) with ultimate tensile loads of F_{uk} =420, 1190, and 1925 N, respectively, and diameters ranging from 0.63 to 1.20 mm, from which significant ductility could be achieved.

Figure 8 – Printing with the Reinforcement Entraining Device (RED) to introduce a steel cable into the concrete layer

In a more extensive subsequent study Bos [5], the pull-out behaviour of the cables in cast and printed concrete was investigated (Fig. 9). The bond strength in cast concrete was 1.5 to 3 times higher than in printed concrete. The bond in printed concrete was towards the lower bound of what would be expected from smooth conventional reinforcement bars. From the results, anchorage lengths were calculated, and dedicated series of beams were designed so that the ultimate failure moment should exceed the cracking moment, $M_u > M_{cr}$. The tests on the cable beams, nonetheless, confirmed the applicability of common calculation methods for RC. The variability of the bond behaviour between cables and the concrete matrix highlighted the major role of the production conditions for the effective implementation of this technique, including contour length, drying stage, self-weight of the structural build up, concrete matrix compaction, and geometry effects. The effective control of these process-related aspects is required to achieve the successful scale up of structural elements manufactured with 3DCP using directly entrained reinforcement cable.

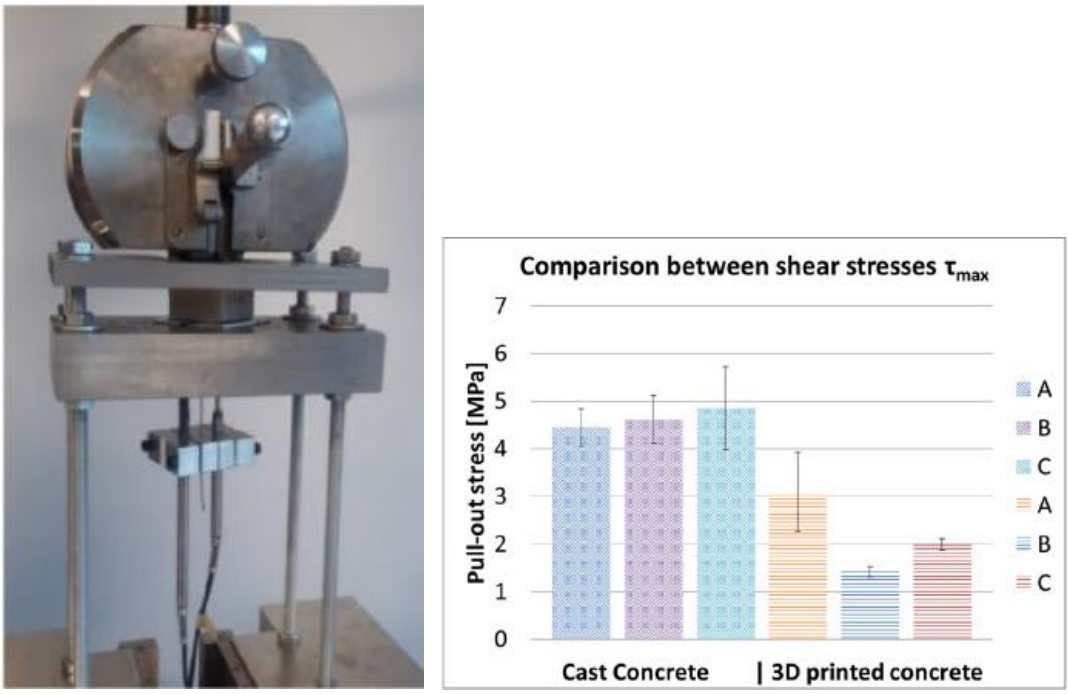

Figure 9 – Pull-out test on concrete with embedded reinforcement cable: on the left experimental set-up with printed specimen; on the right comparison of average bond strengths in cast and printed concrete for 3 types of cables

2.2.7 Technical challenges

A major current obstacle to a broad application of 3D printing in construction industries is the very limited material palette currently available in practice. Many current showcases are not based on high-quality materials required to reach a reasonable service live in natural or industrial exposure conditions. When checking material performance in some showcases in more detail, striking insufficient performance can sometimes be noticed. Moreover, the issue of appropriate curing of 3D printed elements or structures, in the absence of formwork from the beginning, remains a technical challenge requiring further optimization. Intense work on admixture development to get the desired material performance has been done recently. Hence, the detailed control of rheological properties and the constantly evolving technology allow to develop a structural improvement of the building element. Although these developments are promising and have already been implemented on the field, they are quite sensitive to the physical and chemical composition of the mix. A change in the cement type, or aggregate nature might require a new adaptation of the concrete mix design and admixture type. However, a more robust approach is to actively control material rheology and stiffening in real time during production, as currently studied in the ERC Advanced

Grant ‘SmartCast’ project [7]. The main objective of ‘SmartCast’ is to develop concrete with actively controllable rheology and stiffening, in order to automate and optimize concrete casting operations. While 3D printing is offering a totally new production method, fundamental scientific knowledge on cementitious materials is not becoming outdated. On the contrary, it will even become more important in view of correctly understanding the consequences of the different production conditions compared to traditional formwork-based casting operations. Bulk material properties will follow the same fundamental material laws. However, in a 3D printed structure or element, the role of interfaces will become increasingly important. Between successive layers, an interface zone is present, with properties depending on time delay between deposition of layers. These interfaces will influence the mechanical performance, most prominently the bond behaviour, as well as transport and durability behaviours. The anisotropic nature of 3D printed concrete is challenging current approaches for structural and durability design, as well as current practices for performance testing [8]. Current structural and durability design codes consider the concrete as a homogeneous material. For 3D printed concrete elements, this is no longer the case, due to the layered concept with more porous and weaker interfaces, and anisotropic behaviour. In summary, in case of 3D printed concrete based on the principle of additive manufacturing, current structural and durability design codes will have to be revised to consider the anisotropic behaviour. In addition, current concepts of compliance control or performance testing will also require updating. On the short term, the lack of appropriate design codes and performance testing protocols will hinder the breakthrough of digital manufacturing in concrete industry. Finally, added functionality can also be achieved by DFC through purposeful choice of material used, e.g. cementitious materials with very low thermal conductivity such as LWAC, foam concrete, concrete with wood as additive (see Fig. 10) and thermally activated concrete. In future settings, the smart deposition of materials with particular mechanical properties could also include options for internal curior self-healing where needed. Use of multiple materials, each responsible for specific function such as compression load-bearing, tensile load-bearing and insulation has been demonstrated and is envisioned to offer plethora of opportunities to digitally fabricate smart structures. Multi-material structures with load bearing concrete as outer shell and insulating material as infill are also envisioned to reach marketability with DFC in near future. However, this fine intermixing of different materials raise the question of recyclability [9].

Whether multi-functionality should be achieved through a hybridization at the material level or at structural level is a fundamental question for the environmental performance of the final building element.

Figure 10 – 3D printed LWC with wood as filler

2.2.8 Economic potential

Construction industry in European Union constitutes 9.7% of the gross domestic product and provides 6.6% of Europe's total employment [10]. Currently, developed countries suffer from stagnating or in fact in some countries decreasing productivity. The causes are numerous and include factors such as the resistance to introduce changes in a highly traditional sector, low industrialization of construction processes, poor collaboration and data interoperability, and high levels of turnover, which make it difficult to implement new methods. In general, the conservative construction industry invests relatively little in research and development. This holds true also for countries with very good economic situation. Relatively low profit margins for construction companies could be the primary reason for this [11]. As a consequence, construction processes have almost not changed during the past decades. The revolutionary potential of DFC offers a logical evolution from the already well developed Computer Aided Design (CAD) tools to automated construction, thus making construction a fully digitalized process. A reduction of construction times and the improvement of the quality and cost by the integration of digital design and construction activities can significantly increase the productivity of the sector [12]. Digitalization of processes ranging from design to fabrication may also reduce the potential for errors and

aid enhanced management of the construction process. Digital data managed through Building Information Management (BIM) will be fully utilized from planning to production and even further to maintenance, rehabilitation and recycling. A recent study developed by García de Soto et al. [15] investigated the effects of DFC on productivity by analyzing the cost and time required for the construction of a robotically-fabricated concrete wall with different degrees of shape complexity. The results of the analysis demonstrated that additive digital fabrication provides higher productivity over conventional construction when complex concrete structures are built. It has been shown that there is no additional cost derived from robotic fabrication if the complexity of the wall geometry increases. For placing concrete, especially the ready-mix type, formworks are commonly needed. The use of formworks leads to high material, labor and machinery costs. Formwork costs amount up to 28 % according to Schmitt [13] but can be in some cases half of total concrete structure cost. In addition, usage of formworks results in considerable time delays and negative environmental impact. The problematic role of formwork is even more significant in case of constructing unique objects or complex structures, where the use of formwork is on the one hand challenging and on the other hand expensive plus time-consuming. In case of DFC, with help of guaranteed rheological properties and control of their evolution in time, placed cementitious material can retain its shape without any formwork. This can lead to substantial cost reduction. Furthermore, almost-unlimited geometrical freedom enabled by DFC also provides the potential that costs in case of complex structures will not increase or even decrease in comparison to the conventional construction. In other words, the costs of structures manufactured by means of DFC are expected to become largely complexity independent. Subjected to qualitative scrutiny, the four broad components of any construction process are:

- labor;
- machinery;
- material;
- design and planning costs (3D models, BIM).

In case of DFC, total labor costs will be significantly lower than that of conventional construction [14]. The costs of machinery, in principal, depend on the DFC approach and the applied techniques. Three major sub-processes can be identified in all DFC technologies:

- transporting material to the print-head;
- precise positioning of the print-head;
- extrusion or activation of parts of the desired structure's component.

Machinery used for these sub-processes varies depending on DFC technique and so are the costs. In a different perspective, the machinery used for DFC can be categorized into unconventional construction equipment (UCE) and conventional construction equipment (CCE). The more CCEs are incorporated into machinery of DFC sub-processes the faster will be the industrial acceptance, the lower will be the total costs of DFC and the higher will be the sustainability. On the one hand, the material costs for DFC can be lower than those of conventional construction due to topology optimization, avoidance of over-engineering and waste material reduction. On the other hand, they could also be higher in case of DFC due to utilization of expensive, very fine additions such as nano-clay, nano-silica and special chemical admixtures. The costs for the final design and planning, which includes 3D modelling BIM are expected to gradually decrease considering the advancements in related fields. This decrease in costs is particularly likely in case of large-scale implementation. The high reusability of digital data will eventually render the costs for planning in case of DFC negligible in comparison with conventional construction. However, based on a real scale DFC wall constructed in the NEST building (Switzerland), García de Soto et al. [15] estimated the cost structure of this case study. Specifically, the study compared the cost structure of straight and double-curved reinforced concrete walls constructed with robotic fabrication techniques and conventionally. The allocation of the different costs for the different wall types and construction methods is shown in fig.11. It can be observed that the main variations occur in the construction of the conventional concrete walls, and they are caused by the high cost of the formwork needed for double-curved walls. The relative cost of materials is more than tripled when building the complex wall in the conventional way. In contrast, the variations between straight and double-curved robotically fabricated concrete walls are negligible. Therefore, this analysis shows that the cost structure of DFC processes differs significantly when compared to conventional construction.

	Labor	Material	Equipment
Straight wall/conventional	56%	23%	21%
Straight wall/robot	36%	45%	18%
Double-curved/conventional	22%	75%	3%
Double-curved/robot	38%	44%	18%

Figure 11 – Allocation of labor, material and equipment costs for different types of concrete wall construction. (Based on García de Soto [15])

DFC, like other revolutionary innovations, will change the stakeholders in the construction sector. I-Tech companies will have a pronounced role by using BIM and other digital tools as a primary aspect. Furthermore, new start-ups and existing robotic and automation companies potentially enter and become large stakeholders in DFC. The inevitable changes for the personnel with emergence of DFC are also noteworthy. The implementation of digital fabrication in the construction sector will potentially affect the simplest and repetitive manual tasks. As a result, the less qualified jobs may be automated. The number of low-skilled workers will potentially decrease in favour of an increase of high-skilled specialized workers. As a result, highly skilled robotics, programming and concrete technology experts will be the backbone of DFC. Fig. 12 illustrates a simplified representation of the potential evolution of the construction workflow due to the implementation of digital fabrication. In a short term phase or “digitalization” phase, it is expected a partial implementation of digital technologies in construction. During the design phase, the engineering knowledge is embedded in a central software allowing the architect to use this knowledge to design the building. During the construction process, a digital fabrication specialist takes control of the on-site robotic fabrication, extending his/her design knowledge to the construction process. Consequently, the number of on-site conventional construction tasks decreases, and also the construction workers intended for them. The conventional role of designers and project managers will potentially evolve to a consultant, co-creator and collaborator, making digital fabrication technologies accessible to users and helping them during the construction process. Related research in other fields such as presented the role of the designer as a communication facilitator between users and technology developers in a multidisciplinary team, understanding their needs and sharing technological possibilities.

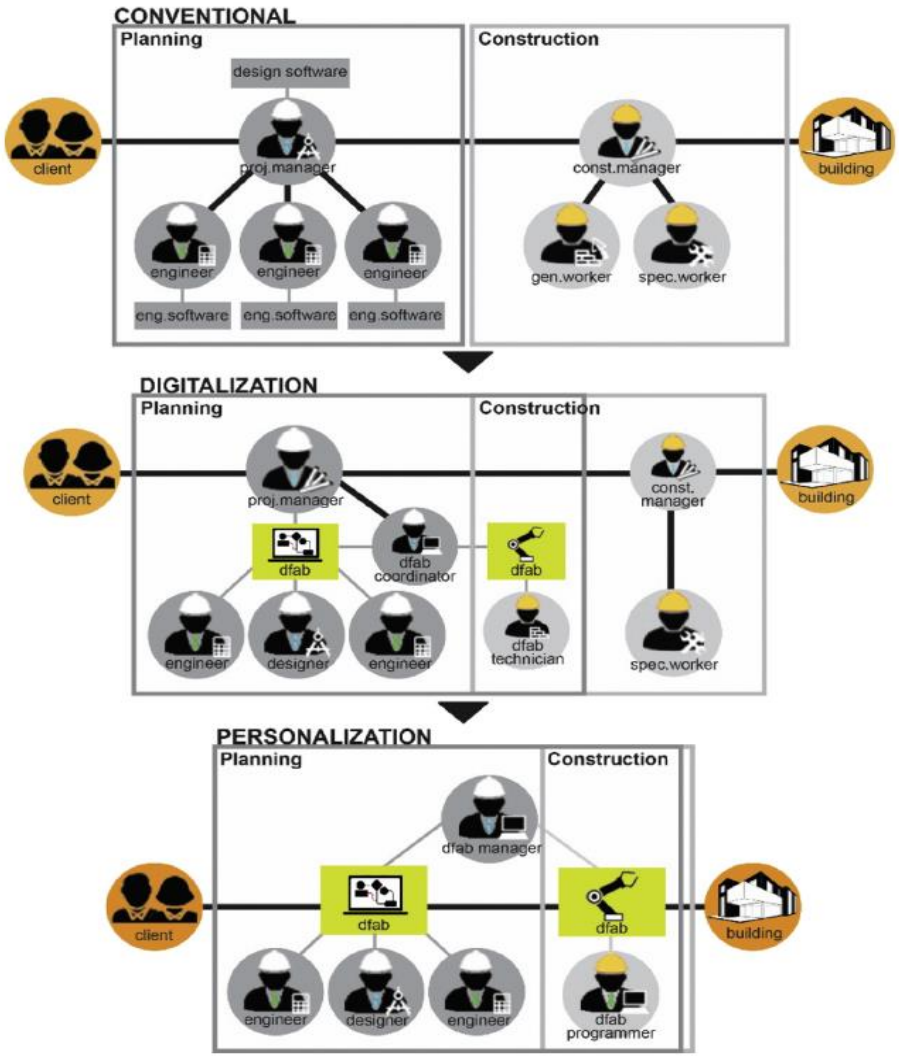

Figure 12 – Evolution of the construction workflow derived from the digitalization of the construction industry, including current, short-term and long-term state [15]

2.2.9 Environmental potential

The construction sector is responsible for high environmental impacts worldwide, such as 40% energy consumption, 40% solid waste generation, 38% GHG emissions and 12% water depletion [16]. Society's increasing concern about sustainability is inducing the emergence of innovative construction processes to overcome the high environmental impacts caused by traditional construction. Additive manufacturing processes have been associated with a cost-effective fabrication that lowers energy use, resource demands and CO2 emissions over the product life cycle. As the interest in 3D printing grows, potential large-scale applications are emerging in construction. According to Labonnote [17], additive construction processes highlight a significant potential to reduce material though topology optimization, produce complex geometries without supporting structures and integrate multi-functionality in building elements, which is not possible with conventional construction techniques. However, in order to achieve a recognizably sustainable

construction process, life-cycle assessments (LCA) must be performed to guide the design of 3D printed structures. Agustí-Juan and Habert [18] performed an environmental evaluation of larger process where three digitally fabricated building elements and their comparison with conventional construction were studied. The results of the evaluation highlighted the low relative impact of the digital construction process compared to the impact of building materials production. Looking specifically at additive manufacturing with concrete materials, Agustí-Juan showed that the production of robotic arm, the production and recycling of the lithium batteries used to operate the robots as well as the electricity demand during the fabrication contribute marginally to the overall environmental impact of a digitally fabricated wall. Moreover, the analysis confirmed that most of the impacts come from the amount and type of building materials used. These results are not surprising as in conventional construction, published studies have already shown that the construction phase has a very small contribution to the life-cycle impact of buildings. Specifically, Hong et al. [19] and Junnila et al. [20] showed that direct emissions derived from on-site construction account for approximately 2% of the overall life cycle emissions. Recent developments in computer-aided design and additive fabrication in architecture demonstrate strong potential to construct customized complex structures. However, a gap has emerged between the possibilities offered by architectural design and the reality of the building industry. Non-standard geometries in construction require the planning and fabrication of complex and labour-intensive rebar geometries and formworks that are not easy to fabricate with current construction techniques. As a result, architectural design is often constrained to standard geometries to reduce costs and enable the reuse of formworks, especially in concrete construction. According to Labonnote and Rüther [21], additive construction processes offer the possibility to produce non-standard geometries at no additional cost. The more complex the structure, the more profitable the use of additive construction. In contrast, additive manufacturing technologies could be less cost-effective for standard construction. Focusing specifically on digital concrete, Agustí-Juan [22] analyzed the environmental performance of reinforced concrete walls with different levels of complexity constructed with additive robotic fabrication techniques and compared them with similar structures that would have been built with conventional techniques. The results of the environmental evaluation confirmed that digital fabrication brings high environmental benefits compared to conventional construction for structures with a high degree of shape complexity. As shown in Fig. 13, the environmental impact of the digitally fabricated wall does not grow with the uniqueness and complexity of the architectural geometry. Additional shape complexity is achieved without additional environmental costs, so the potential benefit of digital fabrication increases proportionally to the degree of complexity of the architectural geometry. Digital fabrication can facilitate the production of elements with higher shape complexity without increasing the environmental costs. This statement contradicts what is usually observed in conventional construction, where increasing complexity leads to a higher use of resources, construction waste and delays in the construction process [23].

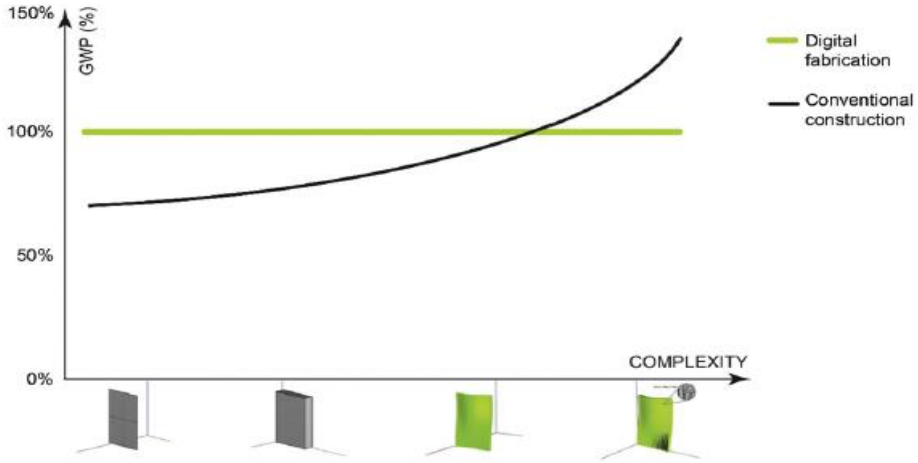

Figure 13 – Complexity related environmental advantage of digital fabrication vs. conventional construction. The environmental impact is expressed by the percentage of Global Warming Potential (kg CO_2) per m^2 of concrete wall (based on Agustí-Juan [22])

Novel computational approaches integrate structural optimization in form-finding design, offering new possibilities of formal expression and addressing resource efficiency in architecture [24], see Fig. 14. Several publications have pointed out the potential of additive construction techniques to reduce the use of material through structural optimization. For instance, Wangler [25] expected high sustainable benefits due to a more efficient design achieved by placing material only where it is structurally needed. Labonnote [17] and Hack [26] specified the potential of structurally optimized nonstandard geometries to bring material savings and weight reduction in load bearing applications. However, the production and optimization of complex concrete structures through digital fabrication methods often relies on high contents of cement. High-performance concrete ensures early strength and buildability without the need for coarse aggregates, the use of which is limited when thin structures such as the one usually manufactured by 3D printing are produced. As the environmental impact per cubic meter of concrete increases by augmenting cement content, the volume reduction must be even more effective [27].

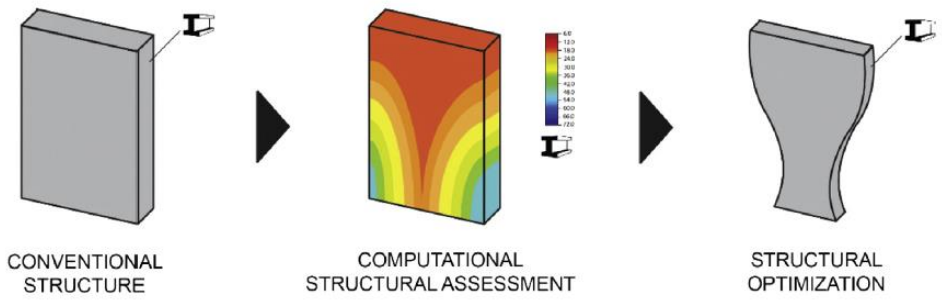

Figure 14 – Complexity related material optimization using computational structural analysis

The second strategy to efficiently use the benefit of a higher complexity without additional cost is to use complex forms to achieve multifunctionality (Fig. 15). Published literature on additive manufacturing applied to construction agree indeed on the potential of digital technologies to facilitate the integration of multi-functionality in building elements [28]. One can distinguish two cases. First, the integration of services such as piping, insulation or electrical facilities in the structure often requires complex geometries. Second, the complex structure can provide a secondary function through its shape, which will save an additional building component that would have provided this function. Integrated design can save building materials during production, associated with reductions in costs and environmental impacts. Nevertheless, environmental emissions are not just produced during the construction phase but also during the service life and a functional hybridization may increase the difficulty of retrofitting a building during its life cycle and increase replacement rates for building elements. The design of hybrid structures should be flexible enough to enable maintenance of certain components without influencing the service life of the whole element. Moreover, the functions integrated should be carefully chosen to avoid functions with a too short service life associated in elements that will have to last long. A reduction in the lifetime of the structure would result in high replacement rates, which increase life-cycle impacts.

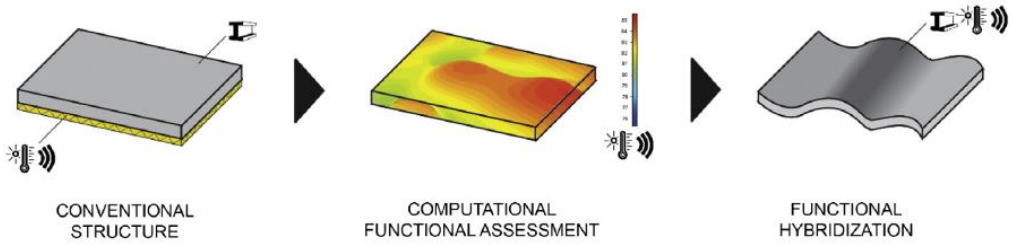

Figure 15 – Complexity related material optimization through functional hybridization

2.3 Methods and reinforcement in the 3D printed concrete

3D construction uses additive manufacturing techniques, which means objects are constructed by adding layers of material. Conventional approaches to construction involve casting concrete into a mould. But additive construction combines digital technology and new insights from materials technology to allow free-form construction without the use of formwork. Eliminating the cost of formwork is the major economic driver of 3D concrete printing. Built using materials such as timber, formwork accounts for about 60% of the total cost of concrete construction. It's also a significant source of waste, given that it is discarded

sooner or later. According to a 2011 study by Oluwafemi O. Omotayo, Samuel Lambe Akingbonmire [29], the construction industry generates 80% of total worldwide waste. Pouring concrete into formwork also limits the creativity of architects to build unique shapes, unless very high costs are paid for bespoke formwork. Free-form additive construction could enhance architectural expression. The cost of producing a structural component would not be tied to the shape, so construction could be freed from the rectangular designs that are so familiar in current building architecture. One of the most promising methods of concrete 3D printing is called Contour Crafting (CC) and has been developed at the University of Southern California, USA. This technology uses the extrusion-based technique to extrude two layers of cementitious mixture to build a vertical concrete formwork. Custom-made reinforcement ties are manually inserted between layers (at every 30 cm horizontally and 13 cm vertically) while the CC machine is constantly extruding the layers. Trowel-like fins are attached to the print head to create smooth extruded surfaces. Once the extruded formwork is completed, concrete is then manually poured to a height of 13 cm and a second batch is poured on top of the first batch after one hour. A one-hour delay batch is to control the lateral pressure of the concrete by allowing it to partially cure and harden. A concrete wall form fabricated by the CC machine is shown in the following figure.

Figure 16 – A concrete wall form fabricated by the CC machine with custom-made reinforcement ties manually inserted between layers[30]

The chief advantages of the CC technology are the superior surface finish and the greatly enhanced speed of fabrication. Other key advantage of CC is possibility of integration with other robotics methods for installing internal components such as pipes, electrical

conductors, and reinforcement modules to enhance mechanical property. The CC technology currently produces vertical elements largely in compression. When a doorway or window is required a lintel is placed to bridge the gap and the wall can be placed above.

Therefore, it avoids the cantilever problem. Gosselin et al. [30] reported the following drawbacks for the CC technology:

- this technology is limited to vertical extrusion, hence yielding 2.5D topologies (vertical extension of a planar shape);
- the initial formwork and trowel system can be rather complex to implement for production, depending on the size and shape of the object being printed;
- the interrupted sequential casting of concrete within the formwork due to hydrostatic pressure and weak mechanical properties of the extruded concrete may result in weakened interfacial zones between the layers

Another technology using the concrete as a building material is the "Concrete Printing technology" developed by a team at Loughborough University in the United Kingdom. This technology also uses the extrusion-based technique and to some extent is similar to the CC technology. However, the Concrete Printing technology has been developed to retain 3D freedom and has a smaller resolution of deposition, which allows for greater control of internal and external geometries. In addition, the material used in Concrete Printing is a high-performance fiber-reinforced fine aggregate concrete, resulting in superior material properties to those obtained in the CC technology.

Figure 17 – A full scale bench fabricated by the Concrete Printing with functional voids and posttensioned reinforcement [31]

The figure above shows a full-scale bench fabricated using Concrete Printing. The bench was 2 m long, 0.9 m maximum width and 0.8 m high and comprised of 128 layers of 6 mm thickness. The bench includes 12 voids that minimize weight, and could be utilized as acoustic structure, thermal insulation, and/or path for other building services. The bench also demonstrates a reinforcement strategy where carefully designed voids form conduits for post placement of reinforcement. Concrete Printing requires additional support to create overhangs and other freeform features. It uses a second material, in a similar manner to the FDM method. The disadvantage of this process is that an additional deposition device is needed for the second material resulting in more maintenance, cleaning and control instructions and the secondary structure must be cleaned away in a post processing operation. Exploiting the technologies explained above a Smart Slab [31], a fiber-reinforced concrete ceiling involving the technology of Digital Fabrication with Concrete (DFC) and the efficiency of robotics was constructed with 3D sand printing technique. The Smart Slab is part of the DFAB HOUSE, a collaborative demonstrator of the NCCR Digital Fabrication for the NEST building of Empa and Eawag. The Smart Slab is at the core of the demonstrator, resting on the double-curved mesh mould wall and supporting the two-story robotically-assembled timber units above. In addition, on the perimeter, it interfaces with the 15 Smart Dynamic Casting facade mullions. The Smart Slab is a 78-square-meter prestressed concrete slab discretized into eleven 7.4 metre long segments. Each segment is unique and prefabricated with special interface features which facilitate on-site connection through post-tensioning tendons. The geometry of the Smart Slab is structurally optimized for its challenging load-case, involving cantilevers of up to 4.5 meters. The material is distributed in a hierarchical grid of curved ribs, which vary between 30 and 60 cm in depth. In addition to this, the interstitial surfaces stabilize the grid and are only 1.5 cm thick. Consequently, the slab only weighs 15 tonnes, almost 70% less in comparison to a conventional solid concrete slab. The Smart Slab is a fully functional structural element which showcases an exquisite digitally designed geometry, with a deeply folded surface and millimeter-precise details. The computational design process uses the structural grid as a starting point to generate a basic mesh geometry with several dozen faces. After several iterations of selective subdivision sequences and parametric smoothing based on the relative position of the vertices within the slab, the articulated final surface is defined with around 13 million mesh faces. 3D printing is used for the most resource-intensive process in

concrete construction: fabricating the formwork. Beyond economic benefits, 3D printing enables several types of geometric features which are a significant challenge for other fabrication methods. Undercuts, sharp inner edges and micro-structures are difficult to achieve with CNC milling or hot-wire-cutting. Therefore, for the formwork of the Smart Slab, different 3D printing technologies were used to efficiently take advantage of their unique capabilities. Binder jetting was used for the most part, while fused filament deposition was used for locally integrating building services within the slab.

Figure 18 – Post-processing of the 3D printed formwork parts. Unconsolidated sand particles are being removed from the print bed

Figure 19 – complex shape of the ceiling obtained with 3D printing

Supplementary, laser-cut plywood formwork panels were integrated to define the geometry of the upstand ribs. This is because the upstand ribs only contain flat surfaces which do not require the high-resolution of 3D printing. This extensive and tolerance-free fabrication freedom for concrete has further applications, beyond the new and radically expressive aesthetic. It enables the perfect integration of the complete suite of building services and structural features necessary for a working building.

2.4 Fiber Reinforced Concrete (FRC)

2.4.1 Introduction

In recent years, several studies have been devoted to investigate the behavior of fiber-reinforced materials consisting of a continuous matrix and fibers that are appropriately dispersed inside it. A particular interest in the field of civil engineering was aimed to steel fiber reinforced concrete. The idea of reinforcing brittle materials using short fibers distributed randomly to improve their physical and chemical properties dates back to ancient times. The invention of composite materials with added fibers is to be attributed to the Egyptians (5000-3000 BC) who used crumbled straws drowned in bricks. Also, the Mayans (around 2,000 BC) put fibers in their ceramics to prevent cracking when the clay was quickly dried in the sun. Nevertheless, one has to go as far as the mid-1900s to talk about composites with the current meaning. Composites consisting of metallic or polymeric fiber-reinforced matrices were the ones that have been the most studied and applied in a wide field ranging from aerospace structures to sports equipment. From the ‘50s and ’60s to the present day, new composite materials have been studied, with greater interest, for applications in the civil engineering field: among these are cement-based composites. The research conducted by Romualdi, Batson and Mandel [31] in the late 1950s and early 1960s is fundamental and marked as the beginning of the studies related to the behavior of these composites. Fiber reinforced concrete is a composite material consisting of a cementitious matrix (hydraulic cement, aggregates, possibly with pozzolan and chemical additives commonly used in conventional concrete) and a dispersed fiber reinforcement. The application of fiber-reinforced concrete to primary structural elements subjected to bending, shear and torsion can be very useful. Indeed, cementitious materials such as concrete and

mortar are brittle and are characterized by an intrinsic weakness in tensile strength. The addition of steel fibers, then increases ductility and crack propagation resistance improving the fatigue behaviour and energy absorption capacity. The incorporation of fibers helps to improve the response of the concrete after cracking by bridging the cracks, reducing their width and resisting their opening. The behavior of fiber-reinforced concrete is governed by the following factors:

- fiber content;
- fiber geometry;
- bond between fibers and matrix.

2.4.2 Effect of dosage in Fiber Reinforced Concrete (FRC)

In fiber-reinforced concrete, the increases are not only of the maximum tension reached, but rather there are behaviours that result in a better fracture toughness, understood as deformation work to reach the breaking of matter, of ductility, of resistance to fatigue shock absorption, the ability to withstand loads after cracking, increased wear resistance and durability. The material behaves differently depending on the variation of the type of matrix, but also and above all based on the type of fibers used in the mixture and their dosage. Depending on the dosage, in fact, two kinds of behavior of the material can be obtained with the presence and formation of a single crack, Fig. 22 (a), or with high doses of fibers, it is possible to check for a hardening behavior with the formation of multiple cracks, Fig. 2.7 (b) [32]. Normally the behavior (a) occurs when there is a percentage of fibers that is less than 2% in volume, while exceeding this quota it is possible to establish multi-turbulent phenomena, with an increase in resistance.

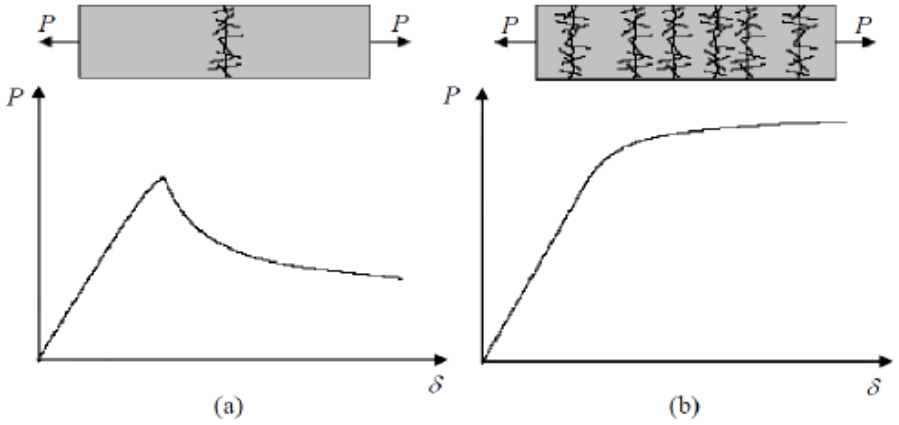

Figure 20 – Effect of dosage on the behavior of the FRC. Low fiber percentages (a), high percentages (b) [33])

The aggregates that are used in the construction of fiber-reinforced concrete must be studied carefully. Their size characterizes the dispersion of the fibers inside the matrix: a

larger size of the aggregates means less dispersion of the fibers in the mixture, as in Fig. 21. According to this phenomenon, an optimal behavior of the fibers in the mixture is achieved when the maximum size of the aggregates is a value between 1/5 and 1/3 of the length of the fibers employed [34].

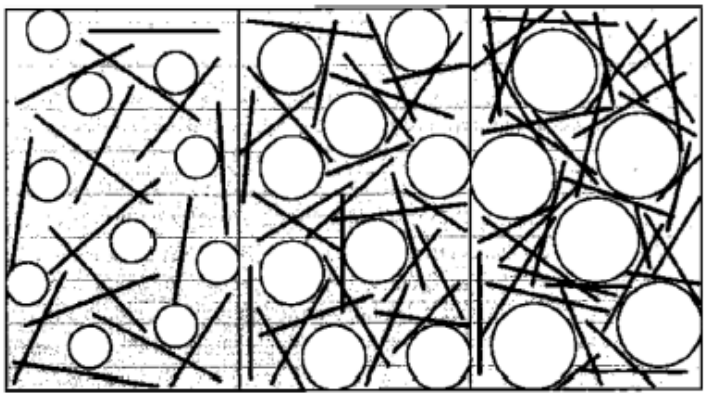

Figure 21 – Fiber dispersion in matrices with different aggregate sizes [34]

2.4.3 Fibers

The fibers inside the fiber-reinforced cementitious composites can be divided into two families based on the modulus of elasticity of the material they are made of:

- Rigid fibers: their Young modulus is greater than that of the cement matrix (Steel, Kevlar, Carbon, Asbestos, Glass, etc.).
- Flexible fibers: their elastic modulus is less than that of the matrix in which they are dispersed (Polyacrylonitrile, Cellulose, Nylon, Polypropylene, etc.)

The fibers with low modulus of elasticity, reducing the micro-cracks due to shrinkage, improve durability. The fibers with high modulus of elasticity improve the strength of the composite material and therefore the ability to withstand stress [34].

The main parameters that influence the technical characteristics of fiber-reinforced concrete are the type of fiber, the shape, the aspect ratio and the relative dosage.

The shape of the fibers is generally aimed at increasing the resistance to the extraction and can be of different types:

- smooth fibers;
- twisted fibers;
- hooked fibers;
- twisted-hooked fibers.

The absorbed energy increases as the aspect ratio increases, defined as the ratio of fiber length to its diameter, as shown in Fig, 22.

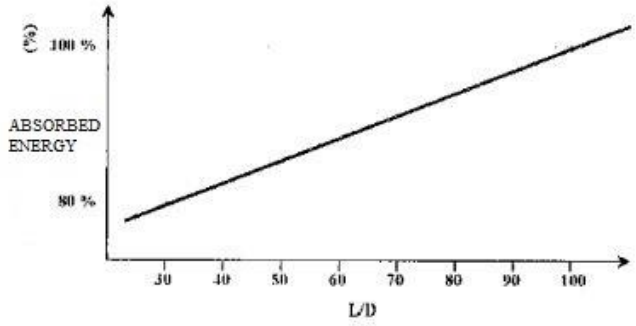

Figure 22 – Influence of the aspect ratio of a fiber with the energy absorbed [34]

The fiber dosage represents the predominant factor in the behavior of the element and directly affects the mechanical parameters and the technical performance of the fiber-reinforced compound. The dosage is both expressed in weight quantities (kg / cm^3 of fiber in the matrix) and in volumetric quantities depending on the overall volume of the concrete.

2.4.4 Orientation of steel fibers in magnetically driven concrete

A large number of experiments on steel fiber reinforced concrete (SFRC) have been carried out over the last four decades [35]. It was shown that fiber orientation has an effect on the tensile behavior of SFRC. The ultimate strength and post-peak stresses increase with a more favorable orientation of the steel fibers. An experience on the orientation of steel fibers in concrete was completed by Wen Xue, Ju Chen, Fang Xie and Bing Feng [37] using an experimental magnetic method to induce fiber orientation. Steel and iron sand slag were used in the concrete and in the magnetic drag concrete to replace the fine aggregate. In total, two series of concrete specimens were tested. One during the casting and one during the vibration of the concrete.

The purpose was to compare on the one hand, the magnetic induction on the fibers during the vibration of the compound compared to a reference sample carried out with the same mix design but without a magnetic device. On the other hand, the effect of the magnetic field on the fibers orientation during casting was compared to a specimen obtained without the magnetic device. Steel fibers having a nominal length of 31.0 mm and nominal diameter of 0.689 mm were used. The elastic modulus and tensile strength obtained from the manufacturer were 210 GPa and 810 MPa, respectively. In total, two layers of 16 steel fibers

each were placed in a 100 x 100 mm cubic concrete specimen. Concrete was cast with two different layers into the mold. The direction of the steel fibers was vertical to the direction of the magnetic force, as shown in Figure 23.

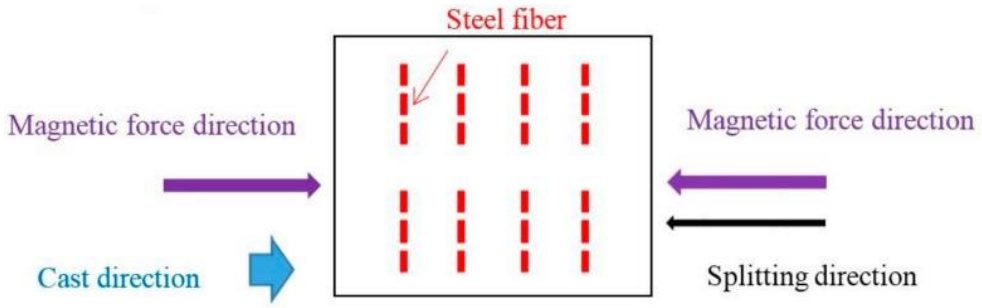

Figure 23 – Test setup of fiber orientation in magnetically driven concrete

The magnetic field was applied by a device developed by Chen [36] as shown in Figure 30. The direction of the magnetic force was changed by switching the direction of the current at a frequency of 5 s. Each test specimen was vibrated for about 3 min based on the test results from Chen [36]. All concrete cubic specimens were cured in the standard concrete curing room at a temperature of 20°C and humidity of 90% for 28 days, respectively. Afterwards, splitting tests were performed on cubic concrete specimens to obtain the tensile strengths.

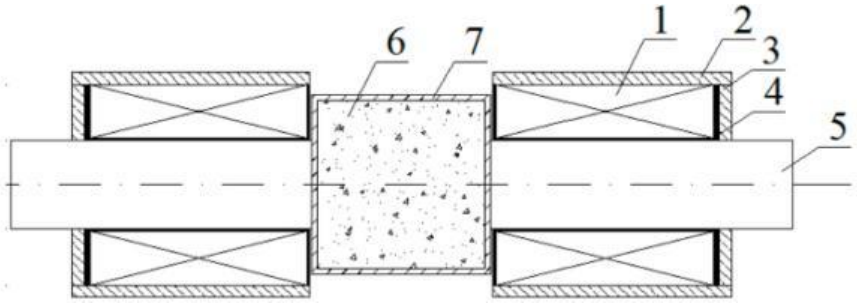

Figure 24 – Magnetic vibration device. 1- Electric Coil; 2- Shell; 3- Steel plate; 4-Coil frame; 5-Iron core; 6-Concrete; 7-Mold

The direction of the steel fibers of specimen submitted to the shaking table remained vertical to the splitting direction, which means that had almost no effect on the orientation of the steel fibers. While, in the samples in which the magnetic force was applied during vibration

the angles between the steel fibers and the concrete cast direction ranged from 35° to 75° with average value of 45°. For the specimen submitted to magnetic field during casting, the steel fibers changed almost 90° of orientation. A comparison of the four test specimens indicates that the orientation on the steel fibers was most effective in the last specimen. It may be explained that the movement of the coarse aggregate under the magnetic force was helpful for the steel fiber's orientation. It is shown that the tensile strengths at 28 days of the specimen series magnetically inducted were higher by 3.5% and 4.4%, than those of the specimen series not subject to the magnetic field. The enhancement in tensile strength may have been caused by the favorable directions of the steel fibers. Fibers are the best aligned with the direction of tensile load having the maximum contribution in tensile resistance.

2.4.5 High-Performance Fiber Reinforced Cementitious Composite (HPFRCC)

The birth of High-Performance Fiber Reinforced Cementitious Composite (HPFRCC) originates from the limit encountered in the development of fiber-reinforced concrete elements (FRC) due to their composition. The reduced workability in compounds with increasing volumes of fibers prevented it from entering the High-Performance category, while the development of HPC materials was limited due to their poor tensile strength and their high compression fragility. To mitigate these two characteristics, tailored solutions have been studied that see both the use of fibers and high performance. Studies and developments have given birth to different materials, such as SIFON (Slurry Infiltrated Fiber Concrete) able to reach a quantity of fibers equal to 12-13% of the total volume, ten times higher than the quantity contained in normal FRCs, reaching very high compression resistances of 120-140 MPa.

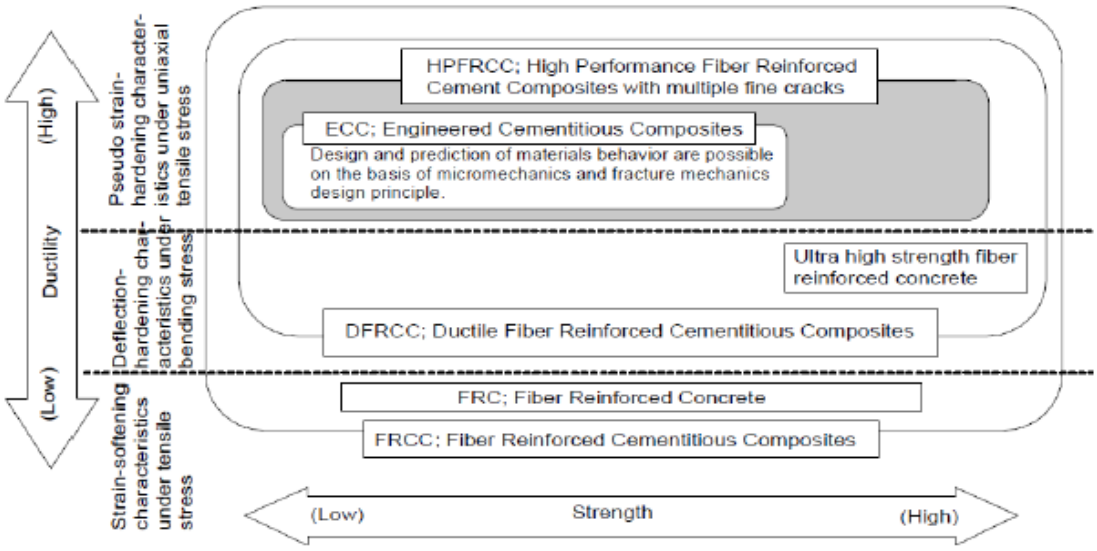

Figure 25 – Classification of fiber-reinforced compounds [38]

The application of fine elements in the cement mixture, the addition of superplasticizer, the possibility of reducing the water / cement ratios to very low values, the use of thin steel fibers allowed to develop those that are called HPFRCC. These materials are characterized by an excellent tensile deformation capacity and develop a multiple cracking that provides the compound with a hardening behavior under tensile stress.

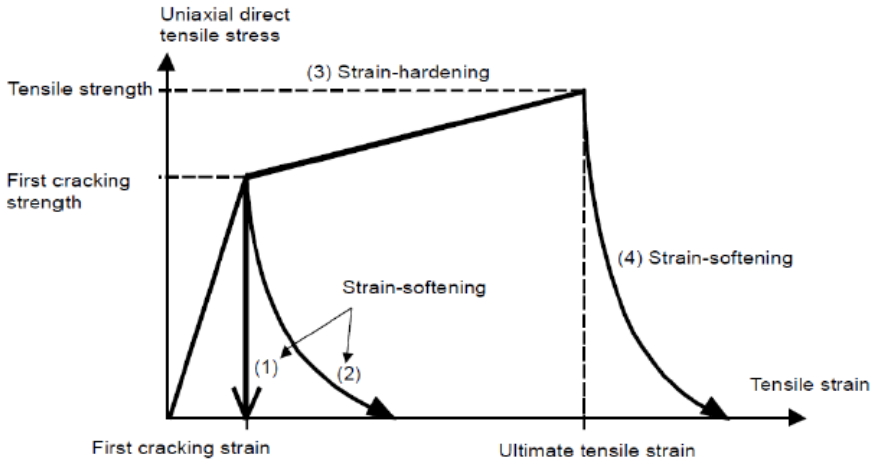

Figure 26 – 'strain-hardening' and 'strain-softening' concepts, under axial tensile stresses

As seen, the FRC compounds follow the two typical trends (1) and (2) after the formation of the first crack, without obtaining higher tensile values in the post-crack branch, as assessed for cement elements. The HPFRCC material, on the other hand, increases its maximum tension due to the formation of the first crack, following the behavior described by the curve (3) in Fig. 26.

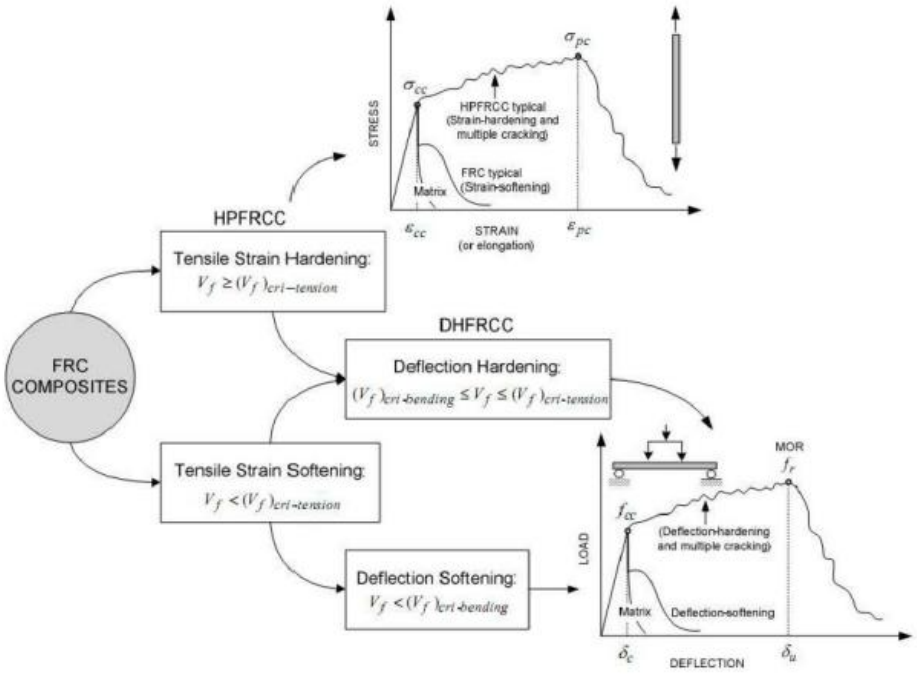

Figure 27 – Classification of FRC based on the stress-strain response before tensile and flexural tests [39]

The High-Performance category is used to distinguish materials with particular performances from conventional ones. What gives attention are, for example, the gains in terms of strength, ductility, toughness, durability, stiffness, thermal resistance, but also the final cost of the material and of the structural element produced, depending above all on the expected useful life. The "high performance" assessment for some of the aforementioned qualities must be made according to the behavior as identified in Fig. 2.14. The direct tensile behavior of the material can be strain-hardening or strain-softening (degrading). According to Naaman and Rehindart [39], those that have a strain-hardening behavior are deficient in HPFRCC materials. On the basis of the flexural behavior, instead, the same distinctions are made, going to evaluate the trend of the load-displacement diagram determined in a bending test. There are therefore two typical behaviours: deflection hardening and also deflection softening. “High performance fiber reinforced cement composites (HPFRCC) form a class of cement composites characterized by a tensile stress-strain response that exhibits strain hardening accompanied by multiple cracking”. [40]. It is now widely recognized that the use of these materials can significantly improve for example the behavior of the structure under seismic actions, as well as the resistance to impacts and explosions. Their particular characteristic is that of being able to develop a hardening behavior. The practical significance of this peculiarity is in the formation of a multi-layer extending along the entire length of the element stressed to traction or in the intrados part when inflected. Resistance to withstand stress increases, as does the ultimate deformation. The next step was to be able to check the crack width. A new type of cement material has therefore been developed. The Engineered Cementitious Composites (ECCs), a type of material that is part of the caterogy of HPFRCCs, as shown in Fig. 2.12, represent a new element that can offer a solution to the problem of the durability of structures. This type of compound can obtain a final deformation of about 300 ÷ 500 times higher in reference to traditional concretes (3 ÷ 7% of deformation against 0.1% of traditional concrete), maintaining the crack opening to very low values, on the order of 80 μm. For these characteristics, Mustafa Sahmaran and Victor C. Li [41], are wondering if this particular type of material can be accepted as crack-free concrete. The HPFRCCs have a strain-hardening behavior with the formation of small multi-crack opening that can carry a greater value of load after their formation, allowing the cementitious material to behave as a ductile metal.

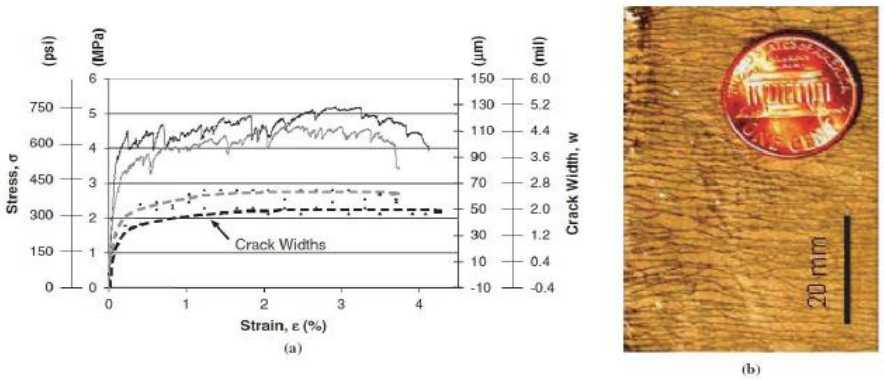

Figure 28 – ECC: (a) strain-stress curves and (b) development of micro-cracks [41]

There is no particular mix design for this type of material, but every "ingredient" that makes it up is carefully chosen to be used to the best of its characteristics. In fact, the realization is "tailored", as are the fibers employed. Their volume V_f is usually at least 2%. ECCs therefore do not have a particularly high fiber content inside them, but their composition, carefully designed on micromechanical basis, allows to improve the cohesion between matrix and fibers that allows to effectively govern the redistribution of efforts following the formation of the first slot. The advantages obtained from these characteristics are innumerable: a reduction of the crack opening, or better still, the formation of multiple cracks instead of the propagation and spread of a single crack makes the material much less permeable to the aggressive substances, as can be seen in Fig. 29.

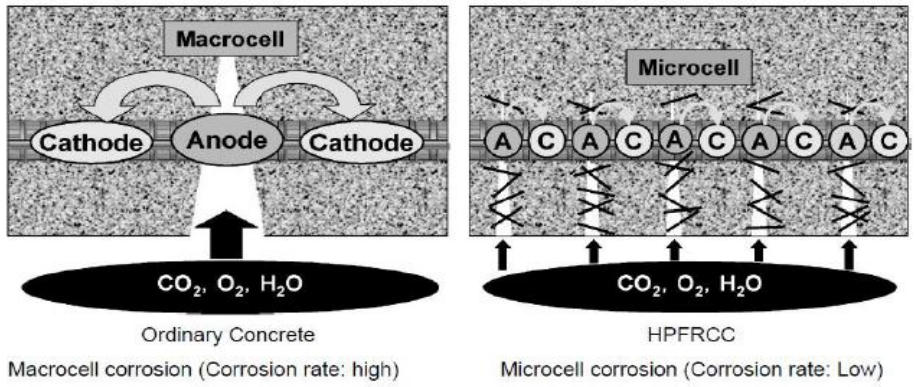

Figure 29 – Corrosion trend according to the type of crack [34]

This particular material can find particular applications in fields where explicit demands for ductility are made. Fukuyama et al. [35] have experimented the use of ECCs as seismic-resistant apparatuses, where, the image Fig. 30, shows a clear difference between the shear behavior of a reinforced beam and the employment of high ductile material. Another important factor is the ability to exploit the potential of autogenous self-healing: the particular chemical composition of the compound and its physical properties can favourably influence the development of typical products of autogenous self-healing in different types of environments, as seen in Fig. 31.

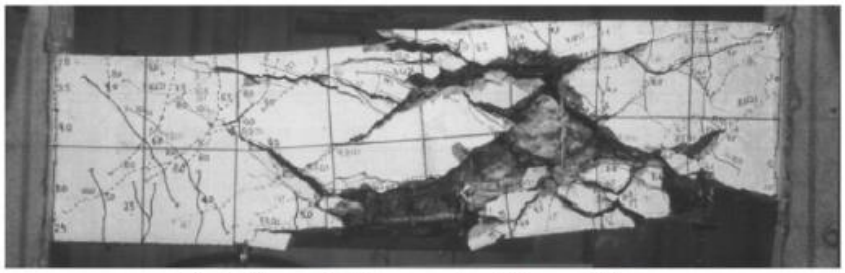

Reinforced Concrete Shear Beam

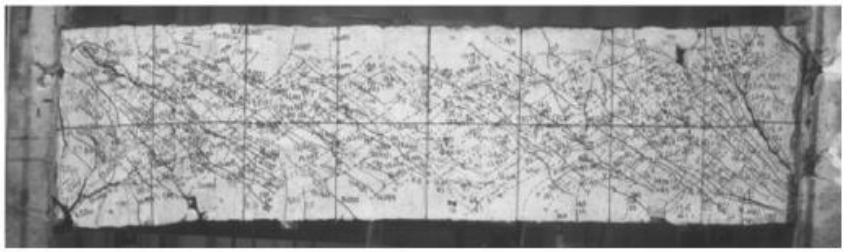

ECC Shear Beam

Figure 30 – Application of ECCs as shear beam [42]

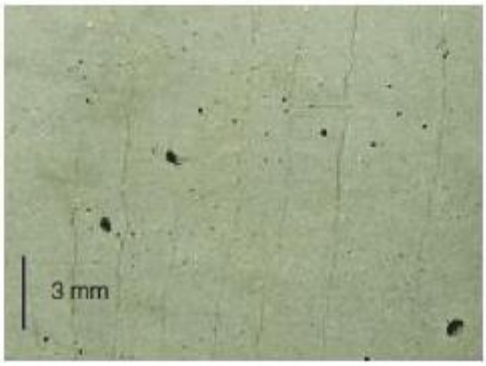

(a)

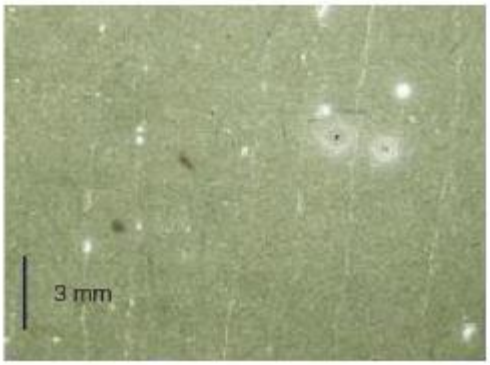

(b)

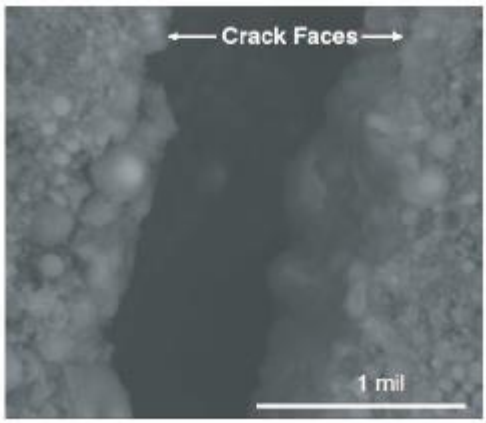

(c)

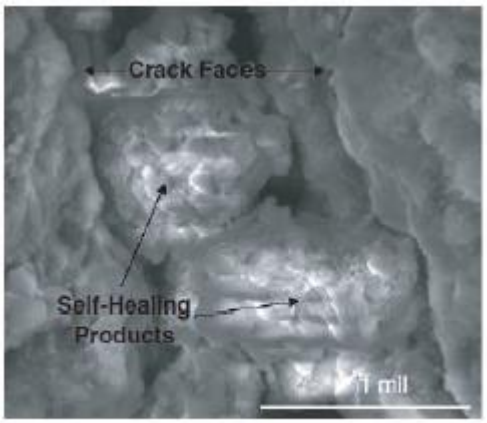

(d)

Figure 31 – Effect of self-healing on the ECC before (a, c) and after (b, d) [41]

2.5 Implementation of 3D printing and fiber orientation in the master's experience

The 3D printing technique was used to generate the molds using a Fused Filament Fabrication (FFF) machine. Thanks to technology and the 3D printing technique the limits of time and material imposed by the traditional technique of wooden formwork are exceeded. In this way complex and toothed shapes of formwork are generated, but at a reasonable price. The size of the formwork teeth was dictated by the length of the fibers used. This allowed during the casting to accentuate the "Wall Effect" on the fiber orientation. As discovered by Roussel and Martinie [55] quantitatively, the average orientation factor in a zone of thickness equal to the half-length of the fiber turns from $\alpha = 0.5$ for the isotropic bulk material to $\alpha = 0.6$ for sections perpendicular to the wall, moreover this preferred orientation is induced as soon as the material is poured into the formwork and only depends on fiber length and geometry of the element to be cast. In addition, the fibers orientation as previously seen can be induced through a magnetic field or through the size of the aggregates. Indeed, it has been demonstrated that fibers strongly affect the packing density of aggregates and vice versa. Barthos and Hoy [43] noted that packing density is reduced with fiber addition in a slightly larger way with coarse aggregate than with sand, because "the sand is able to pack tightly around the fiber, whereas coarse aggregates are pushed apart by the fiber's presence".

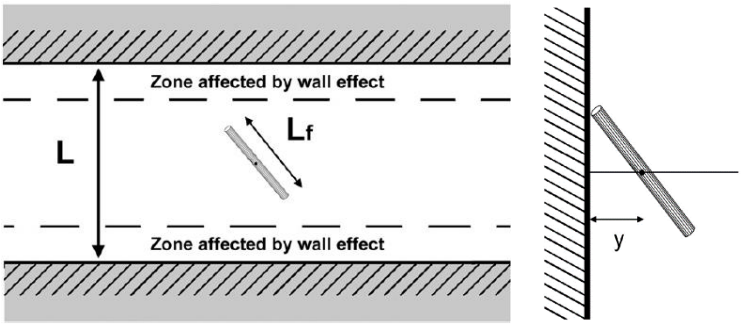

Figure 32 – On the left, wall effect for a fiber of length L_f in a structural element of thickness L. The thickness of the zone affected by wall effect is $L_f/2$. On the right, wall effect for a fiber of length Lf at a distance of a wall $y < L_f / 2$ [33]

This complex specific phenomenon illustrated in Fig. 33 cannot be quantitatively predicted without numerous experimental measurements allowing for the fitting of empirical coefficients. Therefore, by using a mix design with coarse aggregates, while maintaining the required self-compacting and workability characteristics, it is possible to induce the orientation of the fibers.

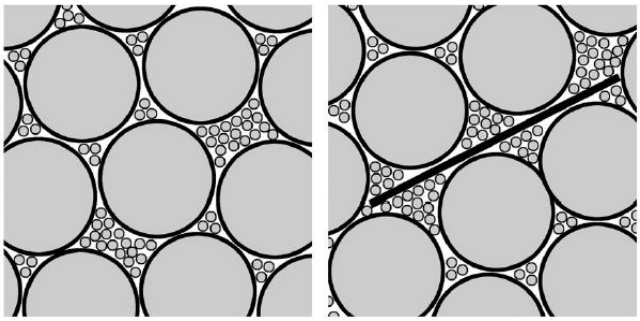

Figure 33 – Effect of a fiber on the packing of gravel and sand mixtures.

Regarding the considerations previously discussed on the fresh state of the concrete and its components, the purpose of this work is to investigate how the fibers orientation induced through the 3D modeling of the formwork allows an increase in flexural strength in high-performance fiber-reinforced concretes, as well as verify the casting methods and the geometry (which was designed to "reproduce" the peculiarities of 3D printed elements).

CHAPTER 3 – MATERIALS AND METHOD

An analysis concerning the State of the Art of 3D printing methods and in particular Digital Fabrication with Concrete (DFC), passing from the properties of Fiber Reinforced Concrete (FRC) and ongoing research activities up to the expectations of the master thesis experience was carried out. In this section the materials and methods used to perform the experimental work will be discussed. First, the materials will be listed one by one accompanied by a brief theoretical description, subsequently a mix design will be realized that satisfies the workability and homogeneity performance of the fiber reinforced concrete with fibers dispersed inside. Secondly, the formwork formation process using 3D printing method and the casting methods. Finally, x-ray computed tomography and fiber orientation analysis will be discussed, highlighting the peculiarities of Avizo software, ImageJ, Java class and Paraview. The fiber orientation analysis will also involve an additional experience concerning a casting in which two flows come into contact with each other. The second purpose of the master's thesis is to describe only the behaviour during the meeting of the fibers inside the two different casting.

3.1 Materials

The materials used for all concrete mixes and samples can be seen in Table 1.

Material	Name	Producer	Pic
Cement	Durabat X-trem - CEM I 52.5 N SR 5 PM-CP2	Lafarge	
Sand	0,1-0,45 mm	Baubedarf	
Silica Flour	K6	Carlo Bernasconi AG	
Silica Fume	Elkem Grade 971-U	Elkem	
Superplasticiser	MasterGlenium ACE 30	BASF	

Table 2 - Materials used for the concrete matrix

3.1.1 Cement

The cement used in the mix design is type I of class 52.5 R with rapid hardening, which from the technical data sheet is composed of 95-100% clinker according to UNI EN 197-1, while the remaining part consists of any secondary constituents. Follows chemical composition of the cement.

Costituent	[%]
C_3S	65 %
C_2S	11 %
C_3A	9 %
C_4AF	6 %

Table 2 – Chemical composition of CEM I 52.5 R

3.1.2 Aggregate

The aggregate that was used in the castings is a sand with a maximum diameter of 4 mm. The granulometric curve of the material is shown in the following figure.

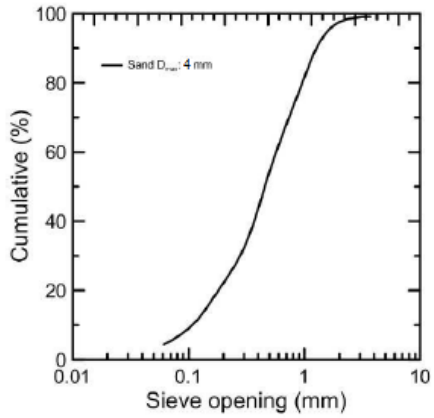

Figure 34 - Granulometric curve of the sand used for packing the mortar

3.1.3 Silica fume

Silica fume, also known as microsilica, (CAS number 69012-64-2, EINECS number 273-761-1) is an amorphous (non-crystalline) polymorph of silicon dioxide, silica. It is an ultrafine powder collected as a by-product of the silicon and ferrosilicon alloy production and consists of spherical particles with an average particle diameter of 150 nm. In the mix design, silica fume has been added to cement concrete to improve its properties, in particular its compressive strength, bond strength, and abrasion resistance. Addition of silica fume also reduces the permeability of concrete to chloride ions, which protects the reinforcing steel of concrete from corrosion, especially in chloride-rich environments such as coastal regions and those of humid continental roadways and runways (because of the use of deicing

salts) and saltwater bridges. Effects of silica fume on different properties of fresh and hardened concrete include:

- Workability: with the addition of silica fume, the slump loss with time is directly proportional to increase in the silica fume content due to the introduction of large surface area in the concrete mix by its addition. Although the slump decreases, the mix remains highly cohesive.
- Segregation and bleeding: silica fume reduces bleeding significantly because the free water is consumed in wetting of the large surface area of the silica fume and hence the free water left in the mix for bleeding also decreases. Silica fume also blocks the pores in the fresh concrete so water within the concrete is not allowed to come to the surface.

Standard specifications for silica fume used in cementitious mixtures are ASTM C1240 and EN 13263.

Element			*Spec**	*Typical***
SiO_2	%	min.	98	98.4
C_{free} ***	%	max.	0.7	0.50
Fe_2O_3	%	max.	0.1	0.01
Al_2O_3	%	max.	0.3	0.20
CaO	%	max.	0.3	0.20
MgO	%	max.	0.2	0.10
K_2O	%	max.	0.3	0.20
Na_2O	%	max.	0.2	0.15
P_2O_5	%	max.	0.10	0.03
SO_3	%	max.	0.3	0.10
Cl	%	max.	0.10	0.01
H_2O ****	%	max.	0.5	0.20

Properties		*Spec**	*Typical***
Loss on Ignition	% max.	0.8	0.50
Coarse Particles >45µm	% max.	0.5	0.20
pH-value		5.5 - 7.5	6.8
Undensified 971-U			
Bulk density ****	kg/m³	250 - 350	300

Figure 35 – Characteristics of the specific silica fume

3.1.4 Fibers

The used steel fibers are fully straight without hooked-ends. The geometric properties of the steel fibers can be seen in Table 2. The mechanical properties as well as the rheology of HPFRC are linked not only to the fiber content but also to the geometric properties of the fibers. In order to be able to compare the rheology and mechanical properties of different concrete mixes, the geometry of the fibers and the fiber content of the mix are considered using the fiber aspect ratio f_{ar} (Equation 1) and fiber factor f_f (Equation 2). The fiber aspect

ratio f_{ar} is a simple geometric parameter and useful to compare the properties of different individual fibers. The fiber factor f takes the geometry and amount of fibers into account.

$$f_{ar} = \frac{l}{d}$$

Equation 6 - Fiber aspect ratio

l = fiber length

d = fiber diameter

$$f_f = f_{ar} * V_f$$

Equation 7 - Fiber factor

f_{ar} = fiber aspect ratio

V_f = fiber volume fraction (V_{fib} / V_{tot})

Steel Fibers	Lenght (mm)	Diameter (mm)	Aspect Ratio	Producer
Type 1	10	0,20	50	Bekaert
Type 2	9	0,15	60	Bekaert

Table 3 - Steel fibers used as a fiber reinforcement for the investigated HPFRCCs

Figure 36 - Steel fibers

High Performance Fiber Reinforced Concretes typically have a dense and fine granular matrix containing small and especially hard aggregates, low water/binder ratios and high amounts of silica fume and superplasticizer, leading to an extremely compact matrix. The strength of the mixes used in this thesis did not exceed 100 MPa and therefore the composite was classified as high-performance fiber reinforced concrete (HPFRC) [45].

The volume fraction of the fibers was calculated as the volume of the fibers divided by the total volume (Equation 3). The total volume is equal to the volume of the fibers plus the volume of the concrete matrix. V_{fib} was calculated as the mass of the fibers divided by the

density of the fibers (ρ_{fib} = 7850 kg/m^3) as shown in Equation 4. The volume of the matrix V_m was calculated with Equation 5.

$$V_f = \frac{V\ fib}{V\ tot}$$

Equation 8 - Fiber volume fraction

V fib = fiber volume

V tot = total volume (matrix + fibers)

$$V_{fib} = \frac{m\ fib}{\rho\ fib}$$

Equation 9 - Fiber volume

m fib = fiber mass

ρ fib = fiber density

$$V_m = \frac{m\ tot}{\rho\ tot} - V_{fib}$$

Equation 10 - Matrix volume

m tot = total mass (m fib + m matrix)

ρ tot = total density (ρ fib + ρ matrix)

V fib = fiber volume

3.1.5 Superplasticizer

The superplasticizer used is MasterGlenium ACE 30, a polycarboxylate ether-based (PCE). This polymer is characterised through an anionic backbone and positively charged side chains (Figure 37). The negatively charged backbone sticks to the positively charged cement particles while the side chains reach into the solution. The positively charged side chains lead to a repulsion of the cement particles and an increased distance between them (Figure 38). The latter strongly reduces the van der Waals forces and therefore increases the flowability of the concrete [46].

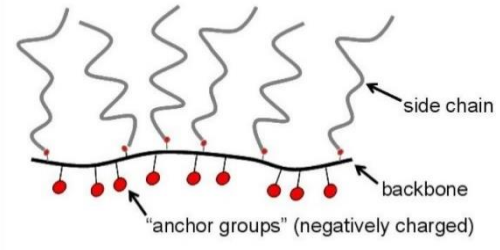

Figure 37 - PCE-based polymer

Even though the general mechanisms of action are the same for PCE based superplasticizers, the characteristics of the products still can vary strongly as there are several parameters,

which can be varied during manufacturing. This also brings the opportunity of finding well-adapted superplasticizers for concrete with specific requirements. The most important parameters are:

- The type of monomers used for the backbone and the amount of negative charges;
- The length of the backbones;
- The composition of the side chains;
- The length of the side chains in respect to the backbones.

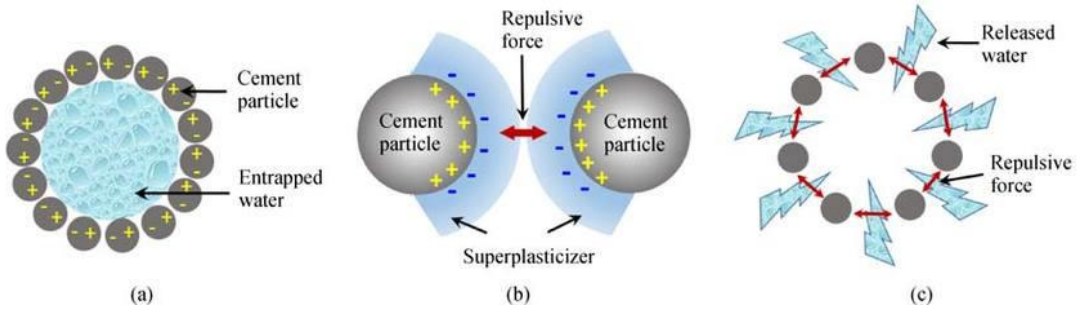

Figure 68 - Adsorption of the polymers to cement particles

3.1.6 3D printed formworks

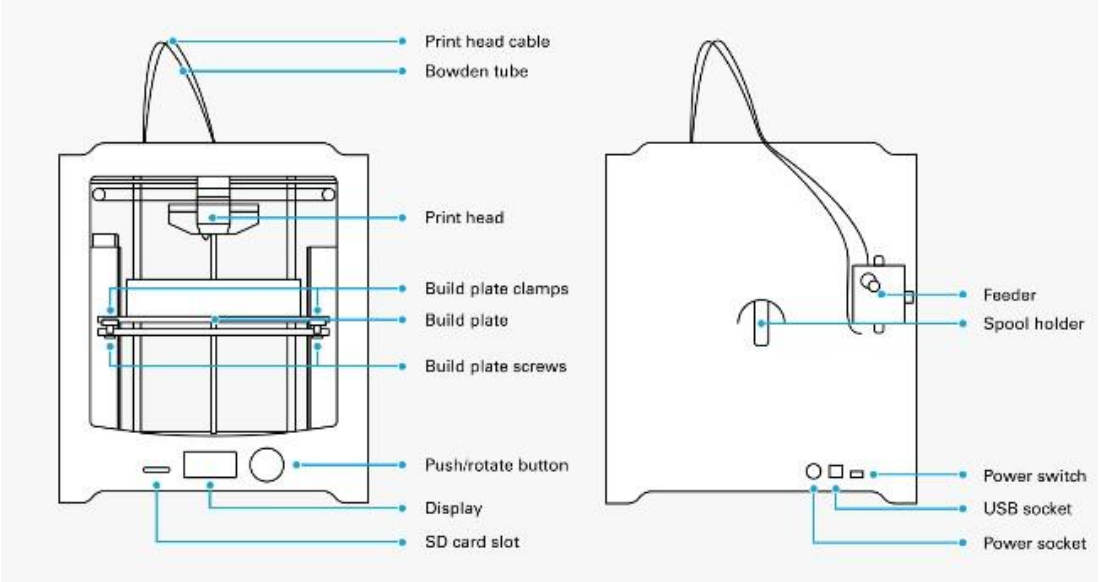

Figure 39 - FFF or FDM 3D printer

FFF (Fused Filament Fabrication) or FDM (Fused Deposition Modeling) 3D printing is a technology developed by S. Scott Crump in 1988 that uses a continuous filament of a thermoplastic material. Filament is fed from a large coil through a moving of a heated head printer extruder and is deposited on the growing work. The print head is moved under computer control to define the printed shape.

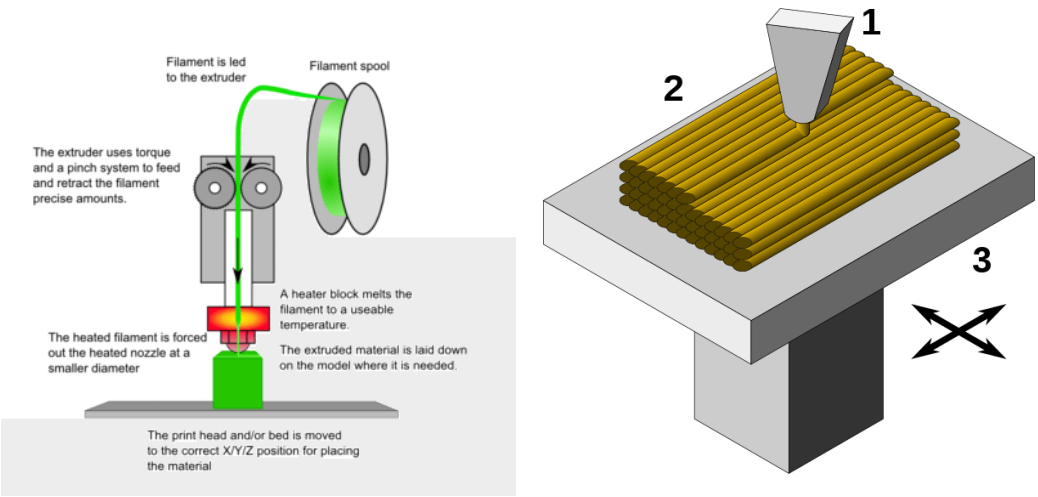

Figure 40 - Illustration of an extruder with the name of involved parts

The 3D printed frameworks used for this master thesis were designed by the Chair for Digital Building Technology (DBT) at the Department of Architecture (D-ARCH) at ETH Zurich. The formworks were made with 0.4 mm thick layers of PLA bonded together through a calcium phosphate solution. The fused filament fabrication (FFF) printer works in the following way:

A heated nozzle (1) ejects molten plastic, depositing it in thin layers (2), onto a print bed (3), forming the 3D printed part [47].

3.2 Methods

3.2.1 Mixing procedure

The mixtures were produced using a Hobart A200N 20 QT mixer. The formulation of the produced concrete mixes and the description of the mixing process can be found in Table 4.

Step	Procedure	Remarks	Time at end of the step
1	Mix the dry components on speed 1 for 5 min	Dry components = cement, silica flour, silica fume, sand	5 min
2	Add the water	Let the mixer run during this procedure	5.5 min
3	Mix on speed 1 for 1 min		6.5 min
4	Add superplasticizer	Let the mixer run during this procedure	7 min
5	Mix on speed 1 for 6 min, or until change or rheology if it hasn't occured yet at that time		13 min (+ t min)
6	Mix on speed 2 for 5 min		18 min (+ t min)
7	Stop the mixer and add half of the fibers (1 min)	Restart the mixer after the minute	19 min (+ t min)
8	Mix on speed 1 for 30s		19.5 min (+ t min)
9	Stop the mixer and add half of the fibers (1 min)	Restart the mixer after the minute	20.5 min (+ t min)
10	Mix on speed 1 for 3 min	**Total time**	**23.5 min (+ t min)**

Table 4 - Mixing procedure for the HPFRC

3.2.2 Measurement methods and mix optimization

Dry extract content of the superplasticizer

An accurate description of the flow behaviour of the concrete as a function of the amount of used superplasticizer was desired. It is important for that point to consider the fact that the superplasticizer contain a part of water and a part of dry extract, which contains the active ingredient. Additionally, this dry extract fraction can vary from canister to canister. The dry extract is the driving force for increasing the workability, while the water content affects the W/C and W/B ratio. It had thus been decided that the amount of dry extract would be used as a parameter, and the added water content in the mix would be adapted as to have a fixed water-to-binder ratio.

The superplasticizer content has been measured as follows using a KEN MRS 120-3 device:

- Put quarz sand on a small plate;
- Tar the plate in the machine;
- Put a couple of grams of liquid on the sand;
- Close the machine, run it at 105° until weight stabilizes (= no more water);
- The dry extract content is then the ratio of the remaining mass to the original mass.

MG Ace 30 Drum	A (29.10.2018)
Solid Cont. [%]	29,06%

Table 5 - Percentage of solid content in superplasticizer

Preliminary mix design selection

The choice of the optimal mix design was made on the basis of workability (measured by mini-slump flow diameter) and resistance to fiber segregation (evaluated as described below). The process of obtaining the slump flow diameter is as follows:

- user the conical trunk on a glass plate;
- fill the conical trunk right after the mixing, make sure that the surface of the concrete is at the same height as the upper limit of the mold;
- lift the mold slowly, keep it approximately 1 cm above the concrete surface for 10s to let most of the concrete contained in the mold leave it;
- measure the circle diameter after 3 min unless the mix has stopped flowing (average of the diameter of two orthogonal directions). A target value of 260-262.5 mm was assumed as satisfactory.

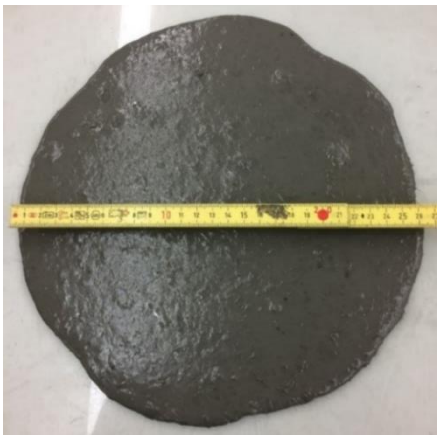

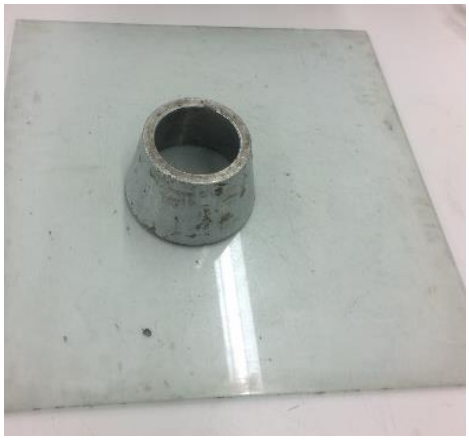

Figure 417 and 42 – On the left, slump flow test, 26.25 cm of diameter; on the right, Truncated cone for mini slum flow test

The dimensions of the used test equipment can be found in the following table [48].

Height	6,0	cm
Radius of bottom section	3,5	cm
Radius of top section	5,0	cm
Volume	344	cm^3

Table 6 - Dimensions of the mini slum flow mould [46]

Afterwards with the mixes prepared, cylinders of 100 mm diameter and a height of 200 mm were obtained and were stored for a day in a climatic chamber at humidity of 90% and temperature of 20 °C. The following day they were submitted to the cut in order to evaluate the segregation of the fibers.

Figure 43 - Segregation of half cylinder samples

DATE			29.10.2018	29.10.2018	31.10.2018	06.11.2018	06.11.2018	06.11.2018
NAME			F.10-03-22	F.10-03-21	F.10-0295-10	F.10-0295-095	F.10-0295-085	F.10-0290-10
W/B	[-]		0,300	0,300	0,295	0,295	0,295	0,290
SPDE	[%B]		2,20%	2,10%	1,00%	0,95%	0,85%	1,00%
Desired Vol.	[l]		4,0	4,0	4,0	4,0	4,0	4,0
FORMULA								
Cement	[kg]		2,677	2,677	2,677	2,677	2,677	2,677
Silica fume	[kg]		0,334	0,334	0,334	0,334	0,334	0,334
Silica flour K6	[kg]		2,677	2,677	2,677	2,677	2,677	2,677
Sand 0.1-0.45	[kg]		2,021	2,021	2,021	2,021	2,021	2,021
Added Water	[kg]		0,742	0,749	0,815	0,818	0,826	0,800
Superplasticizer	[kg]		0,228	0,218	0,1036	0,0984	0,0881	0,1036
Fibres	[kg]		1,000	1,000	1,000	1,000	1,000	1,000
Total mass	[kg]		9,678	9,675	9,627	9,625	9,622	9,612
FRESH STATE PERFORM								
Slump	[cm]	Min	27,5	27,0	20,0	25,5	24,0	26,5
		Max	28,0	28,5	22,0	27,0	24,5	27,0
		avg	27,75	27,75	21,00	26,25	24,25	26,75
DENSITY								
ρ	[-]		2,428	2,428	2,428	2,428	2,428	2,428
Mix Volume	[l]		4,0	4,0	4,0	4,0	4,0	4,0
REAL WATER								
Real Water	[kg]		0,903	0,903	0,888	0,888	0,888	0,873
Real W/B	[-]		0,300	0,300	0,295	0,295	0,295	0,290
Real W/C	[-]		0,337	0,337	0,332	0,332	0,332	0,326
FIBRES								
Length	[mm]		10	10	10	10	10	10
Dia.	[mm]		0,20	0,20	0,20	0,20	0,20	0,20
Aspect Ratio	[-]		50	50	50	50	50	50
Steel dens.	[-]		7,885	7,885	7,885	7,885	7,885	7,885
Mass Frac.	[%]		10,3%	10,3%	10,4%	10,4%	10,4%	10,4%
Vol. Fibers	[l]		0,127	0,127	0,127	0,127	0,127	0,127
Vol. Frac.	[%]		3,18%	3,18%	3,20%	3,20%	3,20%	3,20%
Fibre Fact.	[-]		1,59	1,59	1,60	1,60	1,60	1,60

Table 7 - Mix design selected for workability and homogeneous concrete paste

Because problems were encountered, to make more homogeneous the concrete and to accentuate the "wall effect" phenomenon it was decided to introduce a fibers length of 9 mm. To obtain an acceptable value of 26.25 cm of the diameter, it was decided to increase the content of 9 mm fibers in fiber-reinforced concrete by 20% .

DATE			29.10.2018	29.10.2018	06.11.2018	06.11.2018	06.11.2018	13.11.2018
NAME			F.10-03-22	F.10-03-21	F.10-0295-095	F.10-0290-10	F.09-0295-10	F.09-0295-095
W/B		[-]	0,300	0,300	0,295	0,290	0,295	0,295
SP_{DE}		[%B]	2,20%	2,10%	0,95%	1,00%	1,00%	0,95%
Desired Vol.		[l]	4,0	4,0	4,0	4,0	4,0	4,0
FORMULA								
Cement		[kg]	2,677	2,677	2,677	2,677	2,677	2,677
Silica fume		[kg]	0,334	0,334	0,334	0,334	0,334	0,334
Silica flour K6		[kg]	2,677	2,677	2,677	2,677	2,677	2,677
Sand 0.1-0.45		[kg]	2,021	2,021	2,021	2,021	2,021	2,021
Added Water		[kg]	0,742	0,749	0,818	0,800	0,815	0,818
Superplasticizer		[kg]	0,228	0,218	0,0984	0,1036	0,1036	0,0984
Fibres		[kg]	1,000	1,000	1,000	1,000	1,000	1,200
Total mass		[kg]	9,678	9,675	9,625	9,612	9,627	9,826
FRESH STATE PERFORM								
Slump	Min	[cm]	27,5	27,0	25,5	26,5	26,0	25,5
	Max		28,0	28,5	27,0	27,0	27,0	27,0
	avg		27,75	27,75	26,25	26,75	26,50	26,25
DENSITY								
ρ		[-]	2,428	2,428	2,428	2,428	2,457	2,457
Mix Volume		[l]	4,0	4,0	4,0	4,0	3,9	4,0
REAL WATER								
Real Water		[kg]	0,903	0,903	0,888	0,873	0,888	0,888
Real W/B		[-]	0,300	0,300	0,295	0,290	0,295	0,295
Real W/C		[-]	0,337	0,337	0,332	0,326	0,332	0,332
FIBRES								
Length		[mm]	10	10	10	10	9	9
Dia.		[mm]	0,20	0,20	0,20	0,20	0,15	0,15
Aspect Ratio		[-]	50	50	50	50	60	60
Steel dens.		[-]	7,885	7,885	7,885	7,885	7,885	7,885
Mass Frac.		[%]	10,3%	10,3%	10,4%	10,4%	10,4%	12,2%
Vol. Fibers		[l]	0,127	0,127	0,127	0,127	0,127	0,152
Vol. Frac.		[%]	3,18%	3,18%	3,20%	3,20%	3,24%	3,80%
Fibre Fact.		[-]	1,59	1,59	1,60	1,60	1,94	2,28

Table 8 - Change of length fibers from 10 to 9mm and increase of the fibers content in the final mix design

Finally, the workability trend expressed by the mini slump flow test in diameter of 26.25 mm is visible from the graphic below, as a function of water/binder ratio and percentage of superplasticizer

SP_{DE} \ W/B	0,309	0,300	0,295	0,290	0,285	0,280
2,39%	26,25	29,50				
2,30%		27,00				
2,20%		27,75				
2,10%		27,75				
2,00%		27,00				
1,90%		26,75				
1,80%		28,75				
1,50%		28,75				
1,25%		28,50				
1,15%		28,75				22,25
1,10%		29,25			23,75	23,75
1,05%		29,50		27,25	25,75	23,00
1,00%		29,50	27,25	26,75	23,50	21,75
0,95%		28,25	26,25	25,50	21,25	13,50
0,90%		26,50	25,50	23,25	15,00	
0,85%		24,50	24,25	18,25		
0,80%		24,25	19,25			
0,70%		20,50				
0,60%		15,25				
0,50%		9,5				

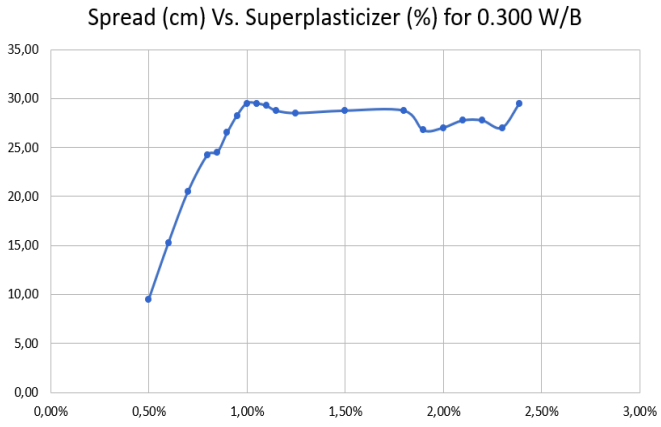

Table 9 - Relationship between spread and percentage of superplasticizer with 0.300 W/B

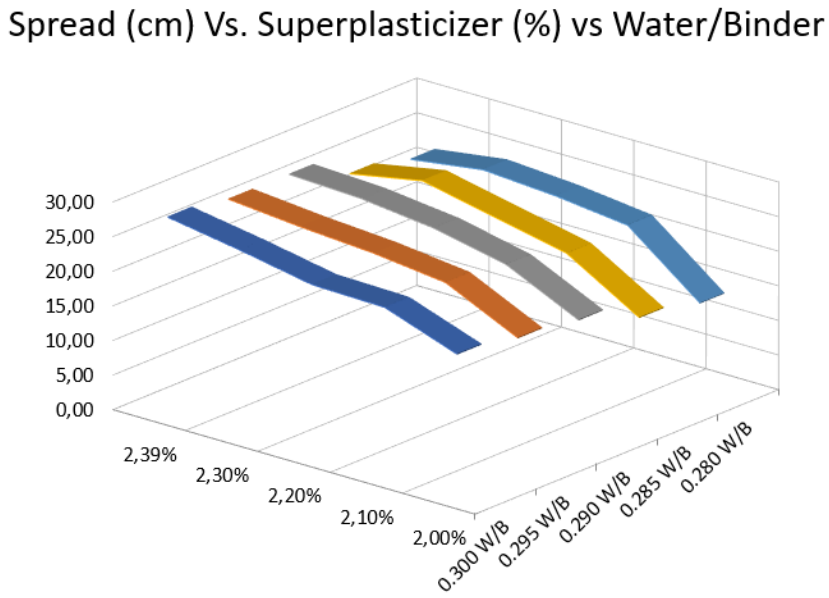

Table 10 - Relationship between spread, percentage of superplasticizer and Water/Binder

It is clearly visible that beyond 1% of superplasticizer content the spread in term of workability is acceptable because a plateau is reached, and it is also useless to put more of it because it reaches a saturation effect. In the initial part of the graph a linear behaviour occurs between spread and superplasticizer. Until 1%, the circle diameter measured by the mini-slump flow test increases as the amount of superplasticizer in the mixture increases. Finally, it is interesting to assert that an acceptable workability is reached with the values of 0.295 W/B and 0.95% of superplasticizer.

Figure 44 - Best results of High-Performance Fiber Reinforced Concrete cylinder samples

Shuttering

The molds, as previously mentioned, are obtained by 3D printing and have a parallelepiped shape with a lower notched base, so as to induce the orientation of the fibers during the casting. Inside them, will be cast the fiber reinforced concrete. The formworks are divided into 7 categories according to the number and size of the teeth. From the rectangular parallelepiped model of reference, the other formworks were created by keeping the total width (116 mm) and length (360 mm) identical and "inserting" different number of teeth, keeping the overall depth of the cross section always equal to 32 mm. Following the various forms of formwork:

- Reference: REF;
- Type 1: 6 teeth, h_t =15mm;
- Type 2: 9 teeth, h_t =14mm;
- Type 3: 12 teeth, h_t =9mm;
- Type 4: 18 teeth, h_t =5mm;
- Type 5: 24 teeth, h_t =4mm;
- Type 6: 36 teeth, h_t =3mm.

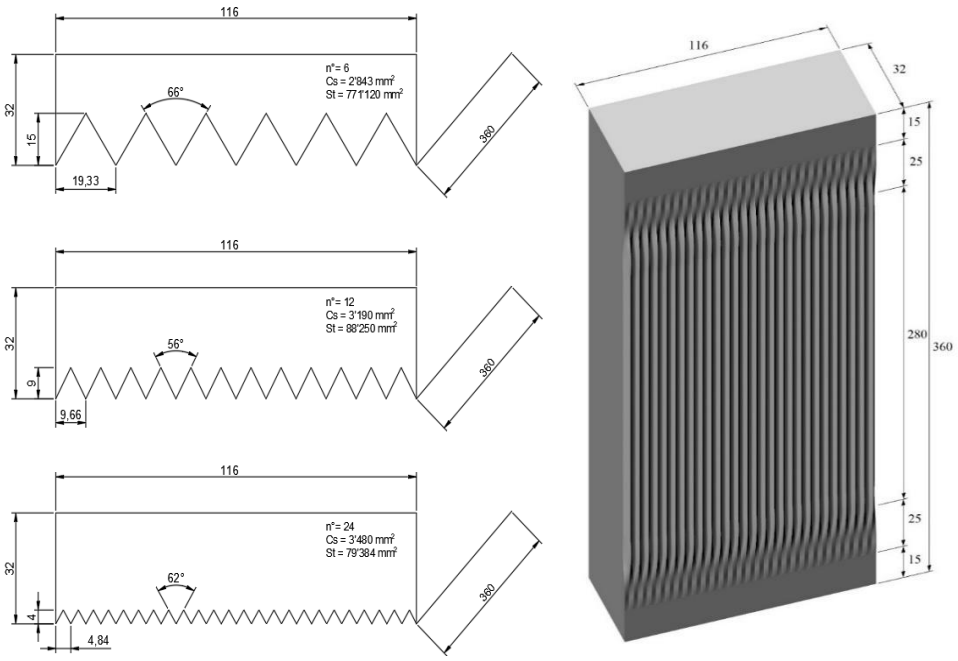

Figure 45 – On the left, cross-sections of three main framework typologies: 6, 12, 24 teeth and on the right, a rendering of a mold

Figure 46 - 3D printed mold, 6 teeth

Figure 47 - 3D printed mold, 12 teeth

Figure 48 - 3D printed mold, 24 teeth

Starting from drawings on a tissue in the laboratory of the building materials department, it was possible to obtain the following formwork construction phases (figure 49).

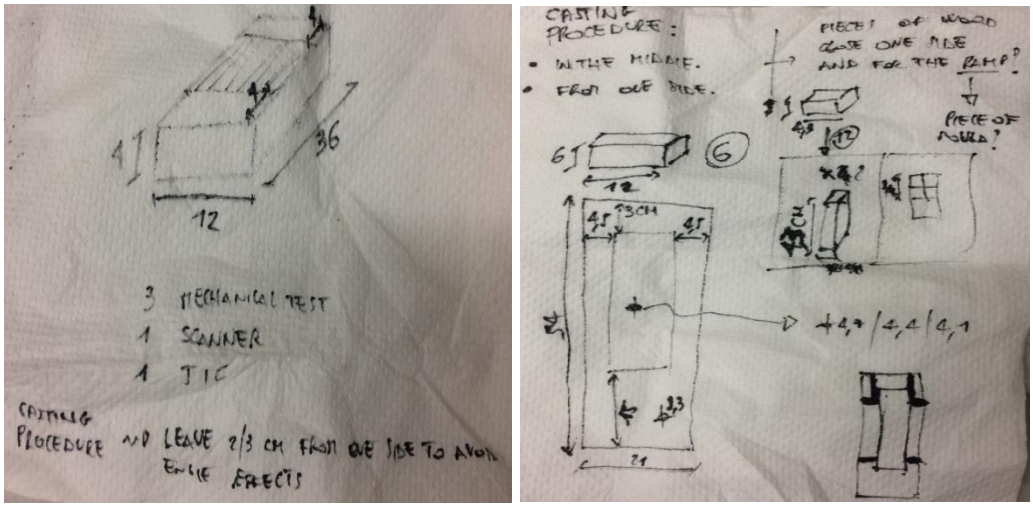

Figure 498 - Sketching ideas of how to cast on a sheet of paper

First of all, the upper side (red) is removed to accommodate the ramp.

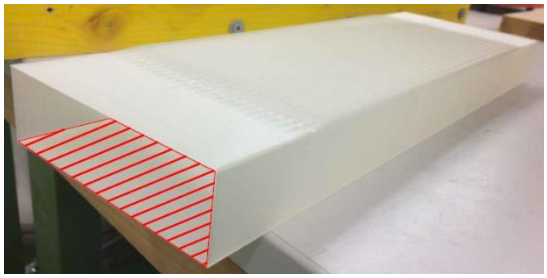

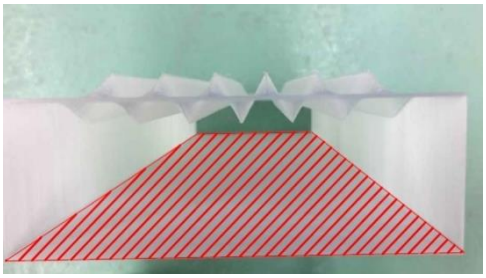

Figure 50 and 51 – On the left, Upper side to remove, view from the side; on the right, upper side to remove, view from the top

Then, to avoid breaking the formwork that is made of material with fragile transverse behaviour, it was decided to place it inside an additional wooden formwork of adequate size.

Figure 52 - Wooden formworks, dim. 210 x 60 x 540 mm

Afterwards, an extension is made to overcome two problems: the "wall effect" on the initial and final area, and the orientation due to the gravity of the casting falling perpendicular to the formwork.

Figure 53 - view of the formwork with double extensions and the piece of wood

As a precaution was also placed a piece of wood to close and stiffen the plastic formwork fixing it with adhesive tape and was added a ramp to ease the casting of the concrete. The ramp was made with the same material employed for the formwork.

Figure 54 - Ramp in PLA for the Fiber Reinforced Concrete casting

Casting procedure

Initially, there was doubt whether to pour the concrete on one side making it flow to the other side or from the center to the ends. The choice fell on the first option for ease of execution and interest for the behaviour of the fibers. On the contrary, a casting from the center would lead to negative mechanical results, because of the force of gravity which inevitably imposes to the fibers orientation a direction orthogonal to the flow. In this way, the phenomenon of "stitching" of the concrete that limits the cracks and increases the performance under load in the center line is not created.

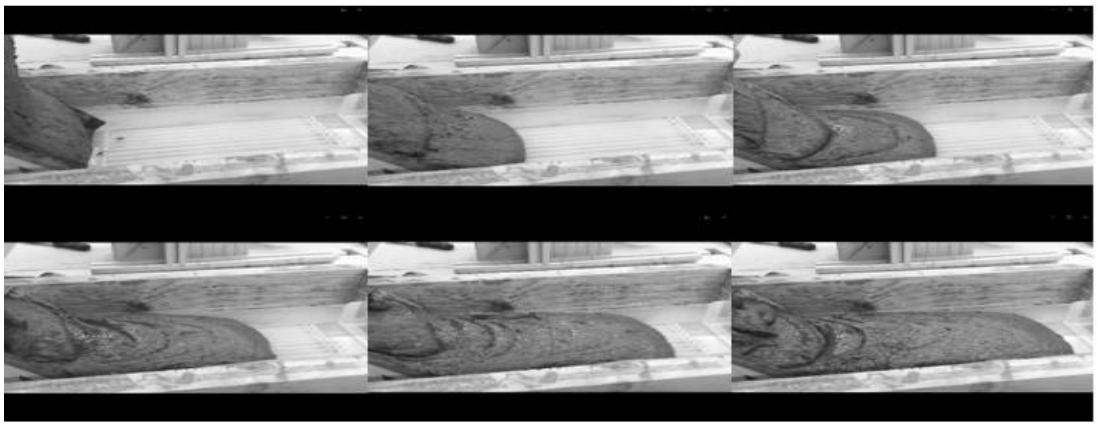

Figure 559 – Black and white snapshots of the flow of Fiber Reinforced concrete cast

In parallel, using the determined mix design , two experiments in a "Y" formwork were carried out. In the first, the concrete was poured inside by gravity and at the same speed (same diameter tubes) from both branches. In the second, the formwork was filled with the concrete, poured at the same speed but with different casting time. First from a pipe and then once it reaches the middle, it was poured from the second one. The idea is to investigate the fibers orientation in the central part of the mock up where the concrete flows are joined.

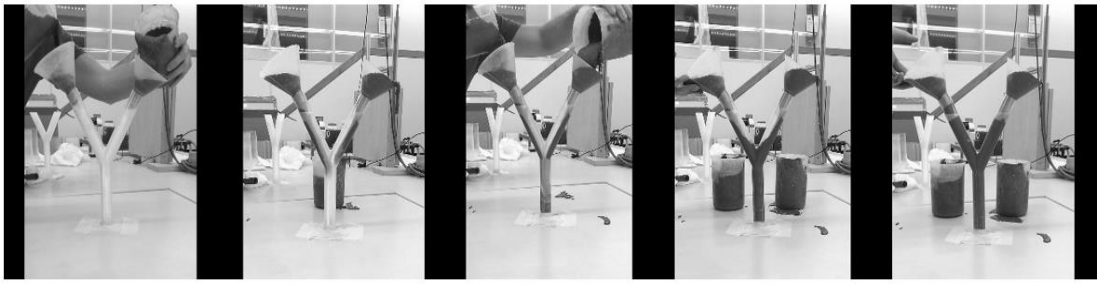

Figure 56 - Casting phases in the Y-shaped formwork

Three-point flexural test

Initially, the idea was of using a smaller test machine with a specimen 40x40x160 mm, then it has been opted for a larger one capable of exerting a pressure of 100 kN. Hence the need to calculate the appropriate dimensions according to UNI EN 12390-1 (dimensional compliance for specimens and formworks) and UNI EN 12390-5 (bending strength on specimens).

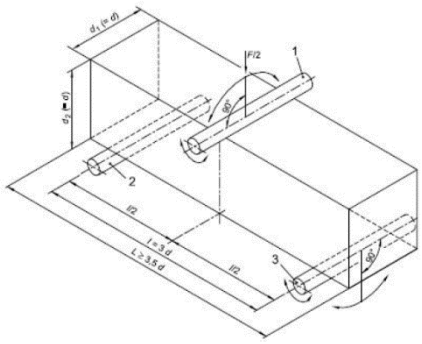

Figure 57 – Three point flexural test

$$V = \frac{2 \cdot d_1 \cdot {d_2}^2 \cdot s}{3 \cdot l}$$

Equation 6 – loading speed V (N/s)

$$f_{cf} = \frac{3 \cdot F \cdot l}{2 \cdot d_1 \cdot {d_2}^2}$$

Equation 7 – flexural strength f_{cf} (N/mm^2)

- s = stress speed (N/mm^{2}s) (value between 0.04-0.06 N/mm^{2}s);
- l = distance between the support rollers (mm);
- d_1 and d_2 = cross section dimensions (mm);
- F = maximum breaking load (N).

As the specimens had been obtained with equal widths but different heights (± 3 mm), the surface was grinded with a 12 cm diameter diamond disk. In this way it was possible not only to make uniform all the specimens, but also to smooth the surface, thus reducing depressions and making it flat for the bending test (avoiding differential surface pressures).

Figure 58 – Surface grinding of the specimens

The three-point bending flexural test provides values for the modulus of elasticity in bending E_f and flexural stress σ_f. The main advantage of a three-point flexural test is the ease of the specimen preparation and testing[49]. However, this method has also some disadvantages: the results of the testing method are sensitive to specimen and loading geometry and strain rate. The bending test have been performed using a German Walter + Bai AG FTS, Form + Test Seider to measure the 28-day strength.

Figure 59 - Setup of the three-point bending test

Figure 60 - Cracking in the middle

The three-point flexural test has been displacement controlled and the procedure was as follows:

- the specimen is placed on the machine with the supports spaced 300mm, so that it is well balanced and centered with the load force operating point (previously a cross was drawn on the surface of the specimen along the center line);

- the various dimensions of the specimen are entered in the database: height, width and length as well as the weight;
- using a manually operated wheel, the machine arm is lowered until it comes close to the point of contact with the specimen;
- the test is started with a speed of 0.001 mm/s until the first cracking is reached, then the speed is increased to 0.01 mm/s and then to 0.02 mm/s up to deformations in the order of 5 mm, finally, the maximum speed is set at 0.08 mm/s until a deformation of 10 mm is reached;
- once the test is complete, the machine arm is lifted, the specimen broken at the centerline is removed and another specimen is replaced.

A drawback during the three-point flexural test was the difficulty in removing the lower part of the formwork in PLA. In specimens with many teeth its removal was avoided to prevent tooth breakage, this inevitably compromised the perfectly elastic-linear behaviour of the fiber reinforced concrete in the first part of the tests.

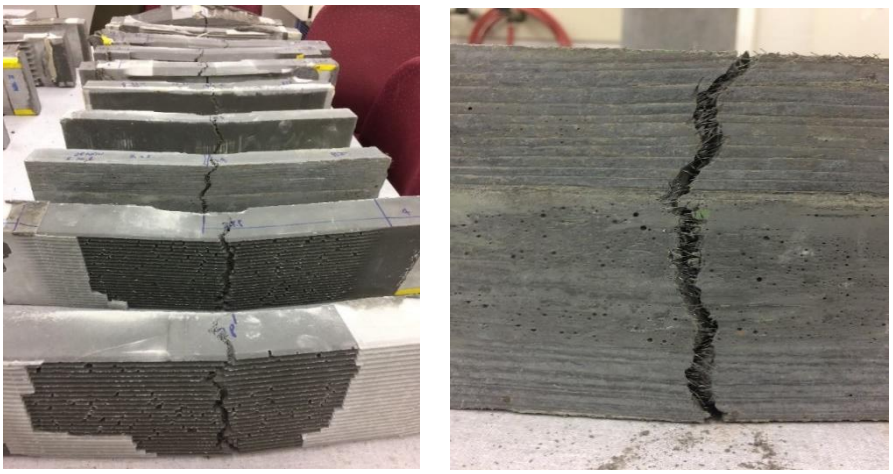

Figure 61 – Specimen broken in the middle

Following two sequences of images with the specimen bending rupture.

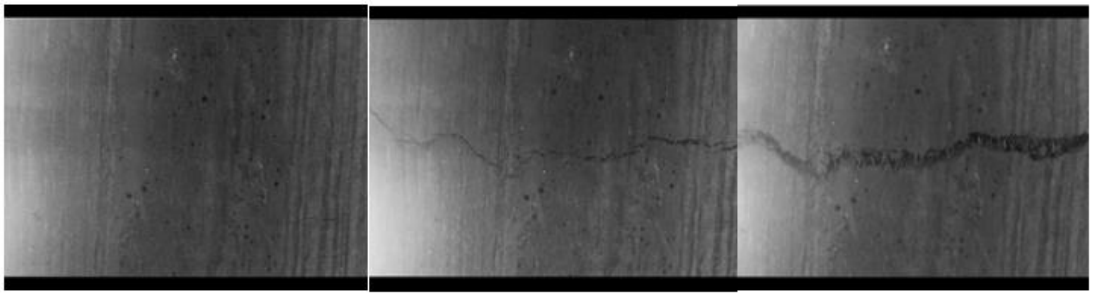

Figure 62 – Bottom view of a sample breaking

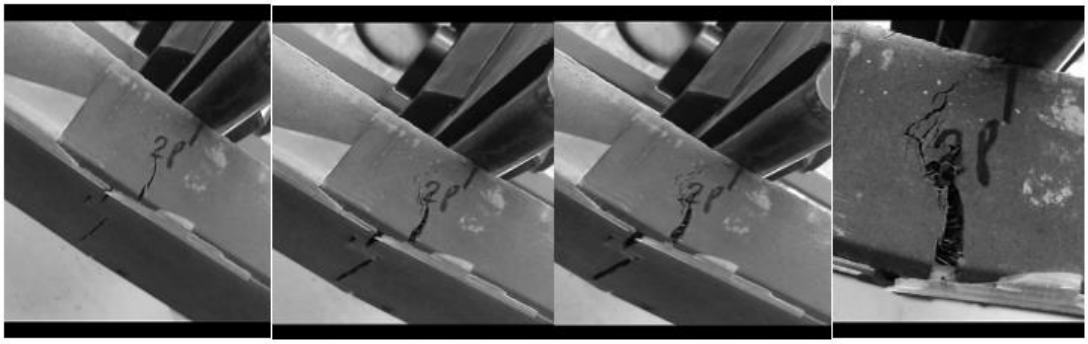

Figure 63 – Side view of a sample breaking

3.2.3 X-ray Computed Tomography (XCT)

After measuring the bending strength of the specimen, it was decided, in order to verify the influence of the orientation of the fibers on the flexural strength, to verify the orientation through tomographic analysis. Parallelepiped specimens should be prepared with a dimension compatible with the tomograph. For this reason, each specimen was cut in three parts along the short side (l_1 = 38.7 mm) and in four parts on the long side (two of l'_2 = 80mm and two of l_2 = 100mm). This resulted into small parallelepipeds with a 4 x 4 cm^2 cross section and a 100 mm length ready to undergo X-ray analysis. A code was written to identify the position of each individual mini-sample with respect to the original sample, paying attention to mark the flow direction. Afterwards, x-ray tomography was performed on each sample.

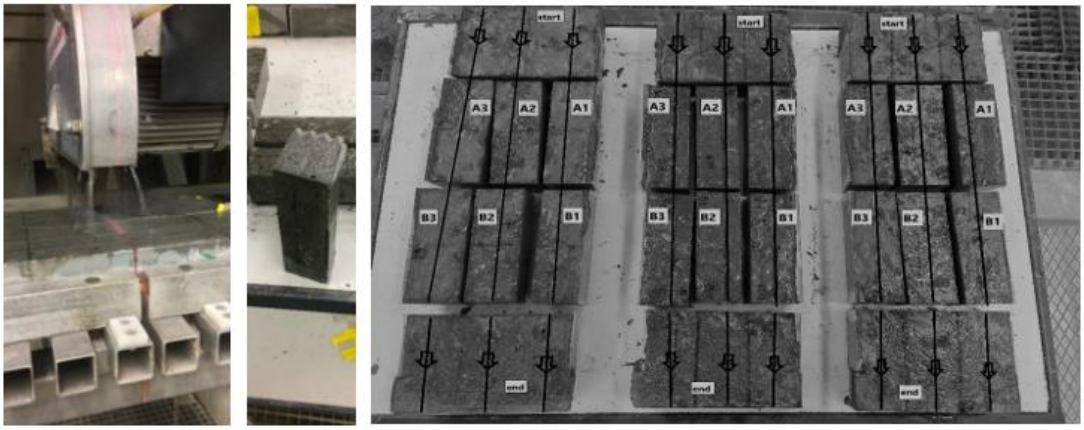

Figure 64 – From the left, transversal cut of the specimen, then parallelepiped 4x4x10 cm^3 and finally10, pieces of specimens ready to be scanned at x-ray tomograph

Introduction

X-ray computed tomography (CT) is a non-destructive technique started with clinical X-ray computed tomography (CT) in 1972 (Hounsfield 1973). Since then, CT technology has rapidly advanced and clinical CT became radiology's powerhouse [48]. In CT a target material (usually a high-atomic-number metal such as tungsten) is bombarded with high-energy electrons produced by a heated filament, as in a standard X-ray "tube". A continuum of X-ray energies is produced due to manifold interactions of the incoming free electrons with bound electrons in the target material. The most dominant interaction produces so-called bremsstrahlung radiation, in which incident electrons decelerate due to interactions with target nuclei (bremsstrahlung arises from the German word *bremsen* for brake). The energy of the resulting radiation depends on the amount of electron kinetic energy transferred by this interaction, and so the X-ray radiation emitted features a broad spectrum of energies up to the maximum energy of the incident electrons (i.e., it is poly-chromatic). The maximum energy is generated when an electron actually collides with the nucleus and all of its kinetic energy is converted to X-ray radiation [50].

The CT is generally used to visualize internal features within solid objects and to obtain digital information on their geometries and 3D properties. A CT image is usually called a slice, as it corresponds to what the scanned object would look like if it were sliced open along a plane. An even better analogy is a slice of a loaf, because just like a slice of bread has a thickness, a slice CT corresponds to a certain thickness of the object scanned. Thus, while a typical digital image is composed of pixels (image elements), an image of a CT section is composed of voxels (volume elements). Taking the analogy further, just as a loaf of bread can be reconstituted by stacking all its slices, a complete volumetric representation of an object is obtained by acquiring a contiguous set of CT slices. The grey levels in an image of a CT slice correspond to the X-ray attenuation, which reflects the percentage of X rays dispersed or absorbed as they pass through each voxel. This is the reason why in a scanned image, objects with a higher CT number result in a grey scale less intense and tending to white color (case of fibers in the HPFRC) while the opposite happens when the attenuation level increases favouring a grey color more intense and tending to black (case of air pockets in the HPFRC). For the X-ray CT an important unit of measurement is represented by the Hounsfield Unit (HU) scale that is a linear transformation of the original

linear attenuation coefficient measurement into one in which the radiodensity of distilled water at standard pressure and temperature (STP) is defined as zero Hounsfield units (HU), while the radiodensity of air at STP is defined as -1000 HU. In a voxel with average linear attenuation coefficient μ the corresponding HU value is therefore given by [51]:

$$HU = 1000 * \frac{\mu - \mu\, water}{\mu\, water - \mu\, air}$$

μ_{water} = the linear attenuation coefficients of water

μ_{air} = the linear attenuation coefficients of air

Equation 8 – Hounsfield Unit

Thus, a change of one Hounsfield unit (HU) represents a change of 0.1% of the attenuation coefficient of water since the attenuation coefficient of air is nearly zero. It is the definition for CT scanners that are calibrated with reference to water. X-ray attenuation is primarily a function of X-ray energy and the density and composition of the material being imaged. Tomographic imaging consists of directing X-rays onto an object from multiple orientations and measuring the intensity decrease along a series of linear paths. This decrease is characterized by Lambert-Beer's law, which describes the reduction in intensity as a function of the X-ray energy, the length of the path and the linear attenuation coefficient of the material.

$$I = I_o * \exp(-\mu x)$$

I = recorded X-ray intensity

I_o = initial X-ray intensity

μ = linear attenuation coefficient of the material

Equation 9 – Lambert-Beer's law for homogeneous material

Equation 9 only describes a homogenous material which, however, in natural samples is rarely encountered. If the object is composed of several different materials, the linear attenuation of each material (u_i) as well as its linear extent (x_i) must be accounted for, resulting in the more general equation. In the case of a monochromatic beam this equation is sufficient to describe the attenuation of the X-ray beam through a heterogeneous object. However, the more typical laboratory setup employs a polychromatic X-ray beam. Because the linear attenuation coefficient is a strong function of X-ray energy.

$I = I_o \exp [\Sigma (-\mu_i x_i)]$

I = recorded X-ray intensity

I_o = initial X-ray intensity

μ = linear attenuation coefficient of the

Equation 10 – Lambert-Beer's law for heterogeneous material

A specialized algorithm is then used to reconstruct the X-ray attenuation distribution in the volume being viewed. The elements of X-ray tomography are a source of X-rays, a series of detectors that measure the attenuation of the intensity of X-rays along multiple-ray paths and a rotational geometry with respect to the object being imaged. Several configurations of these components can be used to create CT scanners optimized for imaging objects of manifold sizes and compositions.

The important characteristics (in which each of them influences the other) of the tube are:

- the target material and the peak X-ray energy;
- the X-ray spectrum that is generated;
- the current;
- the intensity of X-rays;
- the focal point size;
- the spatial resolution.

In general, smaller detectors provide better image resolution, but reduce count rates because of their small area compared to larger ones. The only preparation necessary for CT scanning is to ensure that the object fits inside the field of view and that it does not move during the scan. Because the full scan field for CT is a cylinder (i.e., a stack of circular fields of view), the most efficient geometry to scan is also a cylinder [52].

Strengths

- Entirely non-destructive 3D imaging;
- little or no sample preparation required;
- Reconstruction is generally attenuation-conservative, allowing sub-voxel level details to be extracted.

Weaknesses

- Finite resolution causes some blurring of material boundaries;
- Large geological specimens cannot be penetrated by low-energy X-rays, reducing resolving capability;

- Not all features have sufficiently large attenuation contrasts for useful imaging;
- Image artifacts (beam hardening) can complicate data acquisition and interpretation;
- Large data volumes can require considerable computer resources for visualization and analysis.

XCT scan

The strength and toughness prediction models for fiber-reinforced concrete (FRC) typically assume the spatial distribution of fibers is uniform. However, non-uniform dispersion can greatly affect the FRC's mechanical properties. For quantifying dispersion of synthetic fibers within concrete, a non-destructive technique using X-ray computed tomography (CT) combined with a post-processing image analysis is proposed [53]. Following the procedure used for the 3D image.

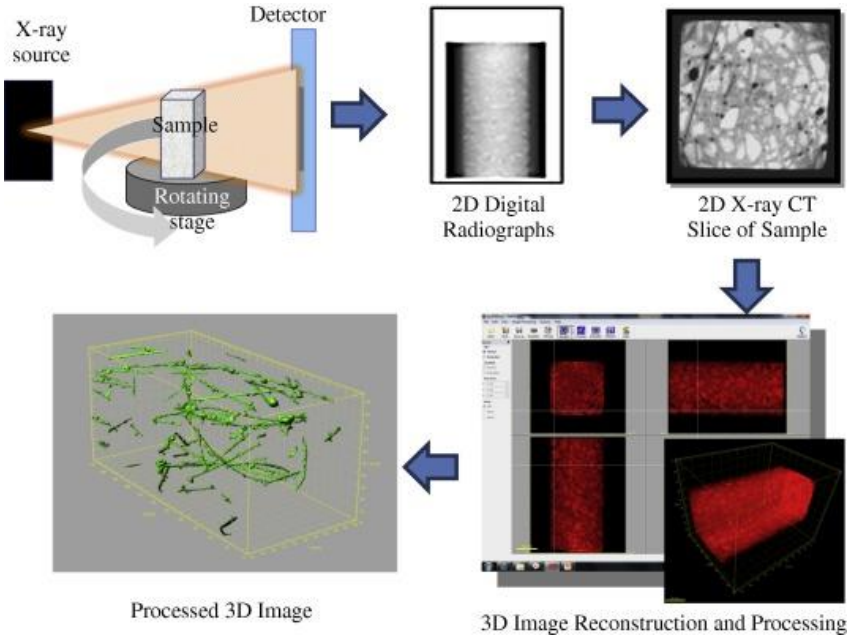

Figure 65 - Procedure used for the 3D image

The XCT scan provides the following steps.

- Positioning of the specimen which must be analyzed on a support with a device that allows rotation during the scan.

Figure 66 - X-ray computed tomography at EMPA

- Setting of all the parameters related to distance from the detector to the specimen and from the source to the specimen;
- Correction of the field of view (the specimen during rotation must always remain visible);
- Definition of voxelsize (in this case 32 micrometres), number of slices to cover the entire region of interest and power of 50 eV;
- Other statistical values of volume height, diameter, generator H and V, imager H and V, rotation and zoom and estimated time required for the scan.

The results are visible in the figure below, which also includes an expected preview of the sample. It is characterized by the fibers (darker) and the matrix (lighter) with bubbles of trapped air.

Figure 67 - Preview of the sample with measurements

Artifacts

The bremsstrahlung and characteristic X-ray radiation actually only represent a small fraction of energy deposited within the target material; the vast majority (> 99%) ofthe incident electron energy is released as heat (Hsieh, 2009). The total X-ray energy output from the target is characterized as the flux (photons/second), although the terms intensity and flux are often used interchangeably (and will be here). While an X-ray tube system is a relatively cost-effective way to generate X-ray radiation, the limited X-ray flux and polychromatic spectrum can lead to imaging artifacts.

Streak artifact

Streaks are often seen around materials that block most X-rays. Numerous factors contribute to these streaks: undersampling, photon starvation, motion and beam hardening. The streaks can be reduced using newer reconstruction techniques or approaches such as metal artifact reduction (MAR). MAR techniques include spectral imaging, where CT images are taken with photons of different energy levels, and then synthesized into monochromatic images with special software such as GSI (Gemstone Spectral Imaging).

Partial volume effect

This appears as "blurring" of edges. It is due to the scanner being unable to differentiate between a small amount of high-density material and a larger amount of lower density. The reconstruction assumes that the X-ray attenuation within each voxel is homogenous. This can be partially overcome by scanning using thinner slices.

Ring artifact

One or many "rings" appear within an image. They are usually caused by the variations in the response from individual elements in a two dimensional X-ray detector due to defect or miscalibration. Ring artefacts can largely be reduced by intensity normalization, also referred to as flat field correction.

Noise

This appears as grain on the image and is caused by a low signal to noise ratio. This occurs more commonly when a thin slice thickness is used.

Beam hardening

It occurs because conventional sources, like X-ray tubes emit a polychromatic spectrum. Photons of higher photon energy levels are typically attenuated less. Because of this, the mean energy of the spectrum increases when passing the object, often described as getting "harder". This leads to an effect increasingly underestimating material thickness, if not corrected. Many algorithms exist to correct for this artifact.

3.2.4 Fiber orientation analysis

Samples and regions to analyze

The 116x32x360mm^3 parallelepiped sample has been divided into eight parts: an initial part (along the casting flow direction) and a final part measuring both 116x80x32 mm^3 and six central ones measuring 39x32x100 mm^3. The focus was on the six central samples, naming them A1, A2, A3, B1, B2 and B3. As regards the parallelepipeds A1 and A3, B1 and B3 a simplification has been carried out. Due to the symmetry an analogue behaviour has been hypothesized. Therefore, the samples considered are A1, A2, B1 and B2. For them, two scans each for a total of eight scans for type.

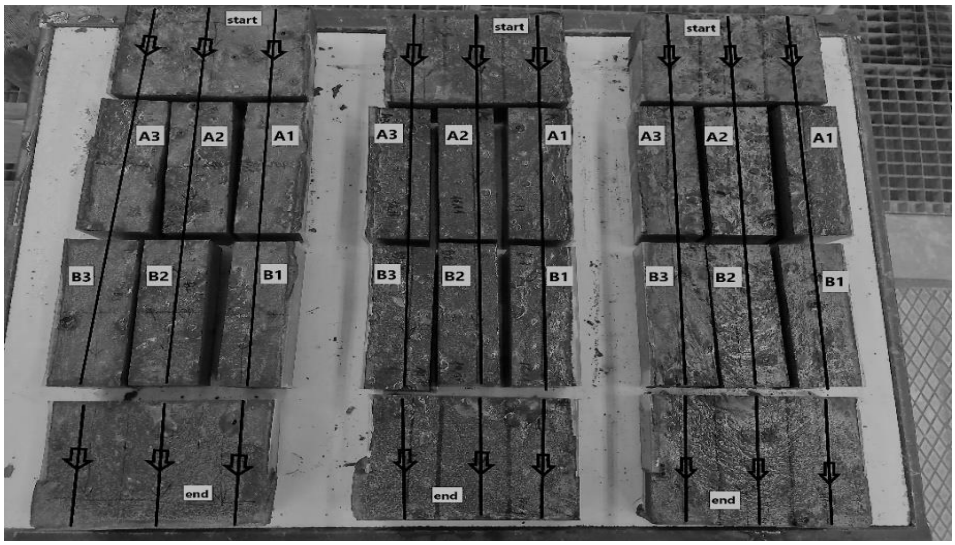

Figure 68 – Division of the samples in subsample

In turn A1, A2, B1 and B2 are named at their start and end parts: A1-A, A1-B, A2-A, A2-B, B1-A, B1-B, B2-A and B2-B. However, since the behaviour of the A1-B / B1-A and A2-

B / B2-A edges is the same, only the A1 samples have been tested (A1-A / A1-B) and A2 (A2-A / A2-B).

Subsequently the final parts B1-A and B2-A were excluded due to the proximity with respect to the parts A1-B and A2-B. B1-B and B2-B edge portions of the original sample were also excluded since it can be realistically hypothesized that they have the same fibre orientation of A1-B and A2-B. This last consideration is given by the fact that the fibers have the possibility to orient themselves up to the central section, beyond which they persist with their orientation [54].

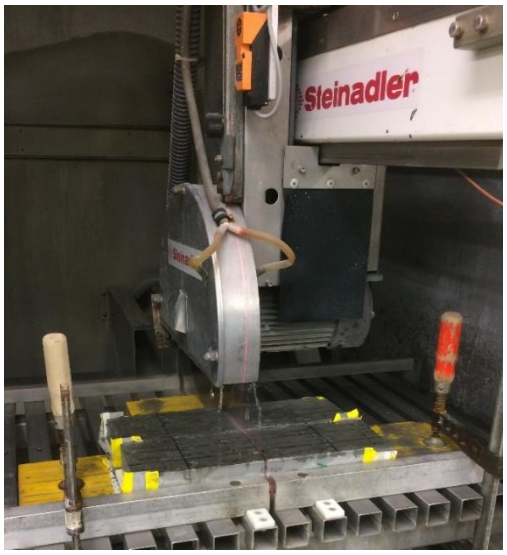

Figure 69 – Cutting machinery and concrete samples in smaller pieces

Therefore, the volume to be analyzed (red part in the picture below) was about 4m3 with a satisfactory amount of fibers inside (four times the length of the fibers). To clarify the scanned parallelepipeds were A1 (A1-A, A1-B) and A2 (A2-A, A2-B).

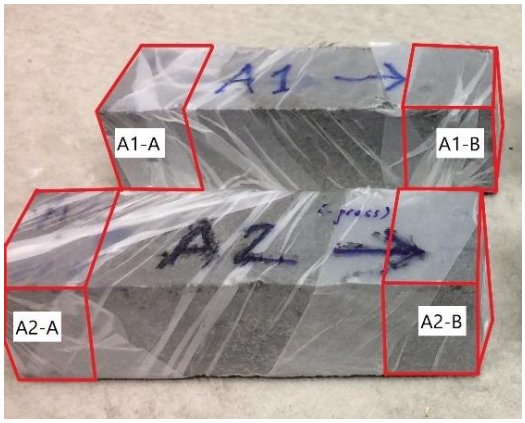

Figure 70 – Reference type with volumes analyzed in red

As regards the regions to be analyzed, it was decided to consider the region of interest (ROI). Depending on the size used, it was then possible to identify the regions concerned:

- one above the tooth called TOP (red);
- one in the center of the tooth called BOT (blue);
- one near the side edge called LAT (yellow).

All three areas taken into consideration besides being influenced by the choice of dimensional aspects (ROI) were also selected for an interest related to the orientation of the fibers within the mortar matrix, in particular for the "wall effect".

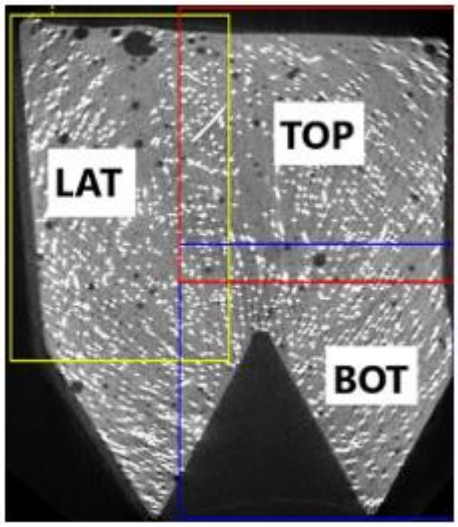

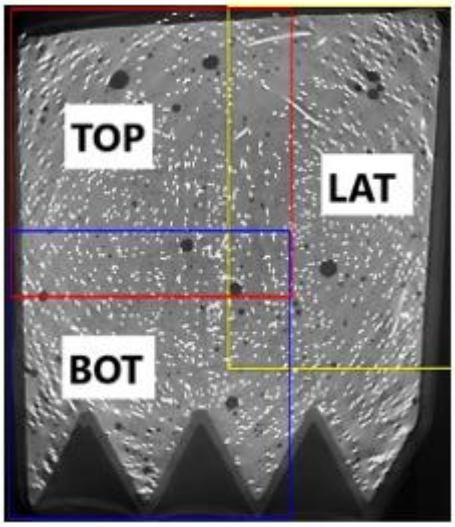

Figure 71 and 72 – Three main ROI in a cross section of simple's type with six and twelve teeth

Avizo

Avizo is a software application that allows users to perform interactive visualization and calculation on 3D data sets. The Avizo interface is modeled on visual programming. Users manipulate form data and components, organized in an interactive graphical representation as a tree structure. The functions of Avizo are highlighted in red, the output files of the related functions are green, while the graphic representations of the output files are shown in yellow and orange. Data and modules can be interactively linked and controlled with different parameters, creating a visual processing network whose output is displayed in a 3D viewer [55]. With Avizo is it possible to automate a model (cylinder correlation) to solve the trend of the fibers (trace correlation lines) inside a cement sample by implementing a

spatial graphic representation. To do this, it uses many algorithms and the user's ability is to optimize the Avizo procedure by using the appropriate input parameters. Thus, the Avizo workflow structure has the following steps:

- Tomogram files;
- Non-local means filter (file filtered);
- Cylinder correlation (correlation, orientation, standard deviation);
- Trace correlation lines;
- Spatial graph statistics

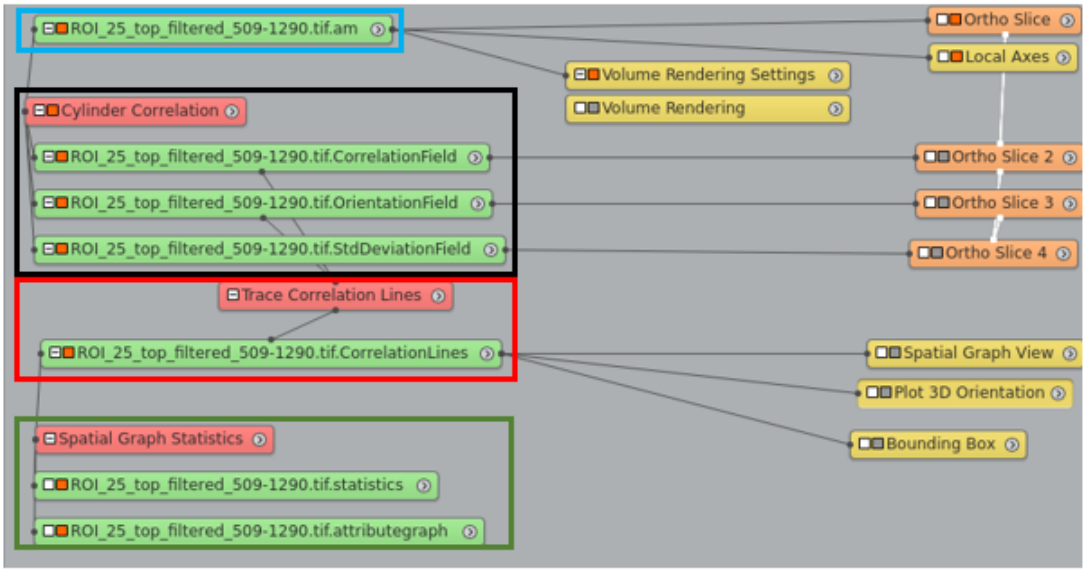

Figure 73 – Tree structure of Avizo interface

Tomogram files

The Avizo input file is a series of tomograms subjected to an adequate correction of the image. A tomogram is nothing more than two-dimensional image produced by tomography, representing a slice or section through a three-dimensional object. Once uploaded the file with the slices of the CT scan it is possible to connect the ortho-slice representation, very convenient to have a pack of the various slices visible in sequence one after the other.

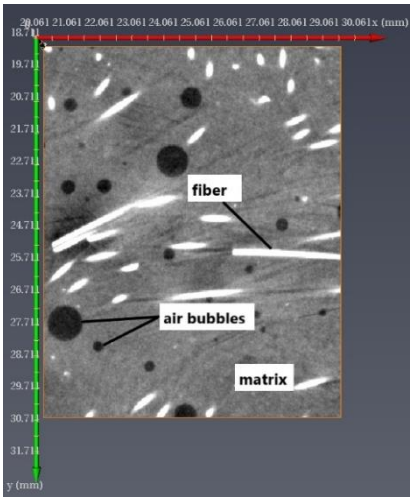

Figure 74 – Ortho slice

Non-local means filter

All the tomograms were submitted to the non-local means filter. Non-local means is an algorithm in image processing for image denoising. Unlike "local media" filters, which take the average value of a group of pixels surrounding a target pixel to make the image uniform, the non-local filter means an average of all the pixels in the image, weighted by the similarity of these pixels with the destination pixel. This translates into greater post-filter clarity and less loss of detail in the image than the average local algorithms [56]. Compared to other well-known denoising techniques, non-local media add "method noise" (i.e. noise reduction process) that looks more like white noise, which is desirable because it is typically less disturbing in the noise product [57].

$$u(p) = \frac{1}{C(p)} \int_{\Omega} v(q)\, f(p,q)\, dq$$

Equation 11 – Filtered value of the image at point p

$$C(p) = \int_{\Omega} f(p,q)\, dq$$

Equation 12 – Normalizing factor

Ω = area of an image

p, q = two points within image

u (p) = filtered value of the image at point p

C (p) = normalizing factor

f (p, q) = weighting function

v (q) = unfiltered value of the image at point q

The Gaussian weighting function sets up a normal distribution with a mean, μ = B (p) and variable standard deviation.

f (p, q) = $e^{-\frac{|B(q)-B(p)|^2}{h^2}}$ h = filtering parameter

B (p) = local mean value of the image point values surrounding p

Equation 13 – Weighting function

Cylinder correlation

A generic cylinder, whose length and diameter must be adapted to the imaging parameters, is used as a template. The cross-correlation involved in the template matching step provides not only a map of cross-correlation coefficients as a measure of the similarity between the template and the local density in the tomogram, but also a map representing the best local orientation of the cylindrical template. These two maps are then used to calculate a similarity function that allows to evaluate the likelihood that two neighboring voxels are connected by a filament. The shape of the cylindrical model must adapt locally to steel fibers. The width of the cylinder is then set by the steel fiber diameter, which is about 15 µm. The length of the model is, however, more critical. Noise and incomplete information restrict the length. If the model is too short, it reacts to all fluctuations, resulting in arbitrary orientations. On the other hand, if the model is too long, it may be missing on a small-scale feature. The entire tomogram is crossed, and a cylinder of appropriate length and diameter is locally adapted to the data, thus determining for each voxel the orientation in which the cylinder is more similar to the image. A formulation of this local cross-correlation function has been described that allows a fast calculation (Roseman, 2003) [58] and serves as a basis for the algorithm used. Voxels with high cross-correlation coefficients should appear as linked regions along the track of a filament. In practice, however, these regions are interrupted due to imaging imperfections, such as noise. Intuitively, it is assumed that the neighboring voxels belong to the same filament if both have a high cross-correlation and the coupled cylinders are similarly oriented [59].

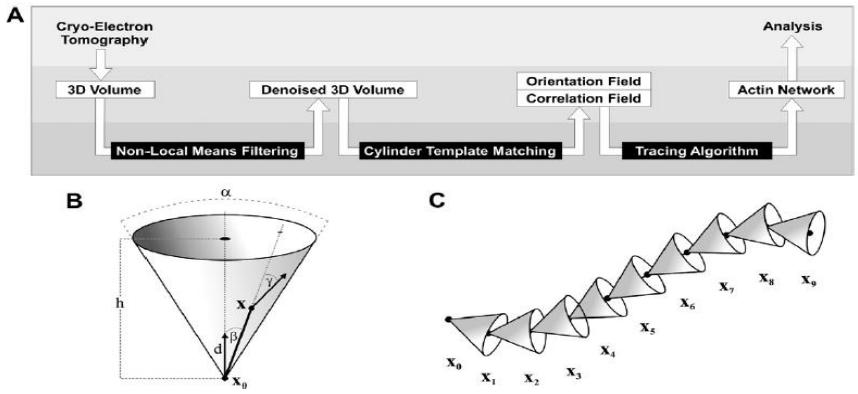

Figure 75 – A) Automated segmentation workflow and C) Algorithm principle. B) Illustration of the algorithm used for microtubule centerline extension. Arrows d: orientations computed by template matching. β, Υ: angles between potential line and orientations. h: length of search cone. x_0: current last point on computed line. x: candidate voxel in the search cone

Angular sampling is the angular frequency with which the semi-sphere is sampled (low is accurate). the other values regulate the mask to be associated as a model around the fibers (mask, outer, inner cylinder radius). A small consideration on the missing wedge correction that represents the impossibility of the projections to be acquired over full tilt angle range with HPFRC samples in electron microscopy [59]. CT image reconstruction can be considered an ill-posed problem because of this missing information. This results in artifacts, seen as the loss of three-dimensional (3D) resolution in the reconstructed images. Finally, the correlation and orientation field are respectively the normalized cross correlation for each voxel and the orientation of the model that precedes the maximum correlation.

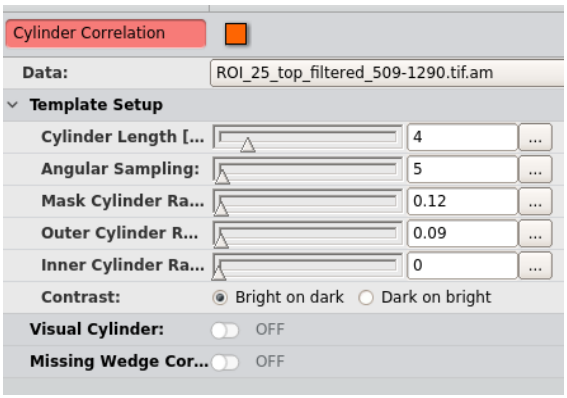

Figure 76 – Template setup of cylinder correlation function on Avizo

Trace correlation lines

The second step of the segmentation process is a new tracing algorithm scanning all voxels for possible connection on the basis of the similarity function. The correspondence of the models produces a double consequence. On the one hand, the map of the highest local cross-correlation, in which the negative values are set to zero and the positive values are interpreted as the probability that a filament passes through the voxel. On the other hand, the orientation field is indicated, in which a vector is assigned to each voxel that indicates the orientation of the model for the highest cross-local correlation. Finally, starting from these two considerations a similarity function is calculated that evaluates the probability that two neighboring voxels belong to the same filament. The definition of this similarity function follows an idea by Fischer and Buhmann (2003). Assuming that the voxel in position x_0 belongs to a filament, the probability for a voxel in x of being part of the same filament is defined as:

$$S(x, x_o) = CC(x)\, C(x, x_o)\, L(x, x_o)\, D(x, x_o)$$

Equation 14 – Similarity function

CC (x) denotes the non-negative value of the local cross correlation coefficient, which is weighted by functions C, L and D, called as co-circularity, linearity, and distance, respectively:

$$C(x, x_o) = e^{-\frac{[\beta(x_0) - \Upsilon(x)]^2}{{\sigma_c}^2}}$$

Equation 15 – Co-circularity function

$$L(x, x_o) = e^{-\frac{[\beta(x_0) + \Upsilon(x)]^2}{{\sigma_L}^2}}$$

Equation 16 – Linearity function

These functions are calculated from two angles $\beta(x_0)$ and $\Upsilon(x)$, from the difference vector x - x0, and from three user-defined parameters σ_C, σ_L and σ_D. $\beta(x_0)$ and $\Upsilon(x)$ denote the angles between the vector $x - x_0$ and the orientation of the model at x_0 and x. The angles are calculated from the orientation field. The co-circularity condition C evaluates the smoothness of the filament: a small deviation between two consecutive orientations

increases the probability, while a node reduces it. The user may prefer smoother lines by choosing a small σ_C parameter. Since equally β (x_0) and Υ (x) dimensions are a condition with a smooth but strongly bent line, a further condition is necessary that evaluates the deviation from a straight line. The linearity function L favours straight lines with small values of β (x_0) and Υ (x) and a small parameter σ_C. The distance function D limits the tracing process towards the voxels x close to the current base point x_0, since a line extension is more likely in the close neighbourhood. The user can enforce this condition by selecting a small value for σ_D. The overall tracing process works as follows. The local cross correlation values are sorted in descending order and the voxel x_0 with the highest correlation value is chosen. Then, the tracing process starts in the forward and backward direction given by the orientation map at position x_0. The tracer continues the line at point x with the highest similarity value S (x, x_0) in the search cone. This is repeated until no point is found for which S (x, x_0) is above a pre-defined threshold t_1. The parameter t_1 restricts the voxels in the search cone that need to be considered. The size of the search cone and its opening angle by the inequalities D (x, x_0) > t_1 and L (x, x_0) > t_1.

$$D(x, x_o) = e^{-\frac{||x - x_0||^2}{{\sigma_D}^2}}$$

Equation 17 – Distance function

The cone height h is given by the maximum over all points x in the search cone, namely:

$$h^2 \leq -\sigma_D^2 \log(t_1)$$

Equation 18 – Cone height

A similar calculation and setting $\beta = \frac{\alpha}{2}$; $\Upsilon = 0$ in L (x, x_0) yields the opening angle α:

$$\alpha^2 \leq -4\sigma_L^2 \log(t_1)$$

Equation 19 – Opening angle

After the trace of a line is finished, a binary mask representing the tracked steel fibers volume is updated and the tracking process continues with the point in the correlation map that has the second highest correlation value, and so on. The general tracking procedure ends when the next initial voxel has a correlation value lower than a predefined threshold t_2. During the trace correlation lines, the algorithm identifies false positives and false negatives for a tracing by establishing correspondences of points between the tracing and a

reference tracing [60]. For each point p in one line set, it is searched for points in the other line set that are close to p. It is called p matched, if it is found a point q in the other line set within a small radius of p. It has been defined the set of false positives (FP) as all points in the tracing that were not matched (red dots). The set of false negatives (FN) contains points in the reference that are unmatched (blue dots).

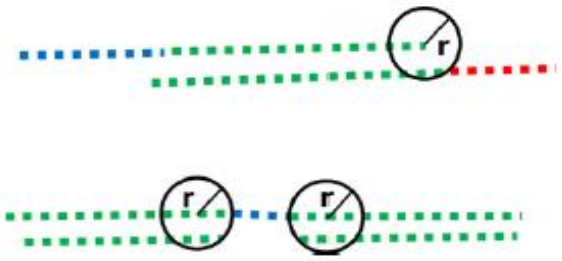

Figure 77 – The upper line represents the case in which two fibers do not belong to the same direction, while the lower line is the case in which two fibers belonging to the same direction are divided.

In the trace correlation lines template, many values are used in the cylinder correlation template. The minimum seed correlation function provides the sensitivity of the algorithm applied, using a high value causes more fibers to be obtained while a low value with less fibers. The minimum continuation quality function influences the length of the fiber, since it acts on false positive and false negative points (a high value makes fibers longer, while a low one produces shorter fibers). Finally, the direction coefficient function affects the shape of the fibers (a high value indicates the presence of very curved fibers, while a low value of straight fibers).

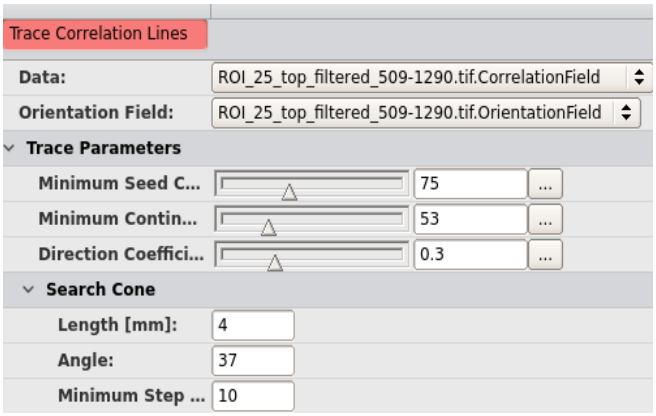

Figure 78 – Trace correlation lines function

Spatial graph statistics

An important thing to evaluate is the duration of the manifold processes. The cylinder correlation takes about 30 minutes because it uses the fastest processor, while the trace correlation lines takes 2h or more depending on the amount of data that the processor must calculate (using the other processor). The spatial graph statistics function, in addition to allowing a graphical representation (3D plot, spatial graph and 3D rendering) provides statistics on the fibers present in the dataset of the starting tomograms. Through two different tables (attributegraph and statistics) different information is provided on the number of nodes, points and segments or graph summary and statistics.

	Node ID	X Coord [mm]	Y Coord [mm]	Z Coord [mm]	Coordination Number
1	0	11.84	4.992	9.44	1
2	1	4.896	21.824	24.96	1
3	2	9.024	20.128	1.472	1
4	3	12.448	22.048	22.272	1
5	4	14.272	4	0.256	1
6	5	6.432	21.472	24.928	1
7	6	6.08	22.816	0.448	1
8	7	0	24.512	15.808	1

	Point ID	X Coord [mm]	Y Coord [mm]	Z Coord [mm]
1	0	11.84	4.992	9.44
2	1	11.488	5.216	9.6
3	2	11.104	5.44	9.76
4	3	10.752	5.664	9.92
5	4	10.4	5.888	10.08
6	5	10.08	6.144	10.24
7	6	9.696	6.464	10.432
8	7	8.576	7.648	11.008

Figure 79 – Attributegraph: nodes and points

	Segment ID	CurvedLength [mm	MeanRadius [mm	Volume [mm^3	OrientationTheta	OrientationPhi	SubgraphID	ChordLength [mm	Tortuosity	TensorXX	TensorYY	TensorZZ	TensorXY	TensorXZ	TensorYZ
1	0	25.9911	0	0	49.5179	111.401	0	23.925	1.08636	0.129372	0.463321	0.407307	-0.160068	-0.133679	0.353893
2	1	22.2053	0	0	11.1393	25.7964	1	21.1672	1.04904	0.0920091	0.02846	0.879531	-0.0077102	0.146036	0.0770781
3	2	32.3945	0	0	37.9265	114.079	2	31.2321	1.03722	0.0699334	0.327574	0.602493	-0.141976	-0.172501	0.383615
4	3	16.9899	0	0	22.4063	164.633	3	16.6064	1.0231	0.158634	0.0207242	0.820642	-0.0246748	-0.314155	0.0923355
5	4	23.396	0	0	6.42123	172.028	4	22.8983	1.02174	0.0373397	0.0163207	0.94634	0.00100201	-0.102629	0.0148092
6	5	22.3603	0	0	19.9588	0.76248	5	21.9047	1.0208	0.144262	0.00333687	0.852401	0.00327545	0.296188	0.00343369
7	6	9.47696	0	0	13.4101	11.7908	6	9.44157	1.00375	0.0542455	0.00641068	0.939344	0.0106048	0.218474	0.0455681
8	7	9.80975	0	0	61.8757	169.515	7	9.77766	1.00328	0.74783	0.0295197	0.22265	-0.137545	-0.405094	0.0751482

Figure 80 – Attributegraph: segments

	Number of Nodes	Intermediate Nodes	Terminal Nodes	Branching Nodes	Isolated Nodes
1	6268	0	6268	0	0

	Number of Subgraphs	Number of Segments	Mean Length	Mean Radius	Total Volume	Total Length
1	3134	3134	14.510123	0	0	45474.726562

Figure 81 – Statistics: graph summary and node statistics

	Graph ID	Number of Segments	Mean Length	Total Length	Number of Nodes	Intermediate Nodes	Terminal Nodes	Branching Nodes	Isolated Nodes
1	Graph0	1	25.991058	25.991058	2	0	2	0	0
2	Graph1	1	22.205334	22.205334	2	0	2	0	0
3	Graph2	1	32.394508	32.394508	2	0	2	0	0
4	Graph3	1	16.989935	16.989935	2	0	2	0	0

	Segment ID	Curved Length	Chord Length	Tortuosity	Orientation Theta	Orientation Phi	Graph ID	Tensor XX	Tensor YY	Tensor ZZ	Tensor XY	Tensor XZ	Tensor YZ
1	0	25.991058	23.925003	1.0863554	49.517941	111.40113	Graph0	0.129372	0.46332067	0.40730733	-0.16006768	-0.13367875	0.35389253
2	1	22.205334	21.167194	1.0490447	11.139346	25.796438	Graph1	0.092009075	0.028460016	0.87953091	-0.0077102035	0.14603558	0.077078126
3	2	32.394508	31.232098	1.0372185	37.926498	114.07856	Graph2	0.069933377	0.3275739	0.60249275	-0.14197589	-0.17250051	0.38361543
4	3	16.989935	16.606396	1.0230958	22.406284	164.63324	Graph3	0.15863362	0.02072423	0.82064217	-0.024674846	-0.31415507	0.092335492
5	4	23.395967	22.898272	1.0217351	6.4212284	172.02843	Graph4	0.037339672	0.016320655	0.94633967	0.00100201	-0.10262928	0.014809231

Figure 82 – Statistics: graph statistics and segments statistics

A filament is comparable to a spatial graph. Within it there are more subgraphs consisting of a set of points (nodes) which together constitute in turn edges (segments). If two segments share a point, the latter is called an intermediate node; while if more than two segments have at least one node in common, this is called branching node.

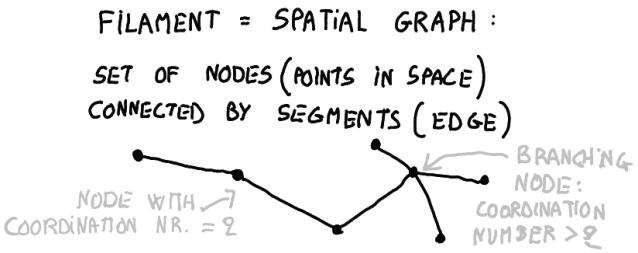

Figure 83 – Spatial graph representation, branching node

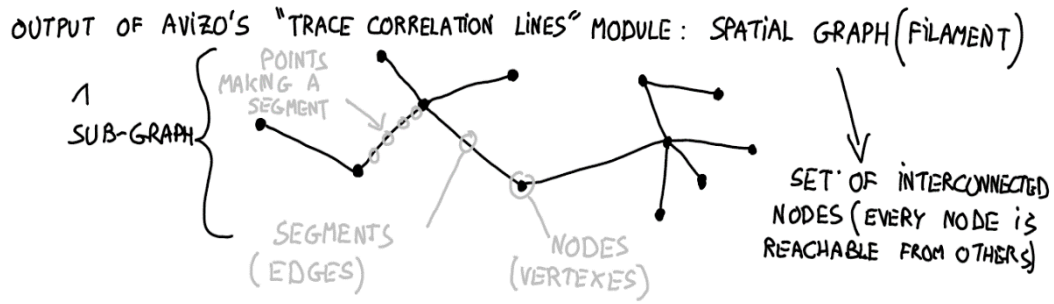

Figure 84 – Spatial graph representation of subgraph with segments, nodes and points

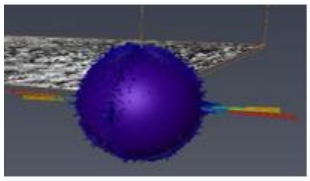

Figure 85 – 3D orientation plot

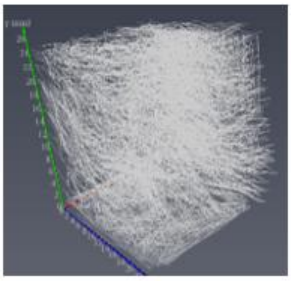

Figure 86 – Spatial graph

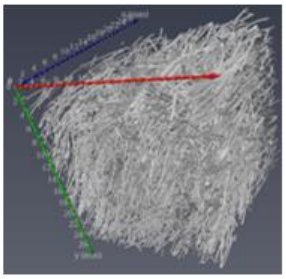

Figure 87 – 3D rendering

Due to problems concerning the waiting time of the analysis in Avizo, it was decided to use shape tensor analysis function, based on using eigenvalues and eigenvectors associated to the stress matrix acting on the model of ellipsoid connected to the model fiber, so it could be possible to obtain the orientation of the fibers as spherical coordinates (theta and fi) and other useful data. Once again, the Avizo sw to provide satisfactory results took too long: whole days of analysis.

ImageJ

ImageJ is a Java-based image processing program with an open architecture that provides extensibility via Java plugins. It can display, edit, analyze, process, save, and print 8-bit color and greyscale, 16-bit integer, and 32-bit floating point images. It can read all the image file formats. ImageJ supports image stacks, a series of images that share a single window, and it is multithreaded, so time-consuming operations can be performed in parallel on multi-CPU hardware [63].

With the use of ImageJ - Fiji it was possible to perform the following operations:

- Create a mask around specimen region (plugin image calculator);
- Create a crop region or rotate the specimen (fig 88);
- Create a binary image sequence (fig 89);
- ROI size analysis (crop plus create a sub-stacks);
- Create a volume mask with outside region voxels set to zero (fig 90);
- Disconnections fibers within specimen (fig 91);
- Shape tensor analysis (BoneJ plugin then particle analyzer).

Regarding the disconnection of particles, it was necessary to make a careful choice of the parameter that influences the algorithm used to separate the particles (fibers). When used

with high values there was the risk of separating the fibers too much in several points, while with low values some fibers were not separated. This function is very useful for distinguishing the fibers from each other in such a way as to associate an orientation after each one. Labeled image sequences are created. In the shape tensor analysis, instead, using the BoneJ plugin it was not possible to obtain satisfactory results, probably due to the complexity of fibers and density present inside the samples. Finally, in both the Avizo and ImageJ software, difficulties were found in time (too long to obtain acceptable results) and in information obtained insufficient for the thesis purpose. The direction to reach the goal of having the orientation of the fibers seemed to have run aground. Then came the idea to use a program of a researcher at EMPA, Beat Münch, written in Java and able to provide the long-hoped for information. Downsides of ImageJ are the incompatibility with Avizo, indeed the output obtained by ImageJ and introduced in Avizo was not recognized by the latter.

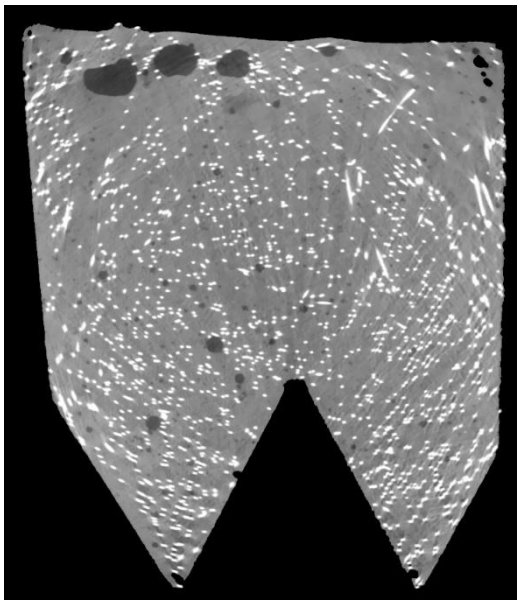

Figure 88 – Cropped_ filtered image

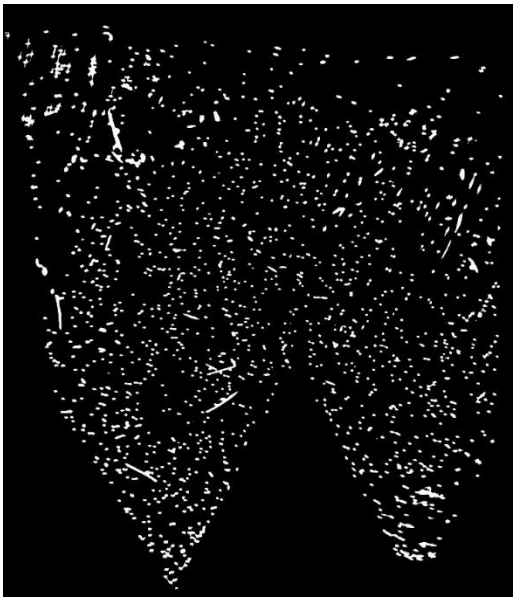

Figure 89 – Binary image

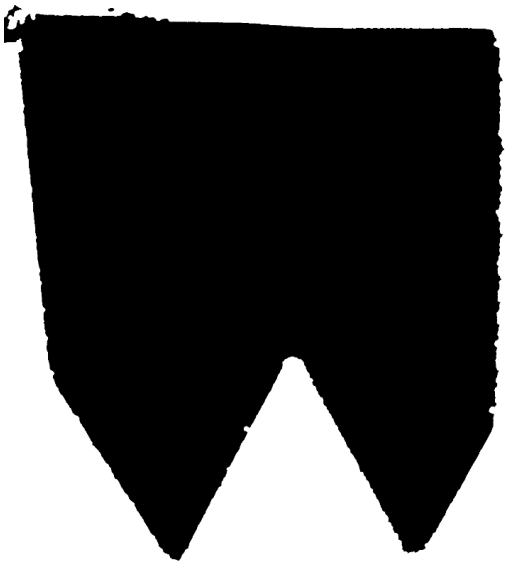

Figure 90 – Mask volume

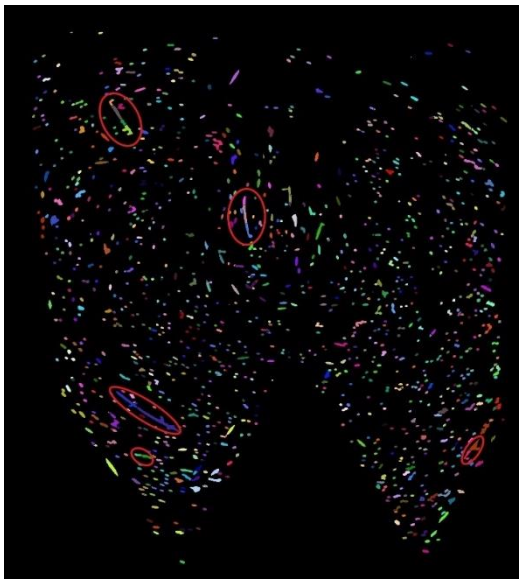

Figure 91 – Labeled image with fiber division

ROI analysis

One of the functions performed on ImageJ - Fiji is the ROI size analysis. With this function it is possible to identify the ROI, Region of Interest, to be submitted to fiber orientation analysis. Subsequently, based on its size, it was possible to place the VIO (Volume of Interest) where it was necessary. In our case, the ROI was placed inside the tooth, above it and close to the side wall of the HPFRC sample for reasons already previously explained. Regarding the ROI size analysis, it was decided to start from the center of the sub-stack and the sequence of filtered tomograms and proceeded as follows:

- Image rotation;
- Cropping image;
- Set voxel around specimen to zero (using the plugin segment phases 3D);
- Segment the fibers (calculating the number of voxels of the fibers by means of a histogram function);
- Percentage computation of the volume of fiber for full specimen with volume mask (calculating the number of voxels in the region entered by the sample boundary);
- ROI size analysis.

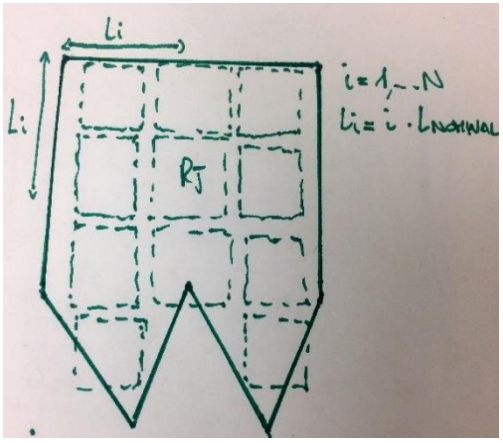

Figure 92 – ROI inside the cross-section

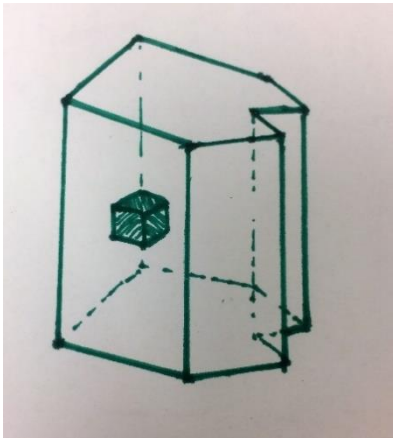

Figure 93 – ROI in the middle of specimen

The ROI size analysis is given by the ratio between the number of voxels of the fibers in the ROI and the number of voxels of the volume mask. An analysis was also performed on the ratio between the number of voxels of the fibers in the ROI and the number of voxels of the matrix in the ROI. This type of analysis was performed on the four sequences of scanned tomograms (A1-A, A1-B, A2-A and A2-B) and for three types of specimens (type1: 6 teeth, type2: 12 teeth and type3: reference) from a ROI of 10 mm (313 x 313 x 313 voxels) up to a ROI of 32 mm (1000 x 1000 x 1000 voxels).

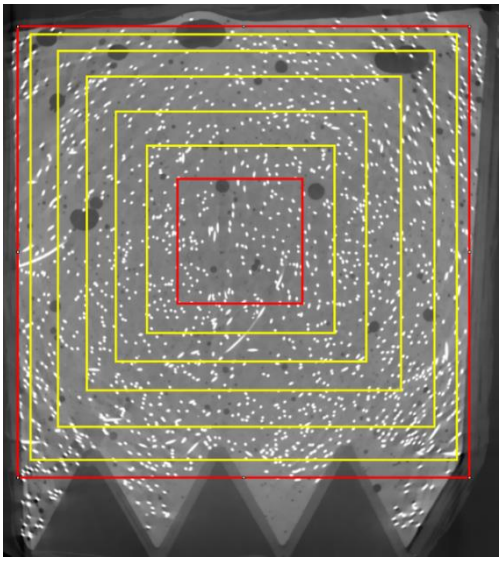

Figure 94 – ROI from 10 mm to 32 mm

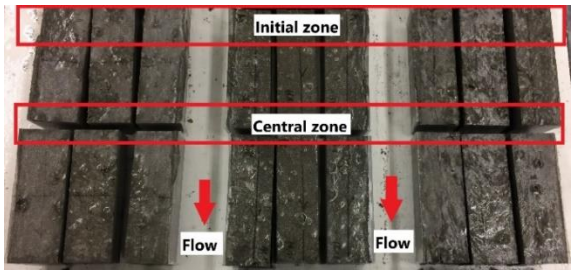

Figure 95 – Zones of interest along the flow

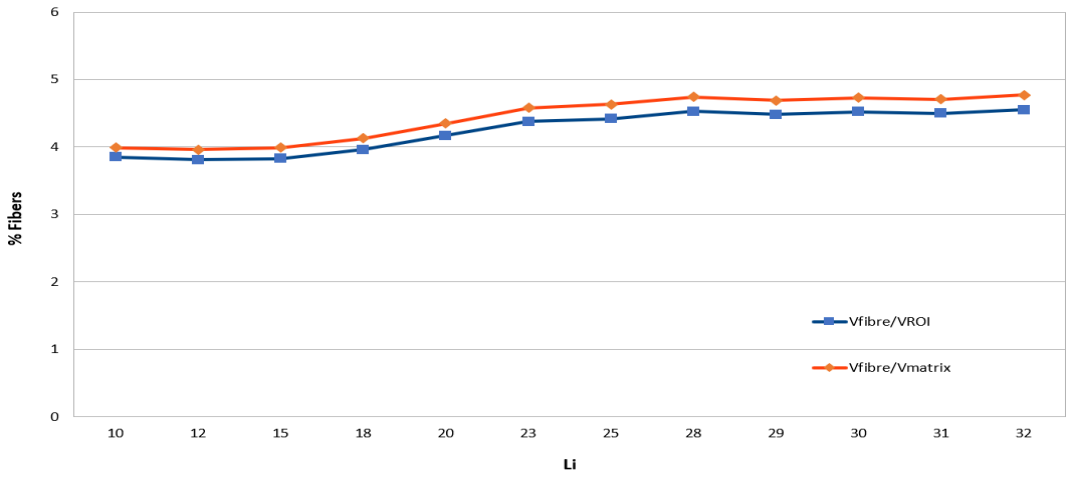

Table 11 – Tomogram A1-A_type 1. In this graph the plateau is reached over ROI of 30 mm. It was decided to take a ROI of 25mm to speed up the calculation of the program and to avoid excessive overlapping of the ROIs.

From the trend of the graphs it has been noticed that the ratio between the voxel's fiber ROI and the voxel total ROI or the ratio between the voxel fiber ROI and the voxel matrix ROI increases as the size of the ROI increases until a plateau is reached. In common to all three types of sample and areas of interest (start and sample center) is the ROI 25 mm (313 x 313 x 313 voxels). It was decided to use this ROI as optimal to avoid considering a region that breaks the fibers and excessive overlapping of the ROIs. Another reason is the increase of speed with the calculation of the program. Finally, an aspect that should not be underestimated is the limit given by the size of interest (inside and above the tooth as well as on the side of the sample) and the timing that is required by the analysis.

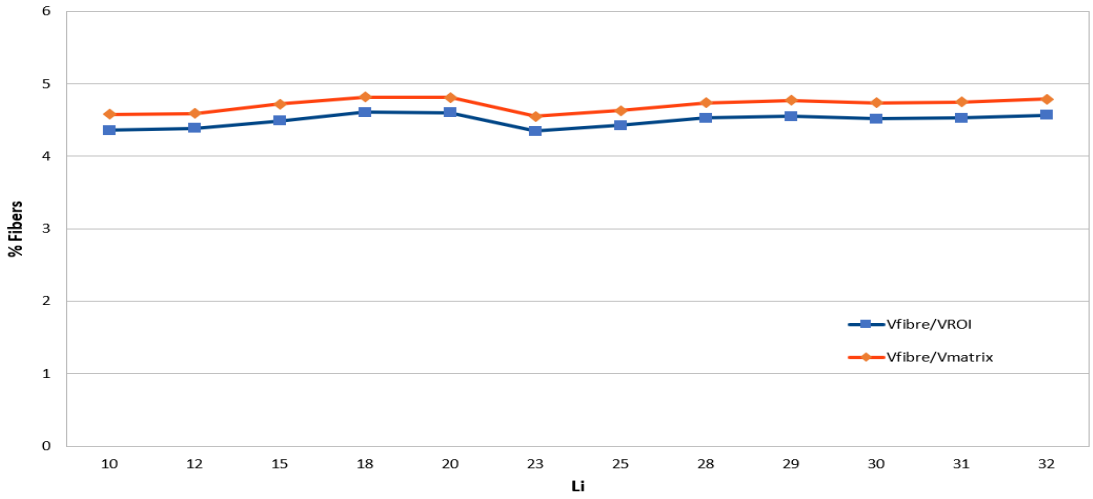

Table 12 – Tomogram A1-A_type 2. In this graph the plateau is reached over ROI of 28 mm. Between the ROI of 20 mm and 28 mm there is a drop in the percentage of fibers in the volume of the ROI due to the surface rising by an air trapped bubble

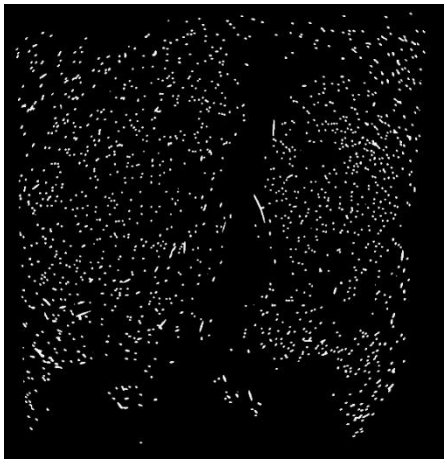

Figure 96 – Space without fibers generated by an air bubble

Figure 97 – ROI marked in red

Sometimes it happens that because of the because of trapped air bubbles rising to the specimen free surface during the setting time, the result of the analysis is compromised (figures above and below). Once the ROI is increased, the problem is no longer visible. For the experiment it was tried to perform the analysis in the sub-stack of interest with ROI 25 obtaining satisfactory results. For the fiber orientation analysis of the third type of as the cube one was used a ROI of the same volume (with same interval sub-stack and ratio between the two edges lower then 1.5). An interesting discovery was that the Avizo sw sometimes identifies fibers placed outside of the sample volume due to artifacts. A way to avoid this is to identify a mask and make the voxels out of the volume boundary all the same and equal to 0, so that SW Avizo certainly does not identify any fiber in that region.

Density analysis

An analysis was carried out with AVIZO on the density of the fibers inside each sample. The procedure is simple: from a sequence of binary images and from a binary mask of the sample volume it was possible to obtain as output a sequence of images representing the cluster of fibers in the matrix for each slice. From this analysis a rendering vision of the entire sample was obtained with the variety of fibers inside it. Below there is a table summarizing the percentage of local fiber volume for each type of sample and divided by part of interest. Remember that from mix design the percentage of fiber volume within the mix was 3.80 %.

Type	Part	fibers number	voxels number in mask volume	Volume fraction percentage
1	A1-A	83211659	1672676658	4,97%
1	A1-B	100399136	1772407569	5,66%
1	A1-C	75652678	1843513143	4,10%
1	A2-A	84886263	1718772737	4,94%
1	A2-B	99869687	1795261458	5,56%
1	A2-C	73293084	1824525633	4,02%
2	A1-A	80339832	1776964190	4,52%
2	A1-B	105426469	1833316247	5,75%
2	A1-C	69899444	1656853049	4,22%
2	A2-A	82845883	1715270944	4,83%
2	A2-B	99702963	1758562421	5,67%
2	A2-C	66221152	1625489627	4,07%
3	A1-A	55470934	1213046074	4,57%
3	A1-B	85736897	1650472070	5,19%
3	A1-C	48734154	1408082484	3,46%
3	A2-A	57058740	1252365590	4,56%
3	A2-B	89575411	1756245822	5,10%
3	A2-C	49947897	1275635415	3,92%

Table 13 – Percentage of local fiber volume for each type of sample

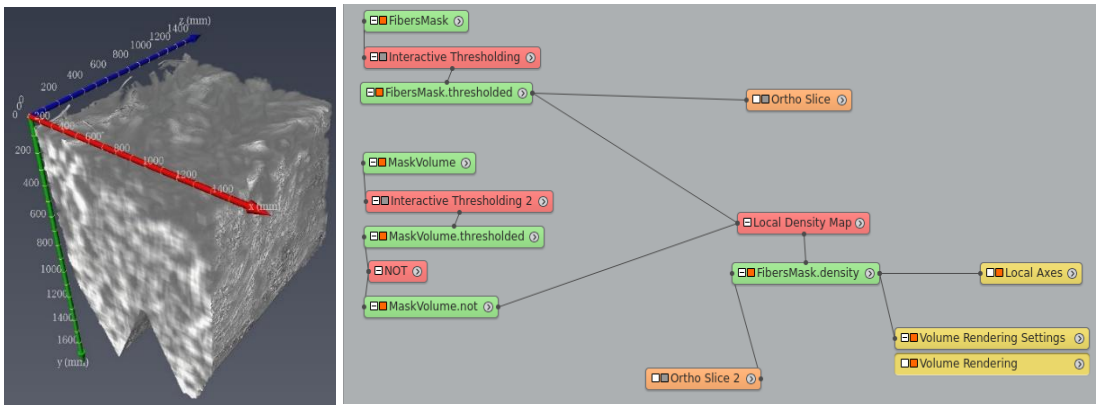

Figure 98 – Avizo local density map on right and rendering result on left

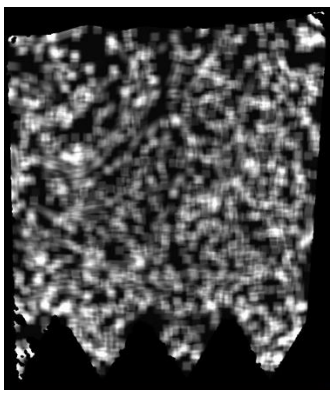

Figure 99 – Local density map for 2nd type

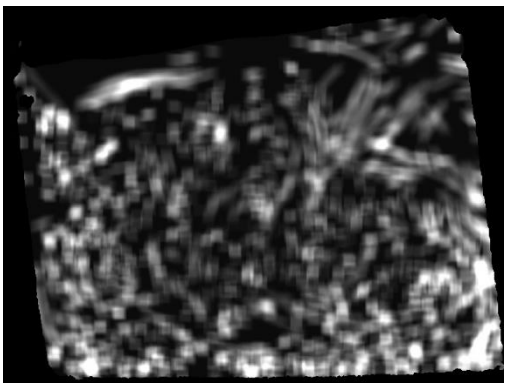

Figure 100 – Local density map for reference type

For all three sample typologies, an almost homogenous fiber volume fraction was measured, with an average equal to 4.73%, (25% greater than the theoretical value). It is not a precise value but is closed to the percentage value of volume fraction of the fibers calculated during the mix design. Higher values were found near the specimen edges, even 20% higher than the reference volume fractions were found, due to the effects on the flow of the cementitious matrix of the non-planar mould bottom.

Moment tensor analysis - Java class Beat's program

After a lot of time spent on Avizo, it has been realized that with the cylinder correlation and the trace correlation lines, the desired results were not achieved since the parameters included in the trace correlation lines must have a compromise of quality and risks. It was decided to use a program written by a researcher at EMPA Beat Münch in Java class [62][63][64], which is a process of programming through Java with which to obtain quickly and with acceptable reliability the required information. Moreover, once the analysis is finished, starting from binary images of disconnected particles inside a ROI of a cement sample, it is possible to obtain a statistic with a lot of information to be exported on MATLAB and thus obtaining graphs and explanatory diagrams. Then another colleague at EMPA Michele Griffa has perfected the new calculation system, which is based on Java programming and performs a shape tensor analysis of the labeled image of a tomogram. This provides as output data manifold particle statistics concerning inner radius, volume, stress matrix, mass centers and orientation according to spherical coordinates of longitude and latitude (θ e φ).

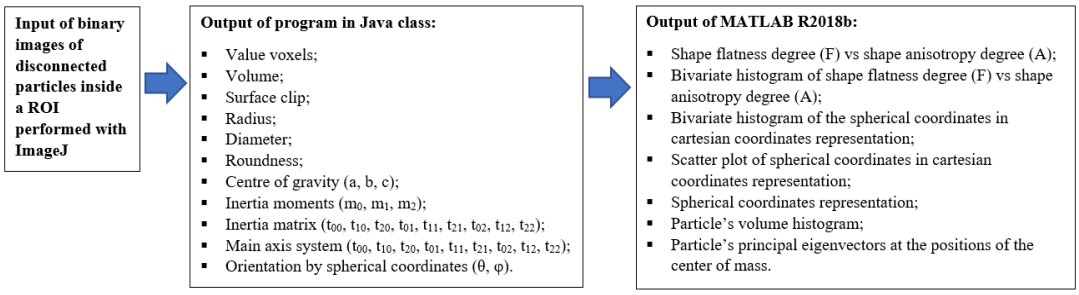

Figure 101 – Processing with program in java class from binary images of disconnected particles to graphic representation in MATLAB R2018b

Moment of inertia

The moment of inertia introduced by Euler in 1765 measures the inertia of the body as its angular velocity changes, a physical quantity useful for describing the dynamic behaviour of rotating bodies around an axis. This size is defined as the second moment of mass with respect to the position. The inertia tensor of an object can have different moments of inertia depending on the rotation axis (I_{xx}, I_{yy}, I_{zz}). These components that are part of the moment of inertia tensor I are defined as [66]:

$$I_{i,j} = \int_{\Omega} \rho(\bar{x})\left[\|\bar{x} - \bar{x_c}\|^2 \, \delta_{ij} - \left(x_i - x_{c,i}\right)\left(x_j - x_{c,j}\right)\right] d\bar{x}$$

Equation 20 – Inertia tensor components

$$X_C = \frac{1}{M}\int_{\Omega} \rho(\bar{x}\,)\, \bar{x}\, d\bar{x} \qquad\qquad M = \int_{\Omega} \rho(\bar{x}\,)\; d\bar{x}$$

Equation 21 – Xc coordinated of mass vector center and mass in this case unitary mass

$x_i\,, \forall_i = 1,2,3.\;\; x_1 = x;\; x_2 = y;\; x_3 = z$

In matrix form:

$$\bar{\bar{I}} = \Gamma_{\Omega}\left(\bar{\bar{G}}\right) \delta_{ij} - \bar{\bar{G}}$$

Equation 22 – Inertia tensor with G gyration tensor

Equation 20 can also be written as follows:

$$I_{i,j} = \int_{\Omega} m_l\left[(x_l)_k (x_l)_k \delta_{ij} - (x_l)_i (x_l)_j\right] d\bar{x}$$

Equation 23 – Inertia tensor components

Where the index l denotes the l_n component of the mass distribution and δ_{ij} is the Kronecker delta. In matrix terms, the equation 23 is written as follow:

$$\bar{\bar{I}} = \sum_{i=1}^{N} m_i \begin{bmatrix} (y_i^2 + z_i^2) & -x_i y_i & -x_i z_i \\ -x_i y_i & (x_i^2 + z_i^2) & -y_i z_i \\ -x_i z_i & -y_i z_i & (x_i^2 + y_i^2) \end{bmatrix}$$

Equation 24 – Matrix of Inertia tensor

For a system of *n* points with mass m_i identified by cartesian coordinates (x_i, y_i, z_i). In our case the mass is considered unitary. Since this tensor is a real symmetric matrix, for the spectral theorem it is possible to find a cartesian coordinate system (an orthonormal base) with respect to which the matrix is diagonal:

$$\bar{\bar{I}} = \begin{bmatrix} I_1 & 0 & 0 \\ 0 & I_2 & 0 \\ 0 & 0 & I_3 \end{bmatrix}$$

Equation 25 – Matrix with principal inertia moment

Where the axes (the matrix eigenvectors) are called axes principals and constants I_1, I_2 and I_3 (eigenvalues) are called principal moments of inertia and are usually ordered in order increasing: $I_1 \leq I_2 \leq I_3$. Calling the unit vectors along the main axes ($\overline{1_1}$, $\overline{1_2}$, $\overline{1_3}$) as rows of the three-dimensional identity matrix, the rotation around that of the main axes of inertia for which the moment of inertia is neither maximum nor minimum, it is not stable. For a homogeneous rotation solid, the axis of rotation is a main axis of inertia. The moment of inertia with respect to any axis passing through the center of mass can also be expressed as the distance from the center to which this axis intersects the surface of an ellipsoid whose axle shafts, oriented along the main axes, are long $\frac{1}{\sqrt{I_1}}$, $\frac{1}{\sqrt{I_2}}$, $\frac{1}{\sqrt{I_3}}$. This ellipsoid is called ellipsoid of inertia.

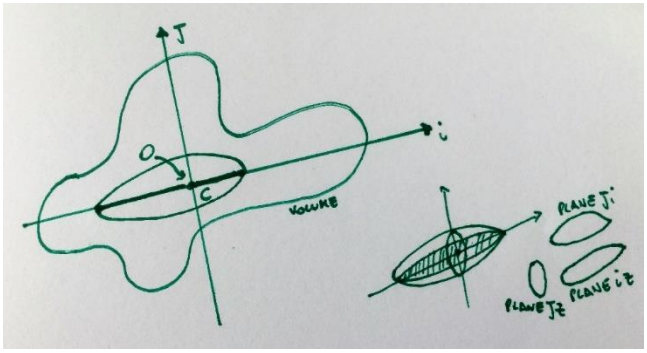

Figure 102 – Ellipsoid of inertia

Fiber orientation

To quantify the orientation of fibers a tensor description method, which is widely used in the fiber-reinforced concrete was applied. Following the orientation state of a single fiber.

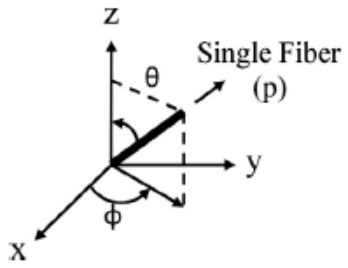

Figure 103 – Orientation state of a single fiber

The orientation state of a single fiber can be defined using in plane (Φ) and out of plane angles (θ), and represented by the following equation:

$$a_{ij} = \frac{\sum (p_i p_i)_n F_n}{\sum F_n} = \begin{pmatrix} a_{xx} & a_{xy} & a_{xz} \\ a_{yx} & a_{yy} & a_{yz} \\ a_{zx} & a_{zy} & a_{zz} \end{pmatrix} \quad i,j = x,y,z$$

Equation 26 – Components of the orientation tensor

In the previous equation a_{ij} stands for the components of the orientation tensor. Parameters p_x, p_y, and p_z give the orientation state of a single fiber in reference directions and are calculated as follows:

$p_x = \sin\theta \cos\varphi$; $p_y = \sin\theta \sin\varphi$; $p_z = \cos\theta$

In-plane (Φ) and out-of-plane (θ) angles for every fiber were measured using an image analysis program. F_n in equation 28 gives the *weighing function* which is used to account for the effect of fiber orientation on the probability of a fiber being intercepted by the cross section under consideration. The probability of being hit depends on the orientation angle. The probability of intercepting a fiber that is aligned vertical to the cutting plane is much higher when compared to a fiber aligned parallel to the section [66]. Therefore, the *appearance function A* depends on the orientation angle θ, and the fiber length L as is seen in equation 27. θ_c *is the cut-off of the appearance function* and it is calculated by using the diameter (d) and length (L) of the fibers.

$$A_{\theta,L} = L\cos(\theta) \quad \text{for} \quad \theta < \theta_c$$
$$A_{\theta,L} = L\cos(\theta_c) = d \quad \text{for} \quad \theta_c < \theta < 90$$
$$\theta_c = \arccos\left(\frac{d}{L}\right)$$

Equation 27 – Appearance functions $A_{\theta,L}$ and the cut-off of the appearance function θ_C

To weight for the measurement data of a single fiber, the data is multiplied by the inverse of the appearance function and the weighting function, F_n was found as follows.

$$F_n = \frac{1}{L\cos\theta} \quad \text{for } \theta < \theta_c$$
$$F_n \frac{L}{d} \quad \text{for } \theta_c < \theta < 90$$
$$\theta_c = arccos\left(\frac{d}{L}\right)$$

Equation 28 – Weighing functions F_n

ParaView

Once the Java class program was used and the necessary statistics were obtained (Figure 104), we proceeded to verify whether the simplified model adopted, based on the inertial ellipsoid and on eigenvectors and values, is effective and reliable. To do this ParaView was used. ParaView is an open-source, multi-platform data analysis and visualization application used to build visualizations to analyze data using qualitative and quantitative techniques [69][70]. In this way it was possible to compare two images overlapping them. One obtained from MATLAB R2018b with an eigenvector of two particles with high volume that have an eccentric curvature, the other obtained from a binary image obtained with Avizo and transformed into rendering. As can be seen in the following figure, the result is satisfactory. Position of the fibers and eigenvector coincide both in the center of mass and in the orientation of the fiber. This additional data obtained by ParaView further strengthens the validity of the program adopted in terms of reliable and realistic results.

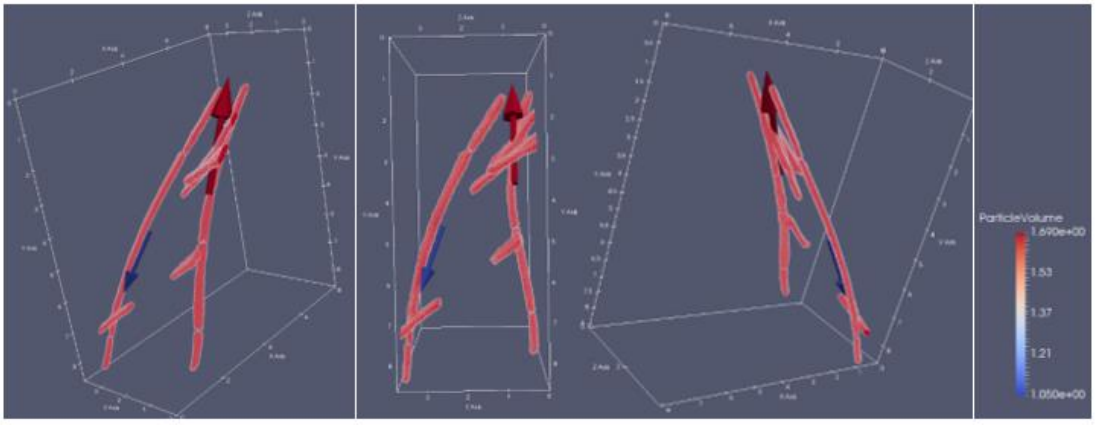

Figure 104 – Validity model adapted. Verification of two eigenvector overlapped two fibers with high curvature in ParaView

CHAPTER 4 – EXPERIMENT RESULTS

A detail description concerning material and methods employed for the university thesis experience has been carried out. Then, was the turn of the formwork formation process using 3D printing method, the casting methods, and x-ray computed tomography. Finally, a java program allowed fiber orientation analysis.
In this section, java program output data and related results will be listed. This will be done both for fiber orientation analysis and for mechanical tests. Afterward, a report cause-effect to define the relationship between fiber orientation and concrete fiber reinforced performance will be outlined.

4.1 Fiber orientation analysis

4.1.1 Output data

The data obtained from the Java program and graphically elaborated with MATLAB R2018b were the following:

- shape flatness degree (F) vs shape anisotropy degree (A);
- bivariate histogram of shape flatness degree (F) vs shape anisotropy degree (A);
- particle's volume histogram;
- particle's principal eigenvectors at the positions of the center of mass;
- bivariate histogram of the spherical coordinates in cartesian coordinates representation;
- scatter plot of spherical coordinates in cartesian coordinates representation;
- semi-spherical coordinates representation.

Shape flatness degree (F) vs shape anisotropy degree (A)

The first two results of the fiber orientation analysis led to a classification of the particles (fibers) according to the model used by the program in Java. For values of A (shape anisotropy degree) that tend to 0, the analogy is with a sphere, for values that tend to 1 is with a cylinder, while for values of A and F (shape flatness degree) that tend to 1, parallelepipeds are obtained.

Shape flatness degree, $F \equiv 1 - \frac{\lambda_3}{\lambda_2}$

Shape anisotropy degree, $A \equiv 1 - \frac{\lambda_3}{\lambda_1}$

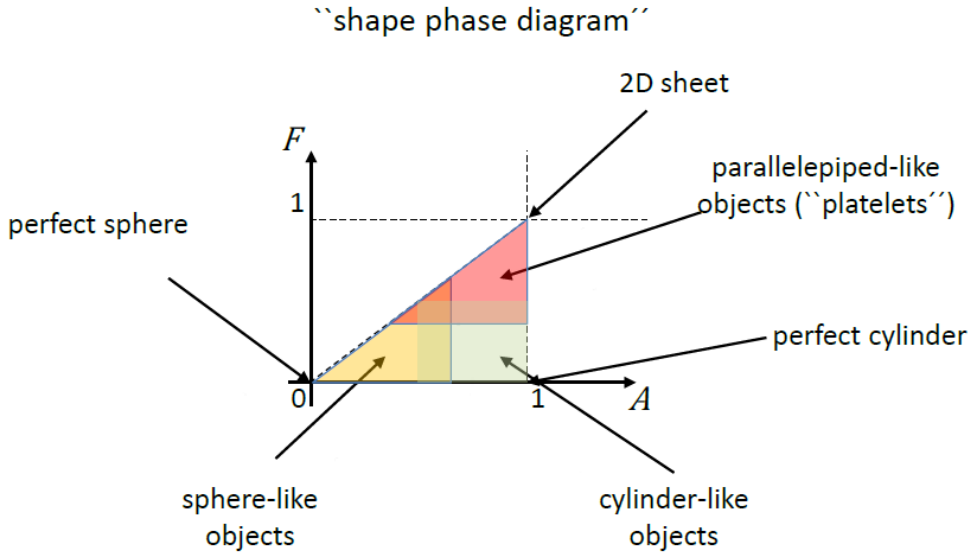

Figure 105 – Particles classification according to shape flatness degree (F) and shape anisotropy degree (A). λ_1, λ_2 and λ_3 are respectively eigenvalues associated to the eigenvectors of the inertia matrix.

As regards the first experience with the parallelepiped specimens and the second experience with the "Y" shaped specimens it was found that most of the fibers from the java model had a cylindrical shape.

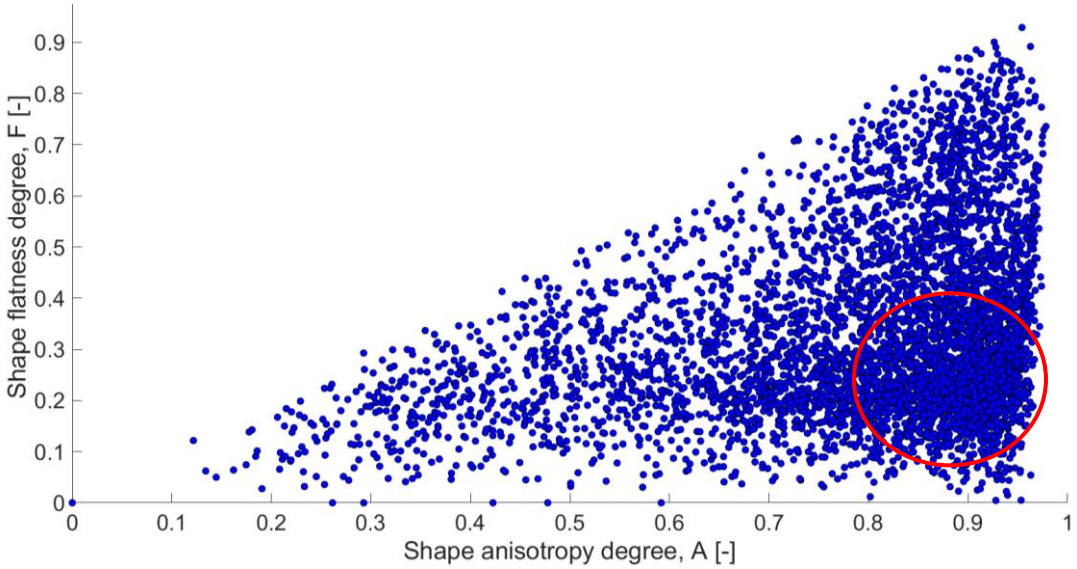

Figure 106 – Shape flatness degree (F) and shape anisotropy degree (A)

Bivariate histogram of shape flatness degree is a representation similar to the shape flatness degree but with additional information related to the number of particles (counts per bin).

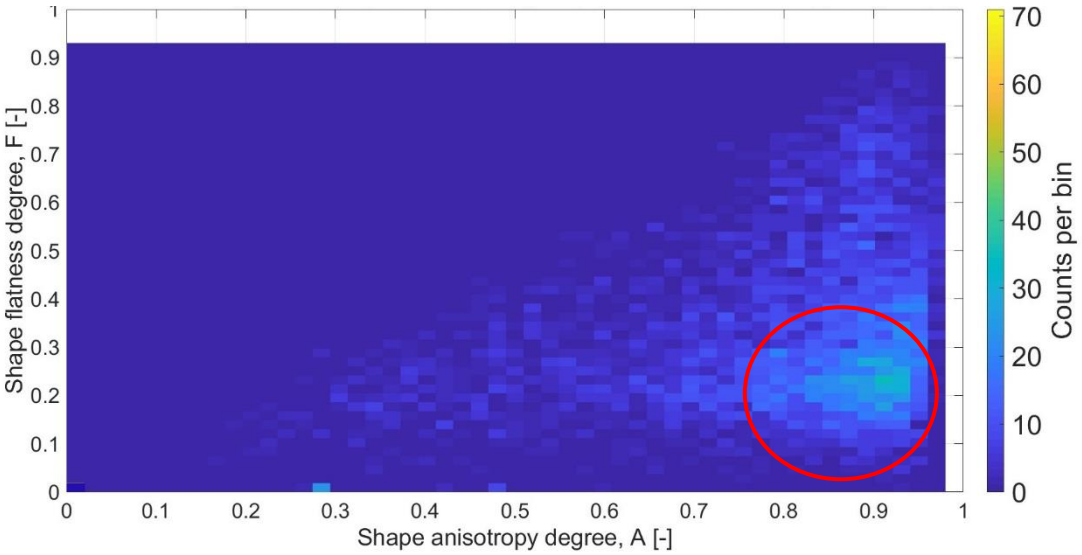

Figure 107 – Bivariate histogram of shape flatness degree (F) and shape anisotropy degree (A)

Particle's volume histogram and principal eigenvectors at the position of the center mass

From the java data output, a graphic representation of the fibers as eigenvectors was obtained (figure 108). The center of the eigenvector is the center of mass of the fiber.

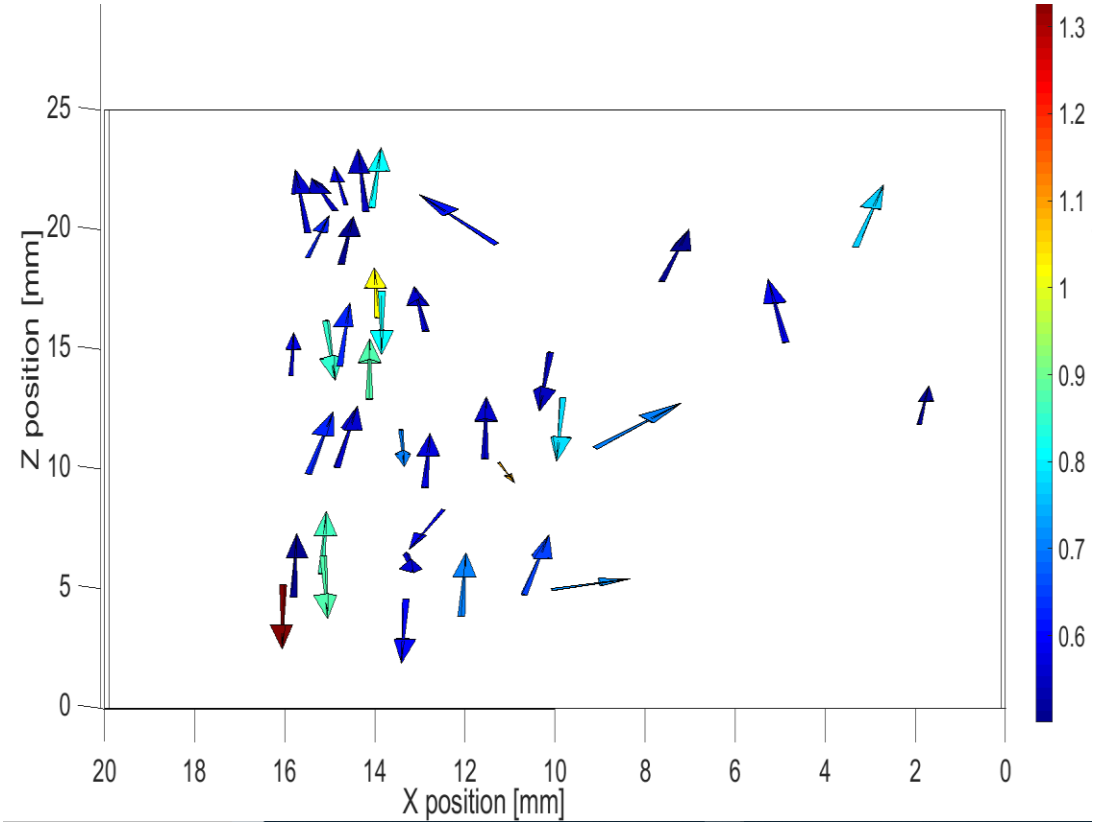

Figure 108 – Particle's principal eigenvectors at the positions of the center of mass. in this case the initial part of the sample was analyzed, as it can see the preferential orientation of the fibers is induced by the force of gravity (the view above is of the cross-section)

Afterward, the volume of fibers was analyzed. The aim of this graphical representation was to investigate the reliability of the method adopted for the analysis of fiber orientation. The data outputs previously obtained represent an overview of each specimen analyzed. Of greater interest is the following analysis which will be dealt with in detail.

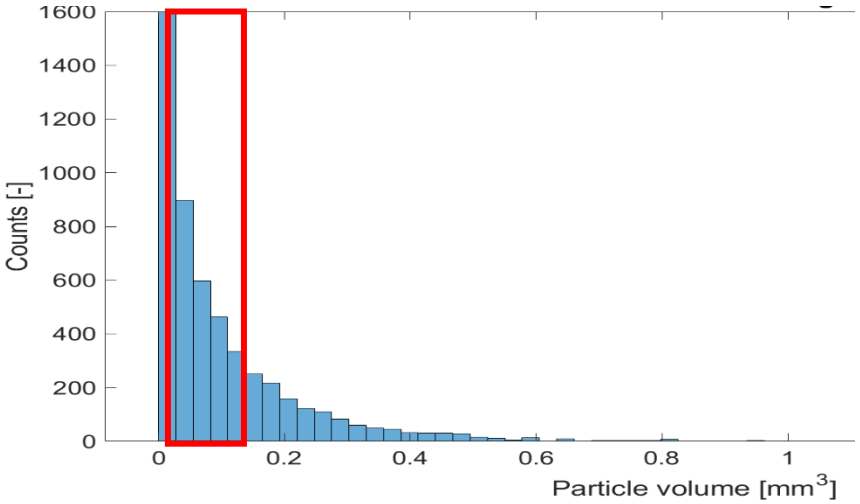

Figure 109 – Particle's volume histogram. In red the real dimensions of the fiber

Bivariate histogram and semi-spherical coordinates representation

The most important result is a classification of the particles according to the orientation in spherical coordinates, angle φ (longitude) and angle θ (latitude). In this case, it was decided to permute (by double rotation) the values of angle θ between 0° and - 90° obtaining only positive values, with a semi-spherical representation. This choice was made for a more orderly graphic representation.

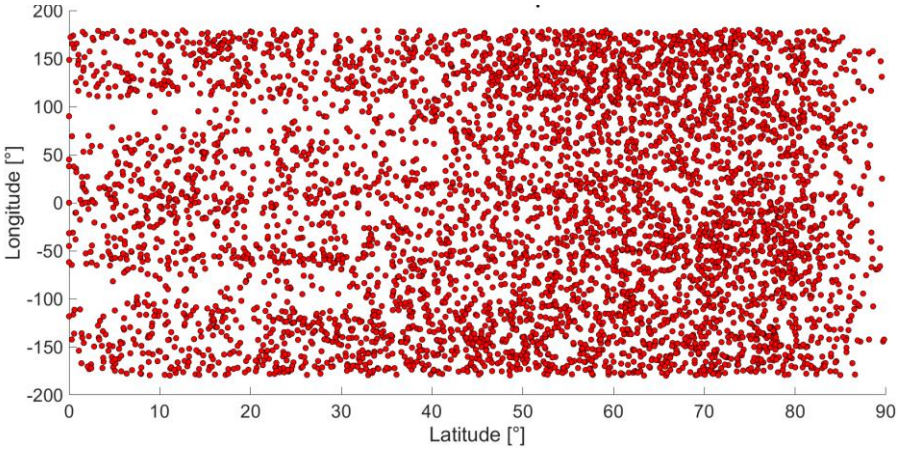

Figure 110 – Scatter plot of spherical coordinates in cartesian coordinates representation. In this representation the cluster of points indicates a prevalent orientation according to the angle φ (longitude) on the y axis and angle θ (latitude) on the x axis.

Following the bivariate histograms and of the fibers orientation in spherical coordinates for the three different typologies of samples analyzed.

- ***T1_I_TOP***. Type 1, top scan of initial part;
- ***T1_I_BOT***. Type 1, bottom scan of initial part;
- ***T1_I_LAT***. Type 1, lateral scan of initial part;
- ***T1_C_TOP***. Type 1, top scan of central part;
- ***T1_C_BOT***. Type 1, bottom scan of central part;
- ***T1_C_LAT***. Type 1, lateral scan of central part;
- ***T2_I_TOP***. Type 1, top scan of initial part;
- ***T2_I_BOT***. Type 1, bottom scan of initial part;
- ***T2_I_LAT***. Type 1, lateral scan of initial part;
- ***T2_C_TOP***. Type 1, top scan of central part;
- ***T2_C_BOT***. Type 1, bottom scan of central part;

- ***T2_C_LAT***. Type 1, lateral scan of central part;
- ***T_REF_I_TOP***. Type reference, top scan of initial part;
- ***T_REF_I_BOT***. Type reference, bottom scan of initial part;
- ***T_REF_I_LAT***. Type reference, lateral scan of initial part;
- ***T_REF_C_TOP***. Type reference, top scan of central part;
- ***T_REF_C_BOT***. Type reference, bottom scan of central part;
- ***T_REF_C_LAT***. Type reference, lateral scan of central part;
- **T_Y_S-S**. Type "Y" casted from the holes at the same time, central part;
- **T_Y_B-A**. Type "Y" casted from the holes at different time, central part.

T1_I_TOP

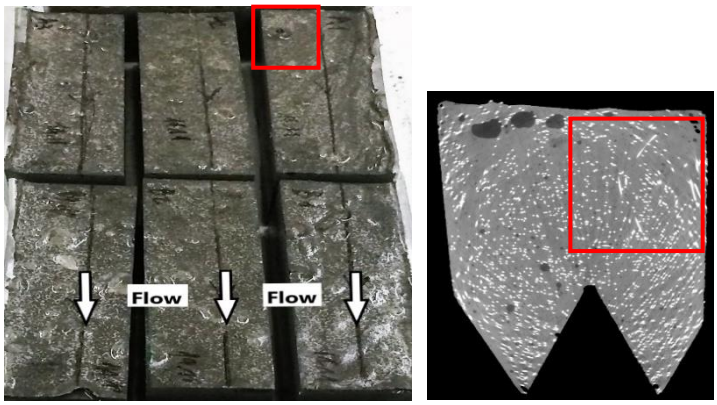

Figure 111 – Navigator of the ROI analyzed. Type 1, top scan of the initial part

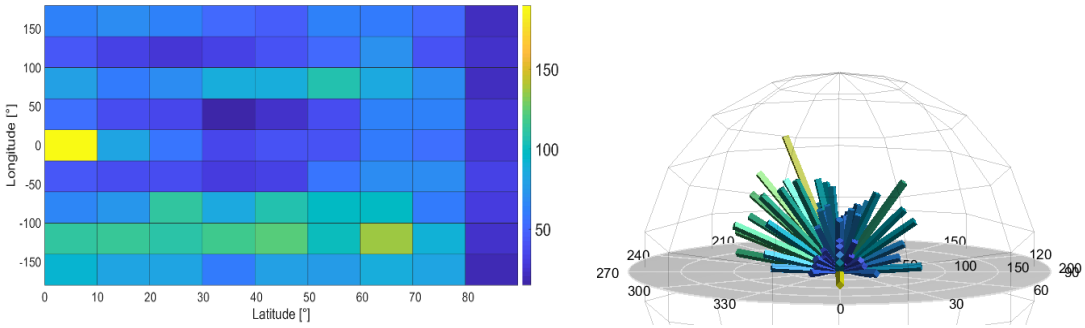

Figure 112 and 113 – Bivariate histogram of the fibers orientation in spherical coordinates and Semi-spherical coordinate rapresentation. Type 1, top scan of the initial part

T1_I_BOT

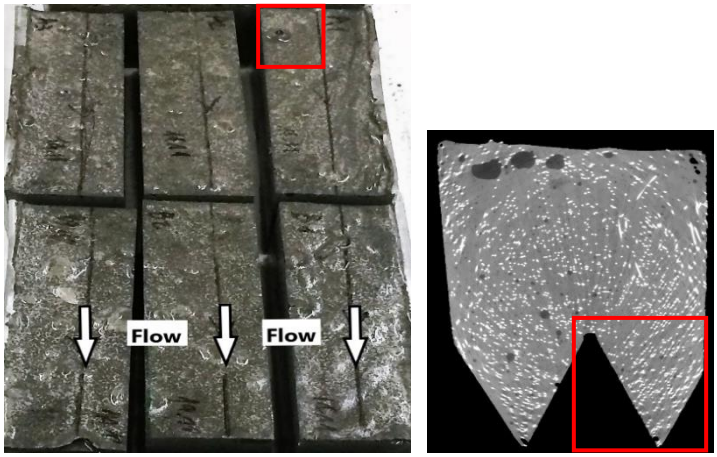

Figure 114 – Navigator of the ROI analyzed. Type 1, bottom scan of the initial part

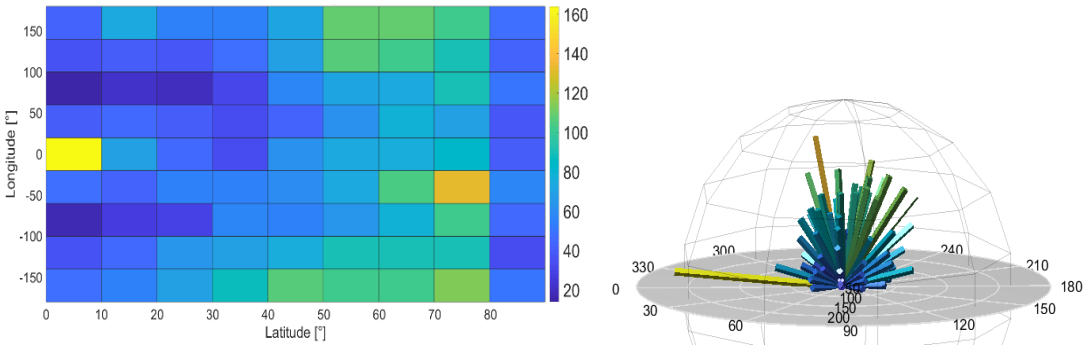

Figure 115 and 116 – Bivariate histogram of the fibers orientation in spherical coordinates and semi-spherical coordinate rapresentation. Type 1, bottom scan of the initial part

T1_I_LAT

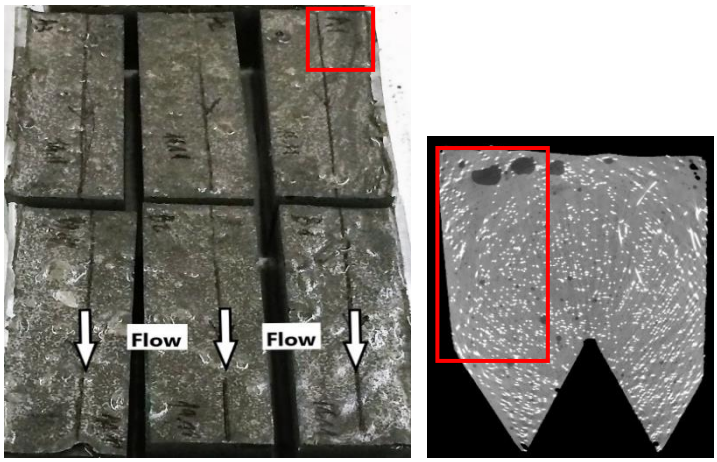

Figure 117 – Navigator of the ROI analyzed. Type 1, lateral scan of the initial part

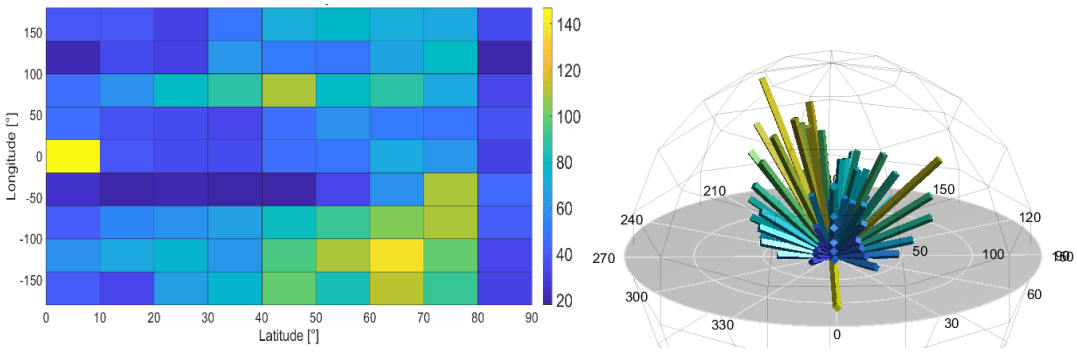

Figure 118 and 119 – Bivariate histogram of the fibers orientation in spherical coordinates and semi-spherical coordinate rapresentation. Type 1, lateral scan of the initial part

T1_C_TOP

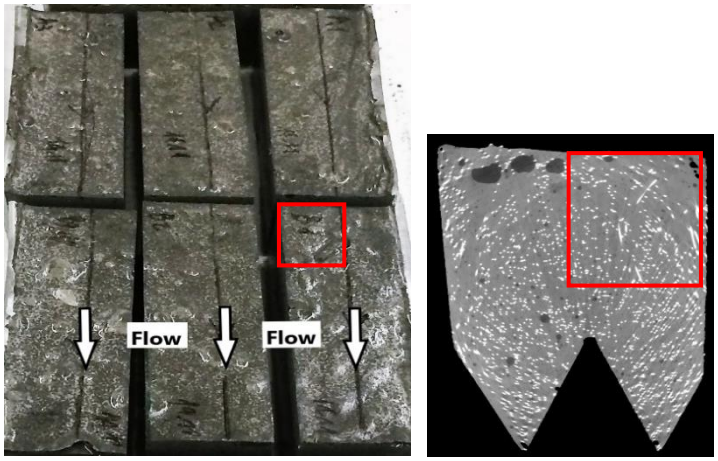

Figure 120 – Navigator of the ROI analyzed. Type 1, top scan of the central part

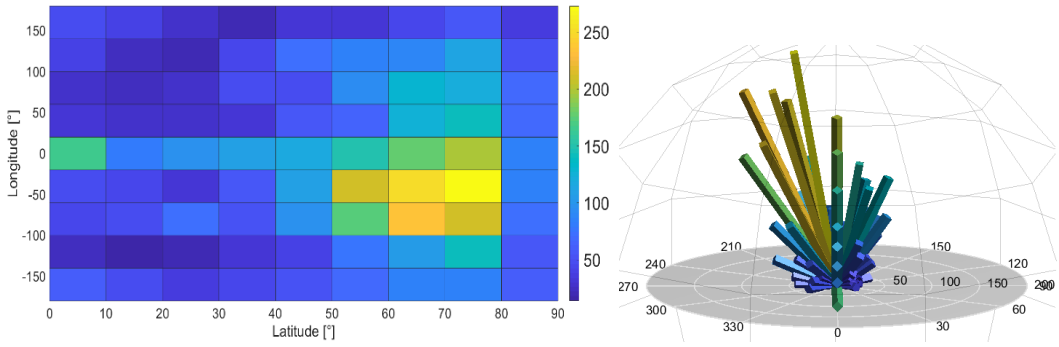

Figure 121 and 122 – Bivariate histogram of the fibers orientation in spherical coordinates and semi-spherical coordinate rapresentation. Type 1, top scan of the central part

T1_C_BOT

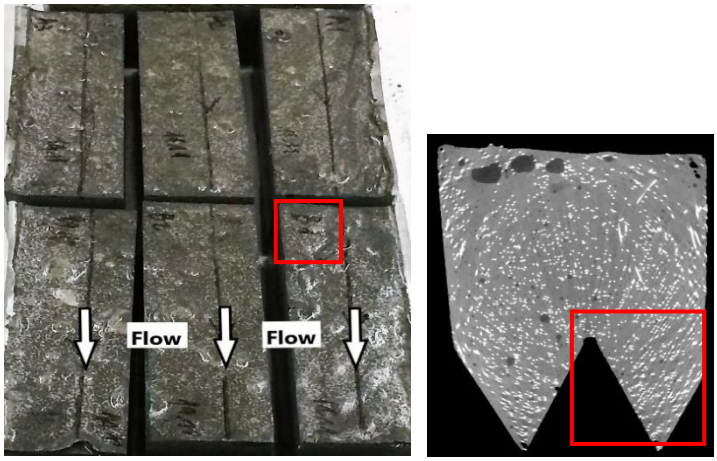

Figure 123 – Navigator of the ROI analyzed. Type 1, bottom scan of the central part

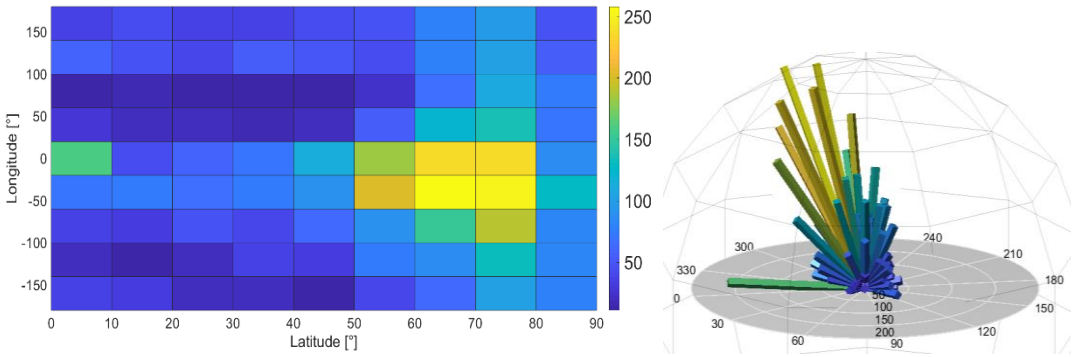

Figure 124 and 125 – Bivariate histogram of the fibers orientation in spherical coordinates and semi-spherical coordinate rapresentation. Type 1, bottom scan of the central part

T1_C_LAT

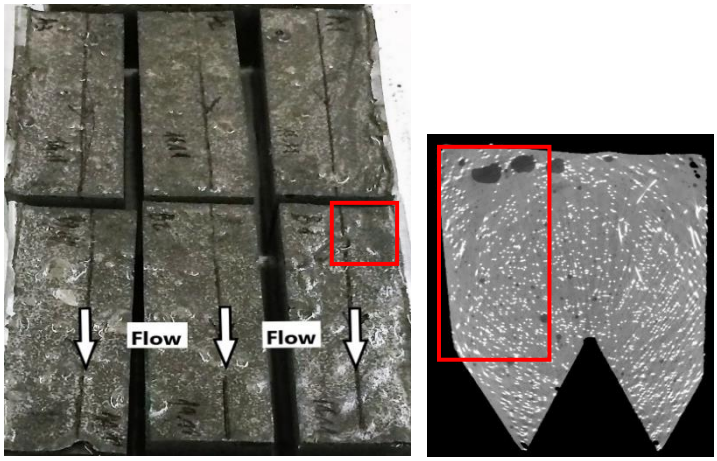

Figure 126 – Navigator of the ROI analyzed. Type 1, lateral scan of the central part

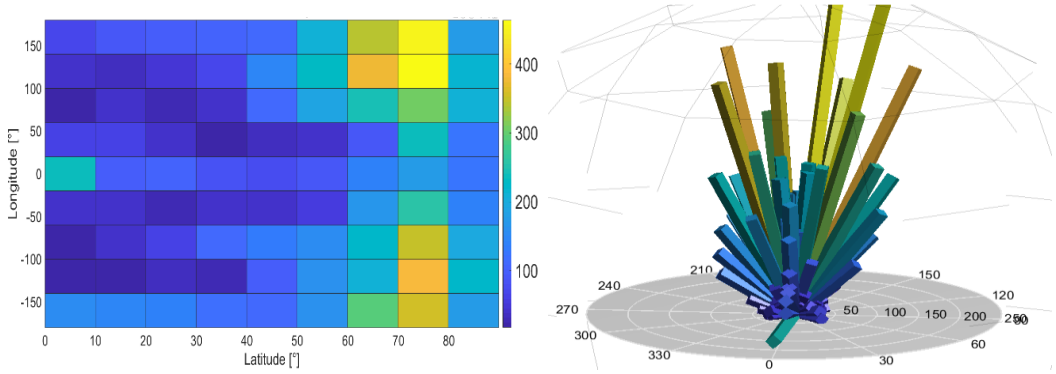

Figure 127 and 128 – Bivariate histogram of the fibers orientation in spherical coordinates and semi-spherical coordinate rapresentation. Type 1, lateral scan of the central part

T2_I_TOP

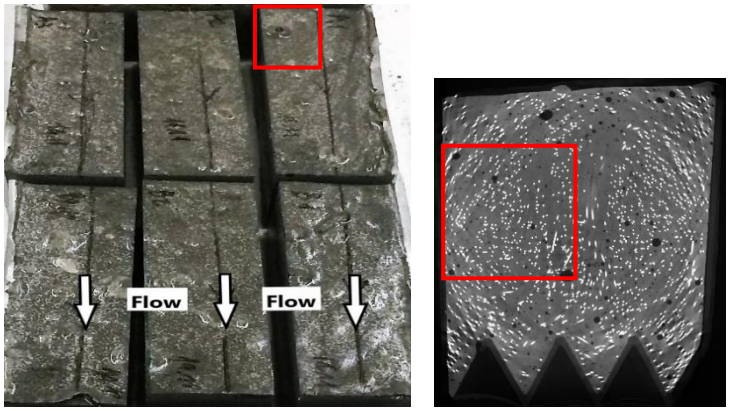

Figure 129 – Navigator of the ROI analyzed. Type 2, top scan of the initial part

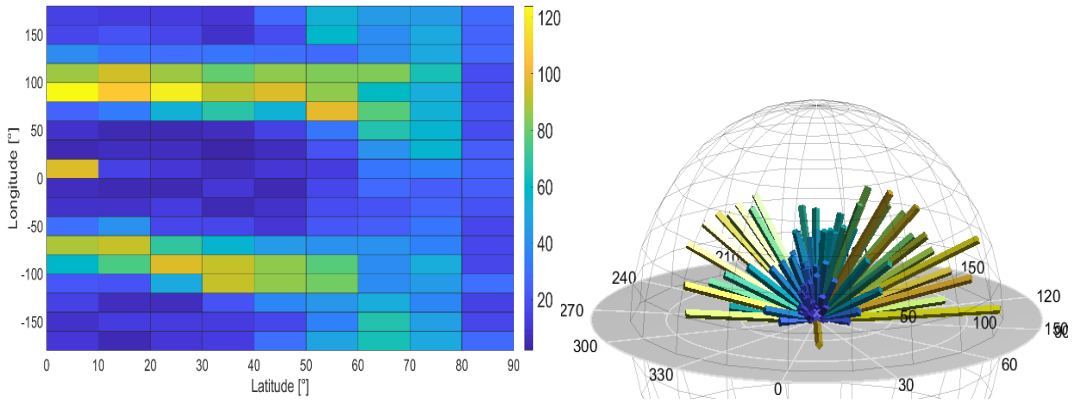

Figure 130 and 131 – Bivariate histogram of the fibers orientation in spherical coordinates and semi-spherical coordinate rapresentation. Type 2, top scan of the initial part

T2_I_BOT

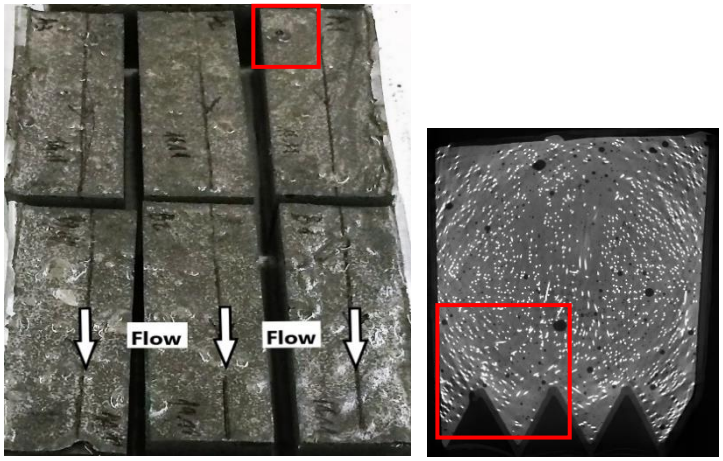

Figure 132 – Navigator of the ROI analyzed. Type 2, bottom scan of the initial part

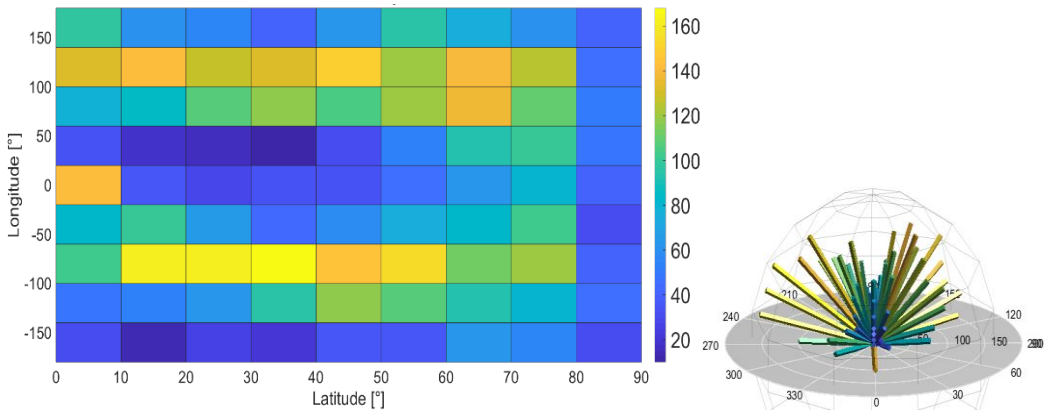

Figure 133 and 134 – Bivariate histogram of the fibers orientation in spherical and semi-spherical coordinate rapresentation. Type 2, bottom scan of the initial part

T2_I_LAT

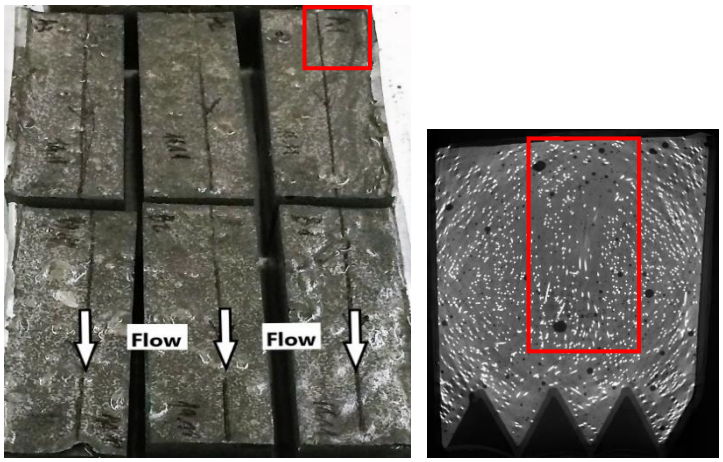

Figure 135 – Navigator of the ROI analyzed. Type 2, lateral scan of the initial part

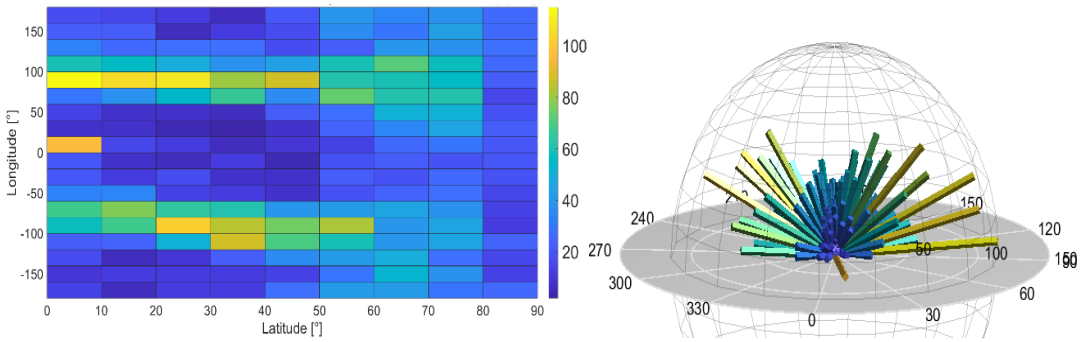

Figure 136 and 137– Bivariate histogram of the fibers orientation in spherical coordinates and semi-spherical coordinate rapresentation. Type 2, lateral scan of the initial part

T2_C_TOP

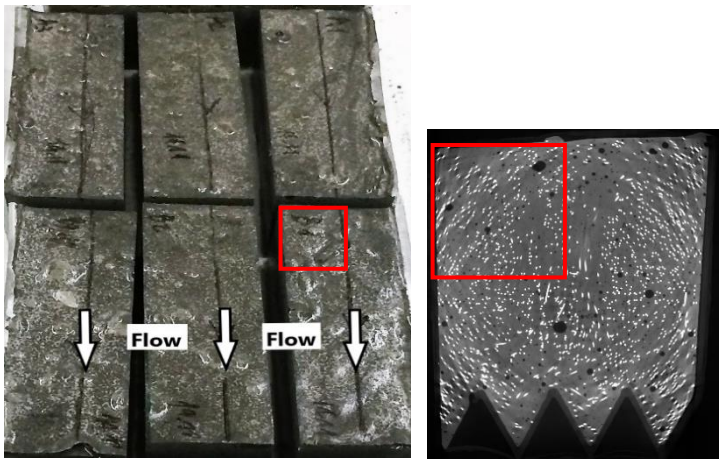

Figure 138 – Navigator of the ROI analyzed. Type 2, top scan of the central part

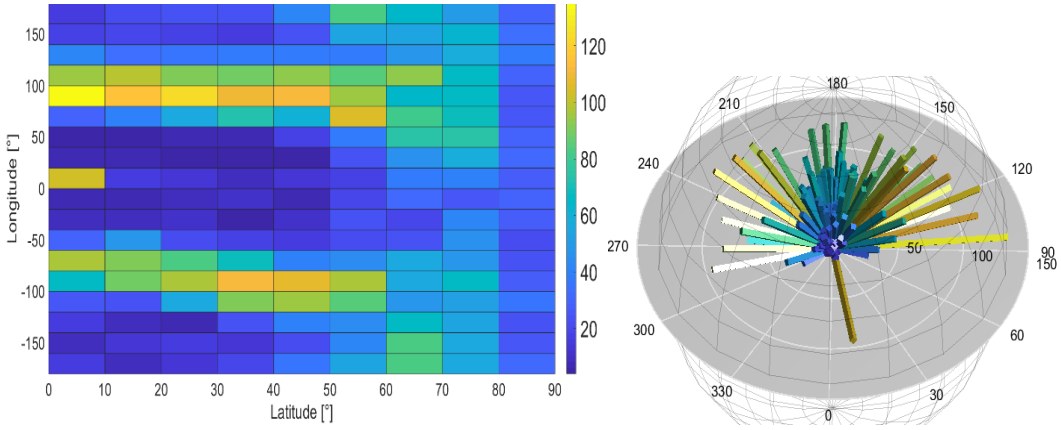

Figure 139 and 140 – Bivariate histogram of the fibers orientation in spherical coordinatesand semi-spherical coordinate rapresentation. Type 2, top scan of the central part

T2_C_BOT

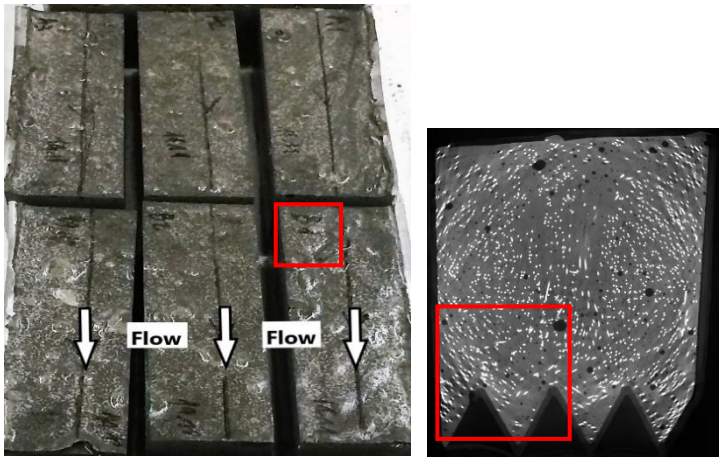

Figure 141 – Navigator of the ROI analyzed. Type 2, bottom scan of the central part

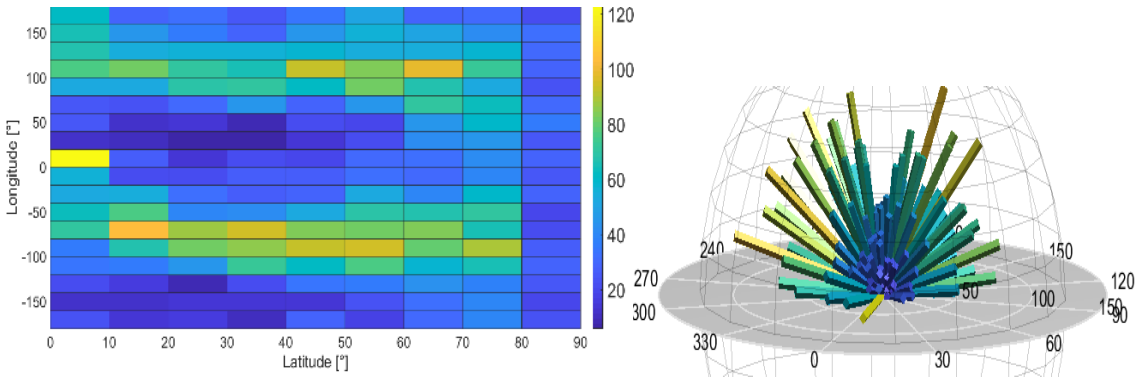

Figure 142 and 143– Bivariate histogram of the fibers orientation in spherical coordinatesand semi-spherical coordinate rapresentation. Type 2, bottom scan of the central part

T2_C_LAT

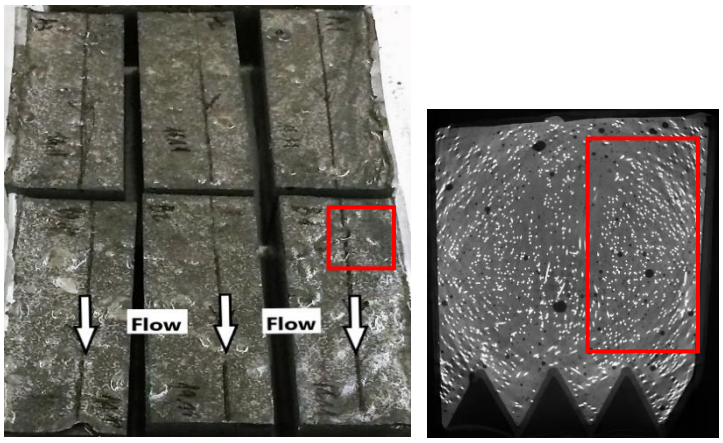

Figure 144 – Navigator of the ROI analyzed. Type 2, lateral scan of the central part

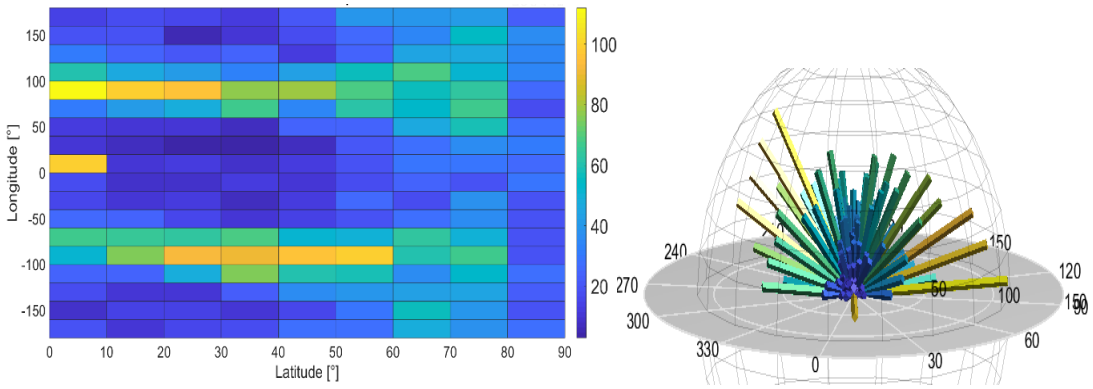

Figure 145 and 146 – Bivariate histogram of the fibers orientation in spherical coordinates and semi-spherical coordinate rapresentation. Type 2, lateral scan of the central part

T_REF_I_TOP

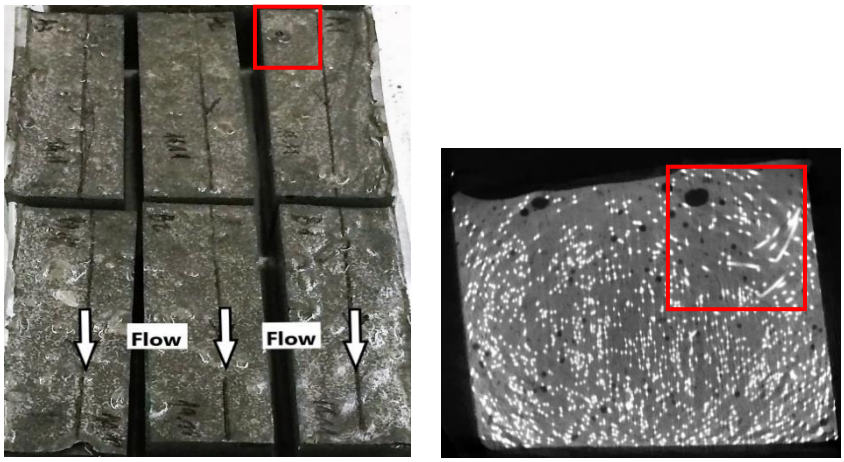

Figure 147 – Navigator of the ROI analyzed. Type reference, top scan of the initial part

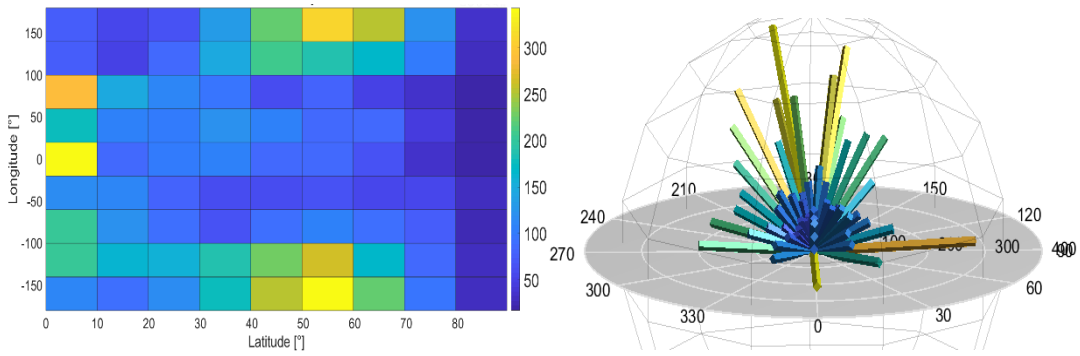

Figure 148 and 149 – Bivariate histogram of the fibers orientation in spherical coordinatesand semi-spherical coordinate rapresentation. Type reference, top scan of the initial part

T_REF_I_BOT

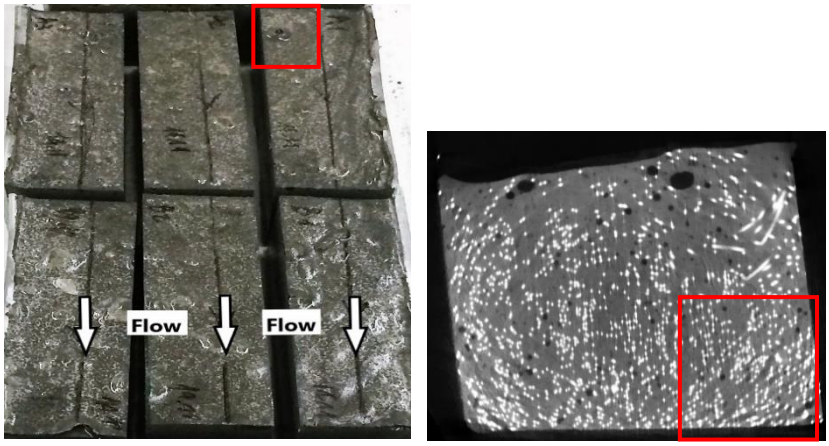

Figure 150 – Navigator of the ROI analyzed. Type reference, bottom scan of the initial part

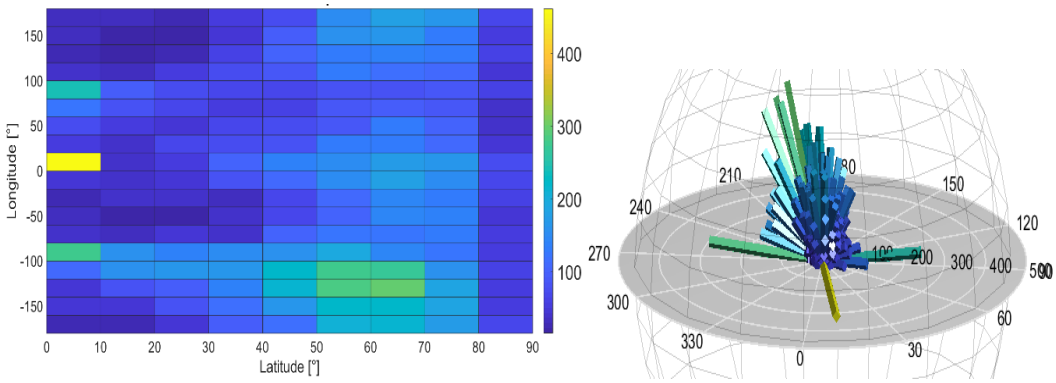

Figure 151 and 152– Bivariate histogram of the fibers orientation in spherical coordinatesand semi-spherical coordinate rapresentation. Type reference, bottom scan of the initial part

T_REF_I_LAT

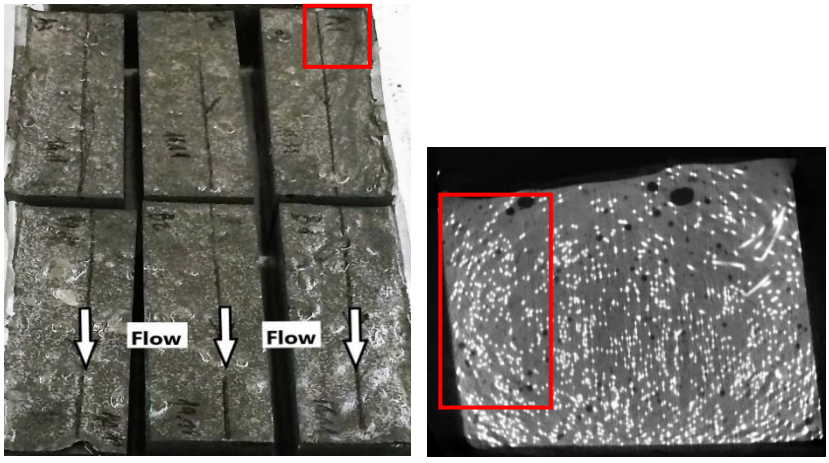

Figure 153 – Navigator of the ROI analyzed. Type reference, lateral scan of the initial part

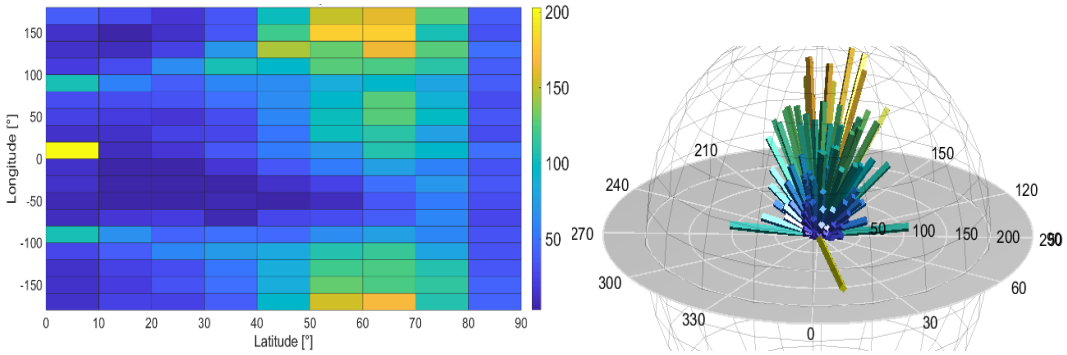

Figure 154 and 155 – Bivariate histogram of the fibers orientation in spherical coordinates and semi-spherical coordinate rapresentation. Type reference, lateral scan of the initial part

T_REF_C_TOP

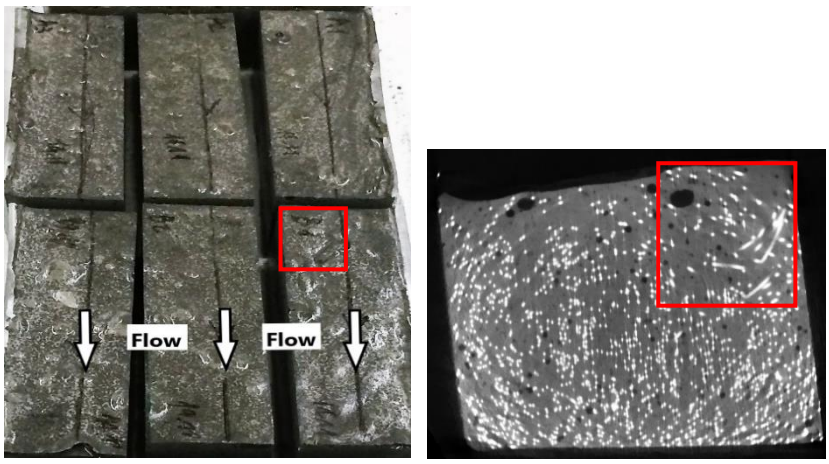

Figure 156 – Navigator of the ROI analyzed. Type reference, top scan of the central part

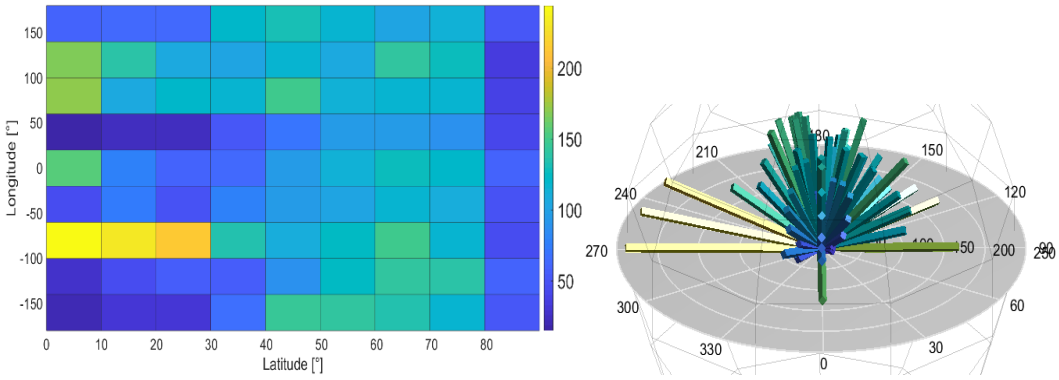

Figure 157 and 158 – Bivariate histogram of the fibers orientation in spherical coordinates and semi-spherical coordinate rapresentation. Type reference, top scan of the central part

T_REF_C_BOT

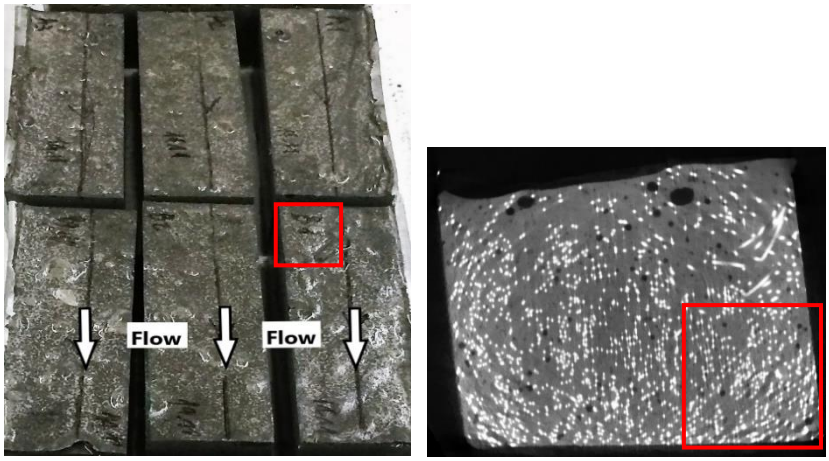

Figure 159 – Navigator of the ROI analyzed. Type reference, bottom scan of the central part

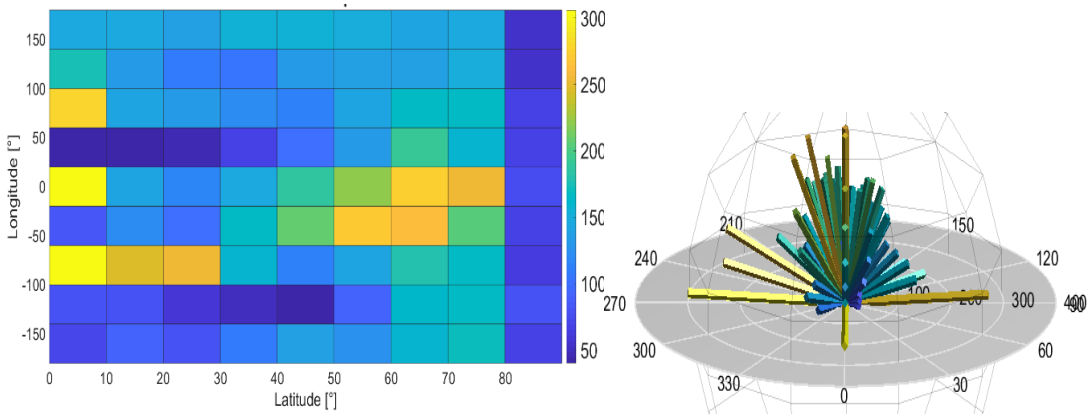

Figure 160 and 161 – Bivariate histogram of the fibers orientation in spherical coordinates and semi-spherical coordinate rapresentation. Type reference, bottom scan of the central part

T2_C_LAT

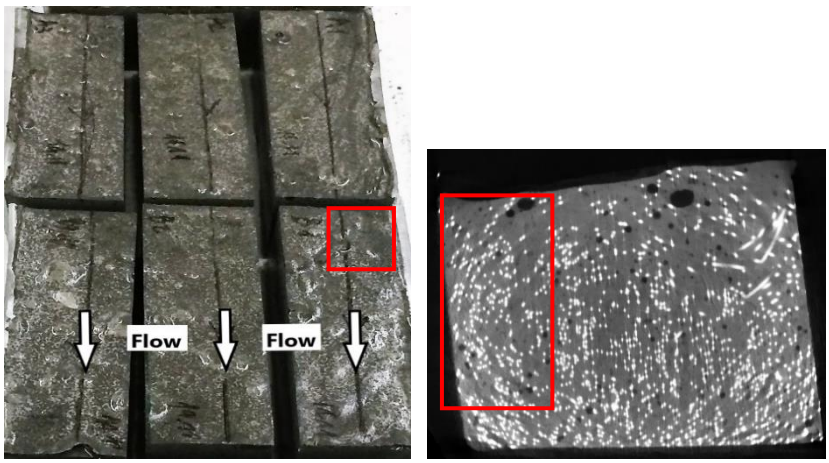

Figure 162 – Navigator of the ROI analyzed. Type reference, lateral scan of the central part

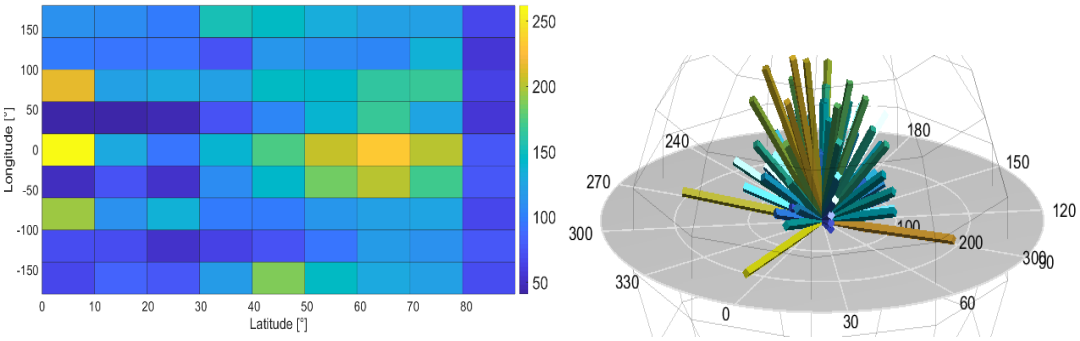

Figure 163 and 164 – Bivariate histogram of the fibers orientation in spherical coordinatesand semi-spherical coordinate rapresentation. Type reference, lateral scan of the central part

T_Y_S-S

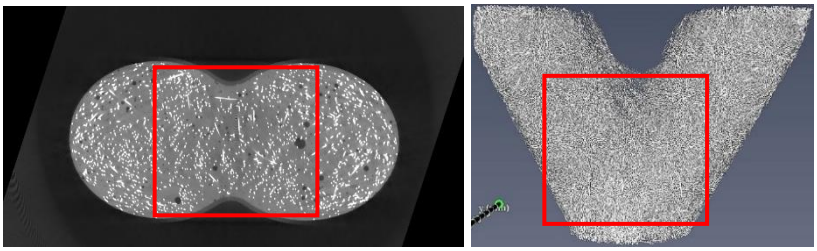

Figure 165 – Navigator of the ROI analyzed. Type "Y" casted from the holes at the same time, scan of central part

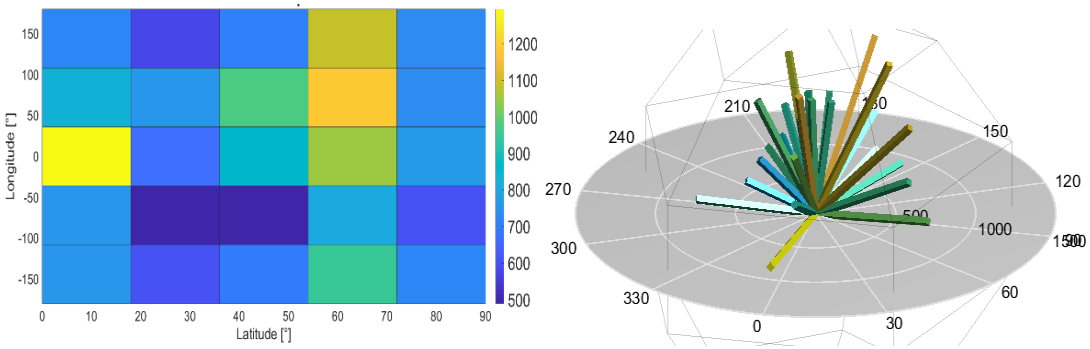

Figure 166 and 167 – Bivariate histogram of the fibers orientation in spherical coordinates and semi-spherical coordinate rapresentation. Type "Y" casted from the holes at the same time, scan of central part

T_Y_B-A

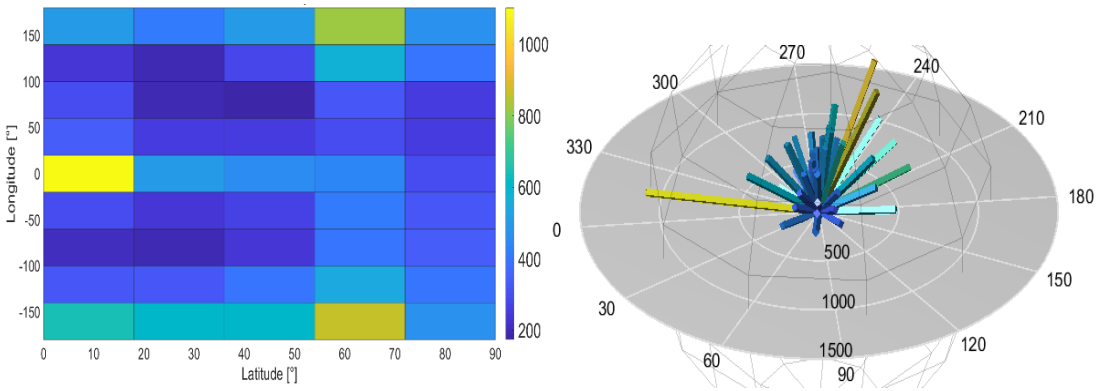

Figure 168 and 169 – Bivariate histogram of the fibers orientation in spherical coordinatesand semi-spherical coordinate rapresentation. Type reference, lateral scan of the central part Type "Y" casted from the holes at different same time, scan of central part

4.1.2 Results

An accurate and detailed analysis of fiber orientation has been carried out. Starting from the parallelepiped specimens (types 1 and 2) up to the "Y" shaped specimens. A comparison with a reference specimen was performed. Before listing the various results obtained it is necessary to clarify the reference system associated with a single fiber immersed in the cement matrix.

Spherical coordinates	X / Y	Reference system
θ: 0° / ϕ: 0°	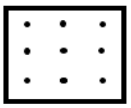	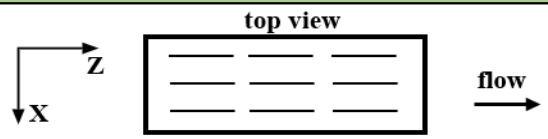
θ: 0° / ϕ: 90°	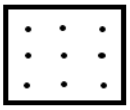	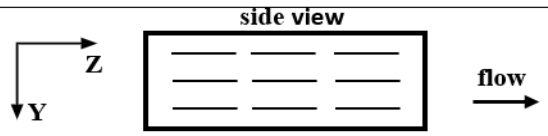
θ: 90° / ϕ: 0°		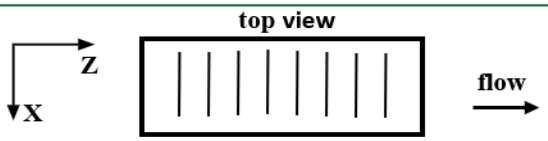
θ: 90° / ϕ: 90°	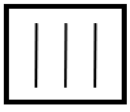	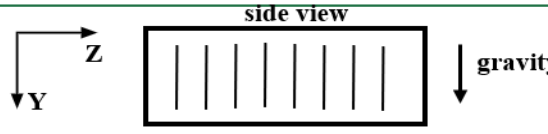

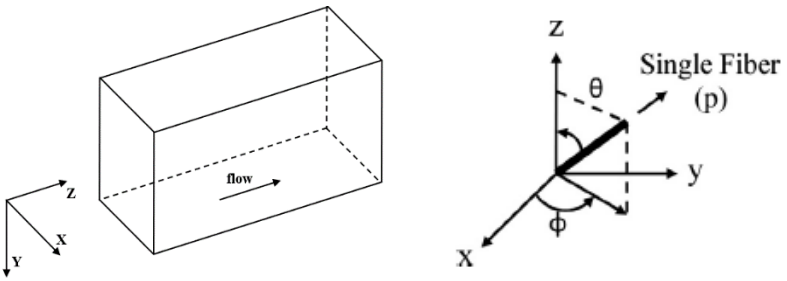

Figure 170 – Above, a table with the representation of the fibers in their orientation of the spherical values inside specimen from different views. Below, the reference system of a single fiber

The analysis on the orientation of the fibers gave the following results:

- in all the specimens, from the lateral edge towards the inside the θ angle decreases;
- in the reference specimen, from the side in which the casting is made towards the center (along the flow) the φ angle decreases;
- the notched edges increase the φ angle;
- from the side in which the casting is made towards the center (along the flow) the θ angle decreases. In the initial part, as expected, the fibers have an orientation influenced by the force of gravity. On the contrary, proceeding towards the center they are conditioned by the force of the flow (lower φ and lower θ);
- the boundaries induce an orientation due to the "wall effect" increasing the fiber efficiency factor (φ angle) [55];
- an error in the number of the particles with unacceptable volume (higher than 0.18mm3). Indeed, one fiber has a volume of 0.16 ± 0.2 mm^3 (10% error of production). Despite the maximum volume value of 0.9 mm^3, the calculation program has highlighted an average of fibers number acceptable.

  In relation to the number of fibers with a volume greater than the tolerable real (i.e. 0.18 mm^3) an error of 19% was found. This problem is due to the simplifications of the moment tensor analysis program in using the ellipsoid of inertia and using an image processing of false negative and false positive with the result of a smaller number of fibers with greater volume. This evidence has been already discussed in the previous chapter;
- In the “Y” specimens, the wall effect can be observed in the intersection of the two pipes. This was created once the concrete came into contact with the walls of the formwork (figure 171);

- In the “Y” specimens, fibers with low θ angle and low φ angle were detected (visible in the previous histogram bivariate);
- in the case of contemporary casting flows, the fibers have an orientation with high θ angle of 60° - 70° and high φ angle of 50° - 100°, while for the case with differentiated casting the fibers prefer θ angle of 60° - 70° and, a more pronounced, φ angle range of 150° - 180°. The φ angle has influenced a greater orientation in the experiment with differentiated flows;
- Finally, in the case of contemporary casting flows the orientation of the fibers is more influenced by the force of gravity than in the other case where the returning back of the flow contrasts the concrete flowing from the top.

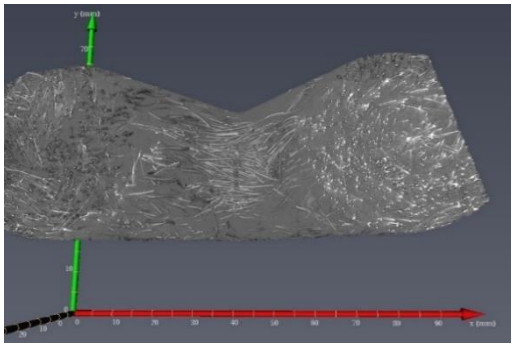

Figure 171– Rendering detail of the fibers near the intersection

4.2 Mechanical tests

4.2.1 Output data

The three-point flexural tests were performed and, as a result, the diagram of the applied load F vs. the deformation were produced. Deformation is expressed in terms of crack mouth opening displacement (CMOD) or mid-span deflection. The load-deformation curve consists of a first elastic behavior until reaching the first cracking, in most of the specimens it occurs at 2.5 mm of strain, then it proceeds to a plastic behavior [72][73]. The interest of the research is directed to the behavior before the first breaking. The load-peak value is taken into consideration and is correlated to a corresponding stress peak.

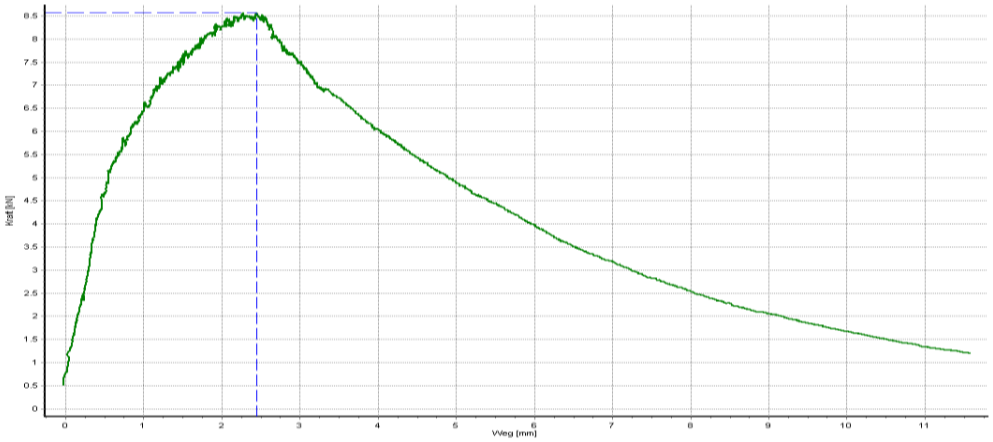

Figure 172 – Load-strain curve. On the y axis, the force applied in kN, on the x axis the strain (mm)

The advantage of using fibers inside the concrete leads to a "seaming" behavior of the cracks that are created. Consequently, the bending strength increases. In the HPFRC there is a plastic behavior greater than the unreinforced concrete, but in any way this is not comparable with the behavior of the reinforced concrete. The three-point flexural test was performed on six types of sample, excluding the reference sample. Due to the geometric shape of the cross-section, composed of a rectangular part and a triangular part, the inertia of the solid had to be calculated. Subsequently, starting from the maximum breaking load of the sample provided by the mechanical test it was possible to indirectly obtain the stress at the desired point. With the following equation:

$$\sigma_z = \frac{M}{J_x} y,$$

Equation 29 – Stress σ_z

In which the moment is provided by the equation 30:

$$M_{max} = PL / 4$$

Equation 30 – Moment M_{max}

Afterward, the tables with the stress values calculated on the base and on the tip of the tooth.

Stress value on the base of the tooth

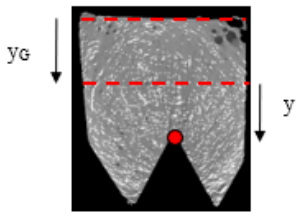

N° teeth	h_{tooth} (mm)	F (N)	Y_G (mm)	I (mm^4)	M (Nmm)	Y (mm)	σ (Mpa)	Average (Mpa)
REF	-	8570	16,00	316757	642750	16	32,47	
REF	-	9250	16,00	316757	693750	16	35,04	37,29
REF	-	11710	16,00	316757	878250	16	44,36	
6	15	11350	12,63	168387	851250	4	22,08	21,36
6	15	10610	12,63	168387	795750	4	20,64	
9	14	8820	12,83	174416	661500	5	19,62	20,68
9	14	9770	12,83	174416	732750	5	21,73	
12	9	11090	13,87	211755	831750	9	35,85	36,64
12	9	11580	13,87	211755	868500	9	37,44	
18	5	10370	14,79	251727	777750	12	37,74	
18	5	11500	14,79	251727	862500	12	41,85	38,83
18	5	10140	14,79	251727	760500	12	36,90	
24	4	15700	15,02	263318	1177500	13	58,03	
24	4	15540	15,02	263318	1165500	13	57,44	58,24
24	4	16027	15,02	263318	1202025	13	59,24	
36	3	10540	15,26	275595	790500	14	39,40	39,40

Table 14 – Stress value calculated on the tooth base for the different typologies of samples

Stress value on the tip of the tooth

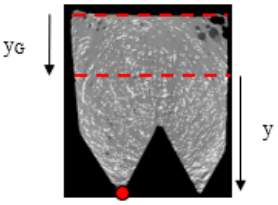

N° teeth	h_{tooth} (mm)	F (N)	Y_G (mm)	I (mm^4)	M (Nmm)	Y (mm)	σ (Mpa)	Average(Mpa)
REF	-	8570	16,00	316757	642750	16	32,47	
REF	-	9250	16,00	316757	693750	16	35,04	37,29
REF	-	11710	16,00	316757	878250	16	44,36	
6	15	11350	12,63	168387	851250	19,37	97,91	94,72
6	15	10610	12,63	168387	795750	19,37	91,52	
9	14	8820	12,83	174416	661500	19,17	72,72	76,63
9	14	9770	12,83	174416	732750	19,17	80,55	
12	9	11090	13,87	211755	831750	18,13	71,20	72,78
12	9	11580	13,87	211755	868500	18,13	74,35	
18	5	10370	14,79	251727	777750	17,21	53,19	
18	5	11500	14,79	251727	862500	17,21	58,98	54,73
18	5	10140	14,79	251727	760500	17,21	52,01	
24	4	15700	15,02	263318	1177500	16,98	75,92	
24	4	15540	15,02	263318	1165500	16,98	75,15	76,19
24	4	16027	15,02	263318	1202025	16,98	77,50	
36	3	10540	15,26	275595	790500	16,74	48,01	48,01

Table 15 – Stress value calculated on the tip of the tooth for the different typologies of samples

Stress value on the center line of the tooth

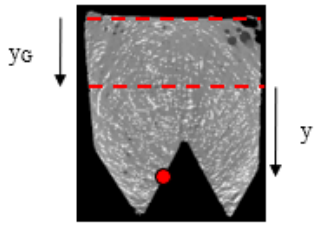

The base and maximum stress on the tip of the tooth have been calculated. To obtain an adequate comparison with the reference sample, it was decided to calculate the stress on the tooth center line. Point where, during each mechanical test, the breaking of the sample occurred.

N° teeth	h_{tooth} (mm)	F (N)	Y_G (mm)	I (mm^4)	M (Nmm)	Y (mm)	σ (Mpa)	Average (Mpa)	Increment (%)
REF	-	8570	16,00	316757	642750	16	32,47		
REF	-	9250	16,00	316757	693750	16	35,04	37,29	-
REF	-	11710	16,00	316757	878250	16	44,36		
6	15	11350	12,63	168387	851250	11,87	59,99	58,04	56%
6	15	10610	12,63	168387	795750	11,87	56,08		
9	14	8820	12,83	174416	661500	12,17	46,17	48,66	30%
9	14	9770	12,83	174416	732750	12,17	51,14		
12	9	11090	13,87	211755	831750	13,63	53,53	54,71	47%
12	9	11580	13,87	211755	868500	13,63	55,89		
18	5	10370	14,79	251727	777750	14,71	45,46		
18	5	11500	14,79	251727	862500	14,71	50,42	46,78	25%
18	5	10140	14,79	251727	760500	14,71	44,46		
24	4	15700	15,02	263318	1177500	14,98	66,98		
24	4	15540	15,02	263318	1165500	14,98	66,29	67,21	80%
24	4	16027	15,02	263318	1202025	14,98	68,37		
36	3	10540	15,26	275595	790500	15,24	43,71	43,71	17%

Table 16 – Stress value calculated in the center line of the tooth for the different typologies of samples

4.2.2 Results

In the previous data output a comparison between the stress values at the base of the tooth tip for the various sample types has been outlined. In general, an improvement in flexural strength for all notched sample types was shown. A dependency between the tooth height of the sample and the stress value was not found. On the contrary, higher strength values in samples with small tooth heights.

Type	H_{tooth} (mm)	F_m (N)	fcf_m (Mpa)	fcf_m (Mpa)	fcf_m (Mpa)	increment (%)
REF	-	9843	37,29	37,29	37,29	-
6	15	10980	94,72	21,36	58,04	56%
9	14	8540	76,63	20,68	48,66	30%
12	9	13723	72,78	36,64	54,71	47%
18	5	10670	54,73	38,83	46,78	25%
24	4	15756	76,19	58,24	67,21	80%
36	3	10540	48,01	39,4	43,71	17%

Table 17 – Comparison between different application of the stress point for the different typologies of samples. In yellow, the stress values on the tooth tip; in blue, the stress values on the tooth base; and in green, the stress values on the center line of the tooth

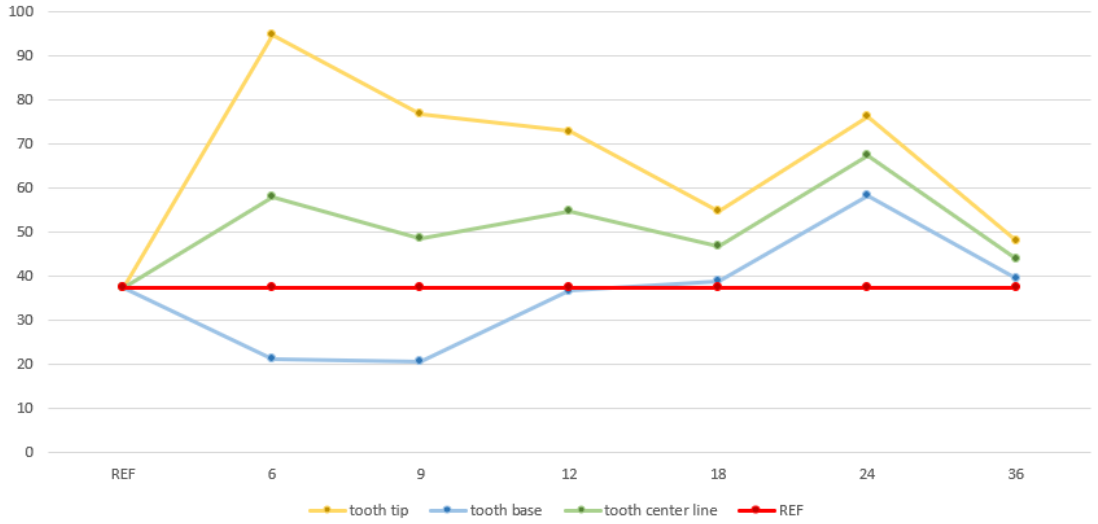

Table 18 – Comparison of stress values calculated at the base, at the tip and in the middle of the tooth, for the different tipologies of samples The red line is the reference stress value calculated in the centre of gravity

Detailed comments of results obtained above are listed as follow:

- the red line is the reference line of the parallelepiped sample. It has reached a flexural capacity of 37.29 Mpa;
- the yellow line is the line of stress values calculated on the tip of the tooth. It provides the maximum stress values in case the breaking occurs in that position;
- the blue line is the line of stress values calculated on the base of the tooth;
- the green line is a good compromise. In this case, the line of stress values calculated in the center line of the tooth shows a performance increase of the resistant capacity to bending;

- no relationship between the height of the fibers and the progress behavior of the stress values due to the fiber density phenomenon inside the matrix. Condensation of fibers at the base and in the center of the specimen was very high.
- Particular attention should be paid to the sample with 24 teeth. For this, there is an increase in flexural resistance with respect to the reference sample even with slight bevels edges of the formwork. This further justifies the effectiveness of the induced orientation of the fibers from the "wall effect";
- The lowest value of stress increase is given by the sample with a lower tooth height. This is due to the fact that the "wall effect" is no longer effective beyond that tooth height limit.

4.3 Fibers orientation for increment in the mechanical performance

In this cause-effect report the relationship that links fiber orientation with mechanical performance has been highlighted. Before starting, a series of considerations must be made before showing the link between peak stress and fiber orientation parameters. First of all, a different concentration of fibers predominantly accumulating on center line part of the specimen (fig. 183) and an orientation of the fibers parallel to the flow was evidenced. Furthermore, the fibers from the casting point characterized by a perpendicular orientation due to the force of gravity tend to a parabolic trajectory (fig. 184). Hence, the methods of casting the fresh state of the concrete are of considerable importance for the effects of the fibers.

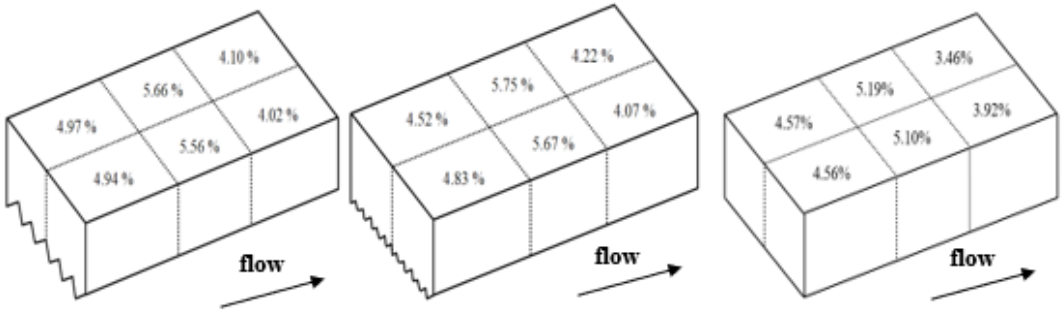

Figure 173 – Comparison of the local density of fibers in three typologies of specimen

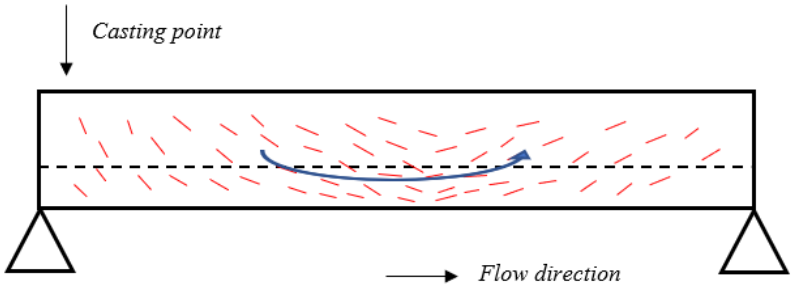

Figure 174 – Side view of the specimen with parabolic trend of the fibers along the flow

Another consideration is that the flow of the concrete, after having touched the base of the mold follows the speed of propagation of the matrix (fig. 185). In the central flow line, the fibers are oriented parallel to the flow direction. Therefore, in addition to the casting method also the geometric characteristics of the formwork influence the orientation of the fibers.

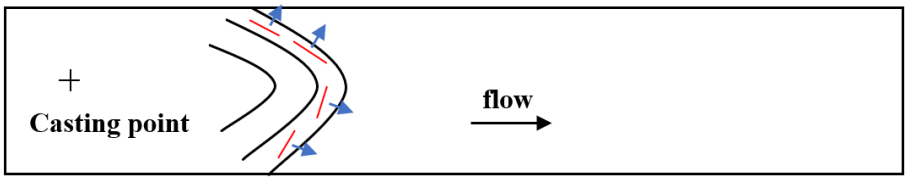

Figure 175 – Orientation of the fibers according to the flow

A case in which, the boundaries favor a precise fiber orientation is represented by the Y shaped specimens. In fact, near the connection of the two ends from which the cement is poured, an orientation of the fibers that follows the contour of the tubular geometric shape has been noted. As shown in the following figure, a practical example could be represented by a Y shaped fiber-reinforced beam in working condition subjected to loads. In this case, the link between fiber and matrix, the aspect ratio and the density of the fibers play a fundamental role because of the contribute to the resistant moment of the beam.

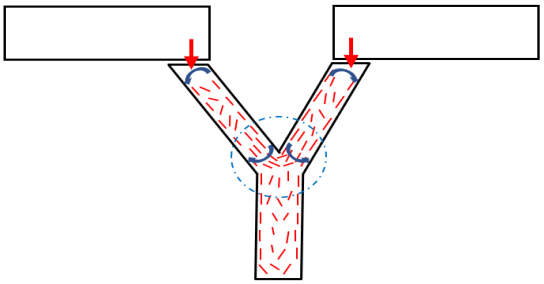

Figure 176 – Forces that are created on a Y-beam under applied loads

The correlation between the orientation of the fibres, evaluated as above, and the mechanical properties of the composite was possible by calculating suitable ‘‘toughness indicators’’ as a function of the COD, coherently with the prescriptions of Italian guidelines on the design of SFRC structures [75].

In the pre-peak regime, where multiple cracking has been observed in the central constant-bending moment region of the specimens, the length-scale governing the measured load–COD behaviour may be reliably assumed equal to the COD-measuring gauge length (COD = 300 mm). On the other hand, once the localization into a single crack has occurred, the fracture governing length scale can be assumed equal to the specimen depth h. Hence, has been possible to calculate the values of $f_{eq,1}$ and $f_{eq,2}$, related to post-cracking behavior.

It is by the way worth remarking that for the very thin structural elements herein dealt with, the second COD range may prove not adequate for a correct design-oriented identification of a tensile stress versus crack-opening law. This either because it is partially overlapping with the first one and may be not enough representative of the actual ductility and deformation capacity of the material. For this reason, post-cracking equivalent strengths corresponding to higher COD ranges, respectively, equal to 0.04 h ± 20% for $f_{eq\,(0.04h)}$ and 0.10 h ± 20% for $f_{eq\,(0.10h)}$, have been herein calculated. Following the table with all values calculated.

Specimen	$f_{eq,1}$ (N/mm^2)	$f_{eq,2}$ (N/mm^2)	$f_{eq\,(0.04h)}$ [Mpa]	$f_{eq\,(0.10h)}$ [Mpa]	$\sigma_{peak,\,mid}$ [Mpa]	peak [mm]	ε_{peak}
6	56,9	55,85	56,4	46,24	58,04	1,8	0,0060
12	53,63	52,36	50,4	45,14	54,71	2,2	0,0073
ref	36,21	35,47	34,15	26,95	37,29	2	0,0067

Table 19 – First cracking and post-cracking equivalent strengths at different COD calculated from load versis COD curves

Finally, two separate analyzes were obtained starting from the stress values comparing them with fiber volume fraction and fiber density.

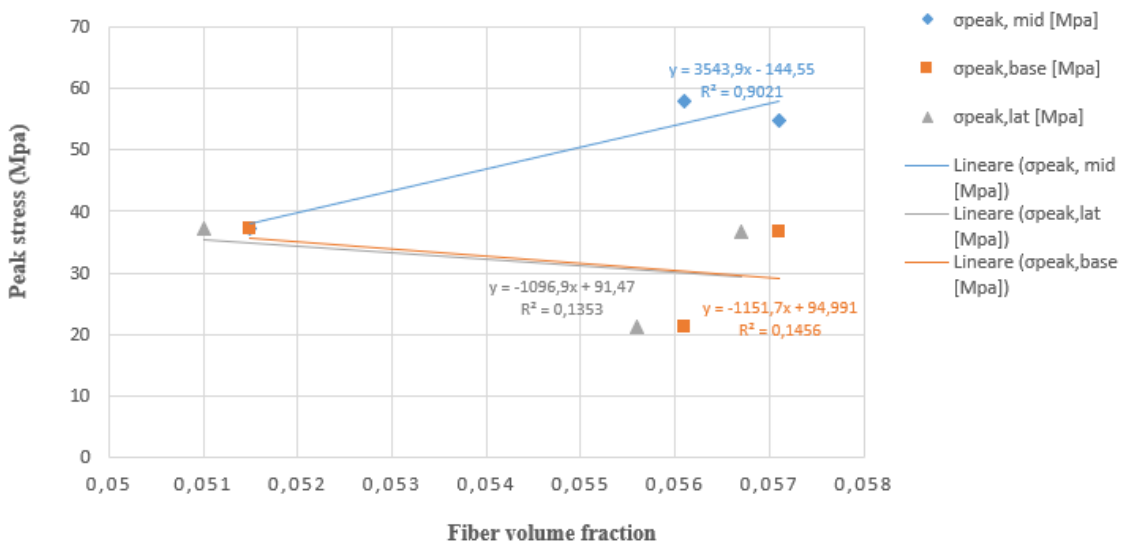

Table 20 – Peak stress vs fiber volume fraction

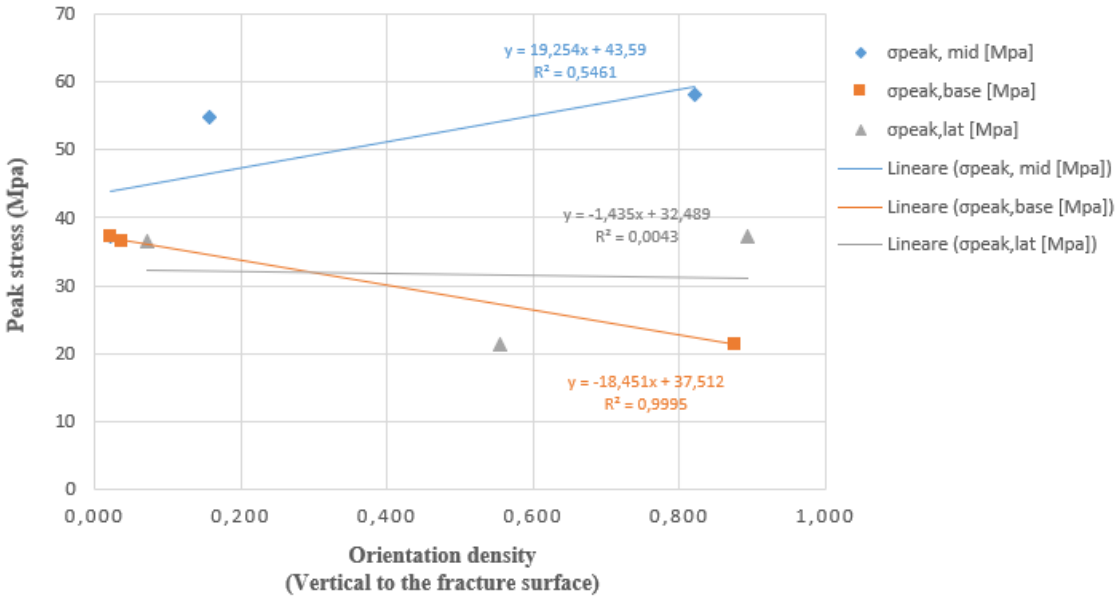

Table 21 – Peak stress vs orientation density

Analyzing the graphs obtained for three points in which the effort was calculated, we note a different mechanical performance of the sample examined according to the specific fiber orientation of an area. In the central-low zone of the sample, the density of the fibers, as previously seen, vertical to the fracture surface favors as an increase in stress peak increases. Moving towards the base of the tooth the fiber density decreases as the attached stress decreases. A similar but less evident speech concerns the orientation density of the fibers

approaching the end. In the graphs above, for the orientation density calculation the parameter p_x equal to sinθ cosΦ was used since the reference image plane is XY. The fiber analysis was performed through imagine analysis in the Amira-Avizo SW.

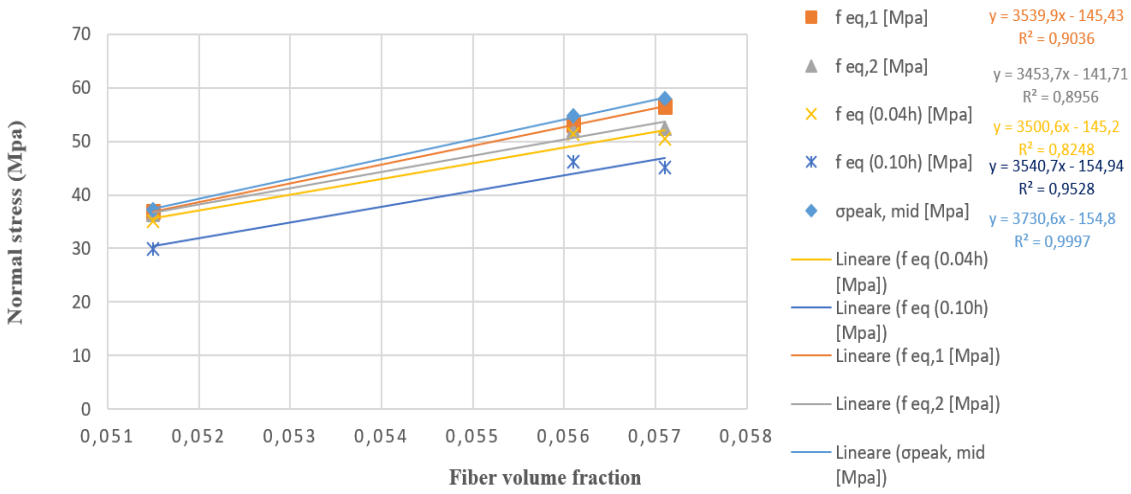

Table 22 – normal stress vs fiber volume fraction for different types of stress

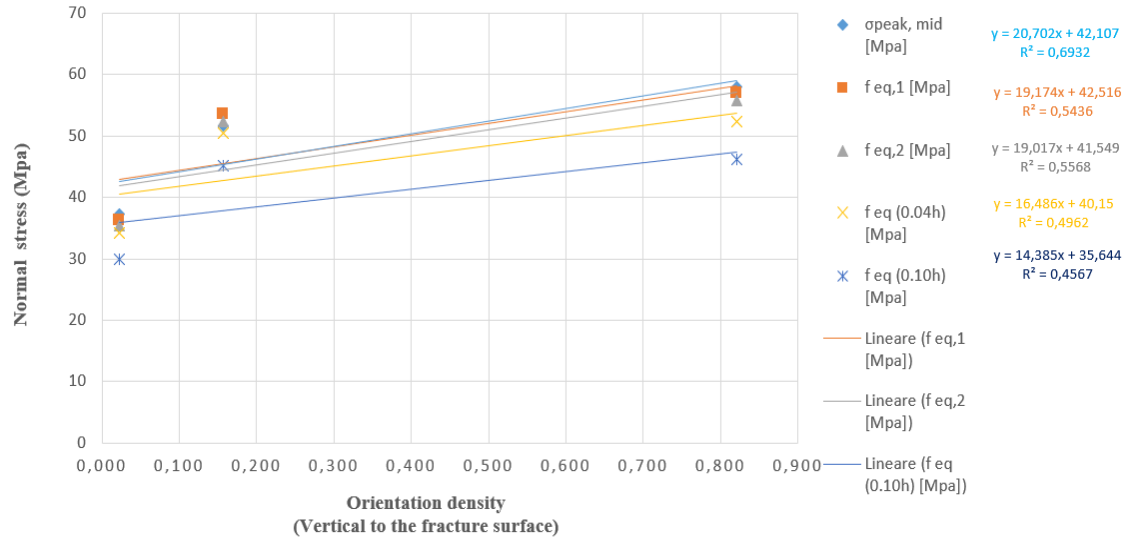

Table 23 – normal stress vs orientation density, vertical to the fracture for different types of stress

The orientation of the fibres significantly affects, as expectable, the mechanical performance of the fibre reinforced cementitious composites. This may be a discriminating factor to obtain a high mechanical performance of the material, such as for example deflection hardening or even reliable strain hardening behaviour, besides suitable selection of fibre type, fibre volume fraction, fibre–matrix bond and matrix characteristics.

This provides solid experimental evidence to the idea that the fresh state properties of the material and the casting process can be effectively tailored to orient the fibres along the direction of the tensile stresses. Values of the orientation factors could hence be governed in order to achieve the required mechanical performance. In addition, the casting and manufacturing process could also be suitably designed to obtain the optimized orientation through the aid of computational fluid dynamics modelling of fresh concrete flow [74].

CHAPTER 5 – CONCLUSIONS

Governing the dispersion and the orientation of fibres in concrete through a suitably balanced set of fresh state properties and a carefully designed casting procedure, is a feasible and cost-effective way to achieve a superior mechanical performance of fibre reinforced cementitious composites, which may be required by the intended application, even keeping the fibre content at relatively low values. The purpose of this work is to investigate how the fibers orientation induced through the 3D modeling of the formwork allows an increase in flexural strength in high-performance fiber-reinforced concretes. To achieve this, 16 toothed parallelepiped specimens, divided by tooth height category, with a total height of 32mm, width of 116mm and length of 360mm were casted. Moreover, this work was intended to verify the casting methods and the geometry (which was designed to "reproduce" the peculiarities of 3D printed elements). An analysis was carried out with AVIZO on the density of the fibers inside each sample. Starting from a theoretically percentage of fiber volume within the mix, with a nominal fiber dosage equal to 3.80 % by volume, after density analysis, an almost homogenous fiber volume fraction was found with an average equal to 4.73%. Higher values were found near the specimen edges, even 20% higher than the reference volume fractions were found, due to the effects on the flow of the cementitious matrix of the non-planar mould bottom. Hence, fiber orientation analysis was performed with a program written in java. The accuracy of the program was assessed in considering the shape of the fibers as a cylinder was obtained a histogram shape flatness and shape anisotropy degree. Then, a representation of the eigen vector of the fibers and a graph with the orientation of the fibers according to the angles in spherical coordinates was achieved. Angle θ is the angle between single fiber and Z axis, coinciding with the length of the specimen along the flow direction, while angle Φ is the angle between the projection

of the fiber on the xy plane, cross-section of the samples, and the X axis corresponding to the width of the specimen. As results, in all samples from the lateral edge to the center the angle θ to decreases, while along the flow towards the center the angle decreases. This is due to the "wall effect", more visible in the experience with the casting into Y shaped mold. In the initial part of the parallelepiped sample, as expected, the fibers had an orientation influenced by the force of gravity. On the contrary, proceeding towards the center they were conditioned by the force of the flow. Afterward, three-point flexural tests were performed and, as a result, the diagrams of the applied load F vs. deformation were produced. Deformation is expressed in terms of crack mouth opening displacement (CMOD) or mid-span deflection. In general, an improvement in flexural strength for all "saw-toothed" sample types was shown. A dependency between the tooth height of the sample and the stress value was not found. On the contrary, values were higher in samples with small tooth heights. In particular, for the reference sample a peak stress of 37.29 MPa was achieved, while for the other samples an increase in the stress calculated at 35% of the tooth was found. This work has shown that the orientation of steel fibres within a SFRC structural element can be effectively governed through a well-balanced fresh state performance, as obtainable by virtue of an appropriate mix composition, and a suitably designed casting process. The orientation of the fibres significantly affects, as expectable, the mechanical performance of the fibre reinforced cementitious composites. This may be a discriminating factor to obtain a high mechanical performance of the material, such as for example deflection hardening or even reliable strain hardening behaviour, besides suitable selection of fibre type, fibre volume fraction, fibre–matrix bond and matrix characteristics. Values of the orientation factors could hence be governed in order to achieve the required mechanical performance.

REFERENCES

[1] *"Rethinking reinforcement for digital fabrication with concrete"* _Domenico Asprone, Costantino Menna, Freek P. Bos, Theo A.M. Salet, Jaime Mata-Falcón, Walter Kaufmann Department of Structures for Engineering and Architecture, University of Naples Federico II, Department of the Built Environment, Eindhoven University of Technology, Department of Civil, Environmental and Geomatic Engineering (D-BAUG) - Institute of Structural Engineering (IBK), ETH Zürich. Cement and Concrete Research 2018 (25–36).

[2] *"Properties of 3D-printed fiber-reinforced Portland cement paste"* _M. Hambach, D. Volkmer, Cem. Concr. Compos. 2017 (62–70).

[3] *"Anisotropic mechanical performance of 3D printed fiber reinforced sustainable construction material"* B. Panda, S. Chandra Paul, M. Jen Tan, Mater. Lett. 2017 (146–149).

[4] *"Mega-scale fabrication by contour crafting"* _B. Khoshnevis, D. Hwang, K.-T. Yao, Z. Yah, Int. J. Ind. Syst. Eng. 1 2006 (301–320).

[5] *"Experimental exploration of metal cable as reinforcement in 3D printed concrete"* _F. Bos, Z. Ahmed, E. Jutinov, T. Salet, Basel 2017 (1313-1314).

[6] *"Additive Manufacturing Technologies. 3D Printing, Rapid Prototyping, and Direct Digital Manufacturing"* _I. Gibson, D. Rosen, B. Stucker, Springer, New York, 2015 (498).

[7] *"Vision of 3D printing with concrete — Technical, economic and environmental potentials"* Geert De Schutter, Karel Lesage, Viktor Mechtcherine, Venkatesh Naidu Nerella, Guillaume Habert, Isolda Agusti-Juan Magnel Laboratory for Concrete Research, Department of Structural Engineering, Ghent University, Belgium Institute of Construction Materials, TU Dresden, Dresden, Germany Dept. of Civil, Environmental and Geomatic Engineering, ETH, Zürich. Cement and Concrete Research 2018 (111–121).

[8] *"Anisotropic mechanical performance of 3D printed fiber reinforced sustainable construction material"* Biranchi Panda, Suvash Chandra Paul, Ming Jen Tan, Mater. Lett. 2017 (146–149).

[9] *"End-of-life consideration for hybrid material systems "*_I. Agustí-Juan, S. Zingg, G. Habert, G. De Schutter, N. De Belie, A. Janssens, N. Van Den Bossche (Eds), 14th International Conference on Durability of Building Materials and Components, RILEM Publications S.A.R.L, Ghent, Belgium, 2017 (377–378).

[10] *"Factors influencing labor productivity on construction sites"* _S.G. Naoum, Int. J. Product. Perform. Manag 2016 (401–421).

[11] *"Wertschöpfungsorientierte Planung und Realisierung von Bauvorhaben durch Lean Construction"* S. Haghsheno, M. Binninger, J. Dlouhy, Bauingenieur Jahresausgabe VDI Bautechnik 2015/2016 der Fachzeitschrift Bauingenieur, Springer-VDI-Verlag GmbH & Co. KG, Düsseldorf, S., 2016 (140–145).

[12] *"Understanding effects of BIM on collaborative design and construction: an empirical study in China"* _Y. Liu, S. Van Nederveen, M. Hertogh, Int. J. Proj. Manag. 35 2017 (686–698).

[13] *"Die Schalungstechnik, 1. Auflage, 1st ed."* _R. Schmitt, Ernst u. Sohn, Berlin, 2001.

[14] *"CONPrint3D: 3D concrete-printing as an alternative for masonry"* _R. Schach, M. Krause, M. Näther, V.N. Nerella, Bauingenieur 2017 (355–363).

[15] *"Productivity of digital fabrication in construction: cost and time analysis of a robotically built wall, Autom. Constr."* _B. García de Soto, I. Agustí-Juan, J. Hunhevicz, S. Joss, K. Grasser, G. Habert, 2018 (297–311).

[16] *"Building Design and Construction: Forging Resource Efficiency and Sustainable Development"* UNEP, United Nations Environment Programme, Sustainable Buildings and Climate Initiative (UNEP-

SBCI), Geneva, Switzerland, 2012.
[17] *"Additive construction: state-of-the-art, challenges and opportunities"* _N. Labonnote, A. Rønnquist, B. Manum, P. Rüther, Autom. Constr. 2016 (347–366).
[18] *"Environmental design guidelines for digital fabrication"* _I. Agustí-Juan, G. Habert, J. Clean. Prod. 2017 (2780–2791).
[19] *"Greenhouse gas emissions during the construction phase of a building: a case study in China"* J.Hong, G.Q. Shen, Y. Feng, W.S.-t. Lau, C. Mao, J. Clean. Prod. 2014 (249–259).
[20] *"Life-cycle assessment of office buildings in Europe and the United States"* _S. Junnila, A. Horvath, A.A. Guggemos, J. Infrastruct. Syst. 2006 (10–17).
[21] *"Additive Manufacturing: An Opportunity for Functional and Sustainable Constructions"*_ N. Labonnote, P. Rüther, International Conference on Sustainable Smart Manufacturing (S2M), Lisbon, 2016.
[22] *"Potential benefits of digital fabrication for complex structures: Environmental assessment of a robotically fabricated concrete wall"* _I. Agustí-Juan, F. Müller, N. Hack, T. Wangler, G. Habert, J. Clean. Prod. 2017 (330–340).
[23] *"Complex concrete structures: Merging existing casting techniques with digital fabrication,"* _ E.Lloret, A.R. Shahab, M. Linus, R.J. Flatt, F. Gramazio, M. Kohler, S. Langenberg, Comput. Aided Des. 2014 (40–49).
[24] *"Design, fabrication and testing of a prototype, thin-vaulted, unreinforced concrete floor"*_ A. Liew, D.L. López, T. Van Mele, P. Block, Eng. Struct. 2017 (323–335).
[25] *"Digital concrete: opportunities and challenges"* _T. Wangler, E. Lloret, L. Reiter, N. Hack, F. Gramazio, M. Kohler, M. Bernhard, B. Dillenburger, J. Buchli, N. Roussel, RILEM Tech. Lett. 1 2016 (67–75).
[26] *"Mesh Mould: An on Site, Robotically Fabricated, Functional Formwork, High Performance concrete and Concrete Innovation"* _N. Hack, T. Wangler, J. Mata-Falcón, K. Dörfler, N. Kumar, A.N. Walzer, K. Graser, L. Reiter, H. Richner, J. Buchli, W. Kaufmann, R.J. Flatt, F. Gramazio, M. Kohler, Conference at Tromsø, Norway, (2017).
[27] *"Reducing environmental impact by increasing the strength of concrete: quantification of the improvement to concrete bridges"* _G. Habert, D. Arribe, T. Dehove, L. Espinasse, R. Le Roy, J. Clean. 2012 (250–262).
[28] *"Largescale 3D printing of ultra-high performance concrete – a new processing route for architects and builders"* _C. Gosselin, R. Duballet, P. Roux, N. Gaudillière, J. Dirrenberger, M. Morel, Mater. Des. 100, 2016 (102–109).
[29] *"Sustainable application of construction and demolition waste: a review*" _ Oluwafemi O. Omotayo, Samuel Lambe Akingbonmire, Conference: 2017 Annual Conference of the School of Engineering & Engineering Technology (SEET), The Federal University of Technology, Akure, Nigeria.
[30] *"Large-scale 3D printing of ultra-high performance concrete – a new processing route for architects and builders"*_Gosselin C, Duballet R., Roux Ph., Gaudillière N., Dirrenberger J. and Morel Ph. Materials and Design (102–109) 2016.
[31] *"Concrete Construction Engineering Handbook"*_ Dr. Edward G.Nawy, P.E., C.Eng Distinguished Professor Rutgers – The State University of New Jersey, Romualdi, Batson and Mandel, Chapter 22, 2008.
[32] "*Studi preliminari finalizzati alla redazione di Istruzioni per l'impiego di calcestruzzi ad alte prestazioni"* Consiglio Nazionale delle Ricerche (CNR) CNR-DT 209-2012, Milano (2012).
[33] "*Materiali da costruzione"*, Luca Bertolini –Vol. 1, Città Studi editore, Milano (2010).
[34] "*I Calcestruzzi Fibrorinforzati – Produzione e applicazione"*, Galbiati A., Granzini L., Macchia C. –Maggioli Editore, Rimini (1996).
[35] *"Engineered steel fibers with optimal properties for reinforcement of cement composites"* _Naaman, A.E. J. Adv. Concr. Technol. 2003 (241–252).
[36] *"Study of magnetically driven concrete"* _Chen, J. Wang, J. Jin, W.L. Constr. Build. 2016 (53-59).
[37] *"Orientation of Steel Fibers in Magnetically Driven Concrete and Mortar"* _ Wen Xue, Ju Chen, Fang Xie and Bing Feng School of Civil Engineering and Architecture, Zhejiang University of Science and Technology and Department of Civil Engineering, Zhejiang University, Hangzhou, China January 2018.
[38] "*Recommendations for Design and Construction of High Performance Fiber Reinforced Cement Composites with Multiple Fine Cracks (HPFRCC)"* Japan Society of Civil Engineers Concrete Committee, Concrete Engineering Series (82), Japan, March 2008.
[39] "*Proposed classification of HPFRC composites based on their tensile response"* Naaman A. E.,

Reinhardt H. W. –Materials and Structures (2006), Vol. 38, pp. 547-555, Rilem 2006.
[40] "*High Performance Fiber Reinforced Cement Composites"* Naaman A. E. High-Performance Construction Materials: Science and Applications, Caijun Shi Y L Mo editors, Engineering Materials for Technological Needs, 2008, Vol. 1.
[41] "*Engineered Cementitious Composites – Can Composites Be Accepted as Crack-free Concrete?"*, Sahmaran M., Li V. C. –Concrete Materials (2010), Vol. 10, pp 1-8.
[42] "*Degradation kinetics and aging mechanisms on sisal fiber cement composite systems"* Almeida Melo Filho J., Silva F. A., Toledo Filho R. –, Cement & Concrete Composites (2013), Vol. 40, pp. 30-39
[43] "Interaction of particles in fibre reinforced concrete" _P.J.M. Barthos, C.W. Hoy, D.L. Marrs, D.J. Cleland (Eds.), Production Methods and Workability of Concrete, E&FN Spon, London, 1996 (451–461).
[44] *"3D Sand-Printed High Performance Fibre - Reinforced Concrete Hybrid Structures"* _Nicolas Ruffray, Mathias Bernhard, Felix Stutz, Neil Montague de Taisne_D-BAUG–Dept. of Civil, Environmental and Geomatic Engineering IfB – Institute for Building Materials Group PCBM – Physical Chemistry of Building Materials_06-06-2016.
[45] *"Ultra High Performance Concrete (UHPC*)" _M. Schmidt, E. Fehling, C. Geisenhanslüke University of Kassel, Germany_Schriftenreihe Baustoffe und Massivbau Structural Materials and Engineering SeriesKassel, Germany September 2004 (13-15).
[46] *"Superplasticizer effects on setting and structuration mechanisms of ultrahigh-performance concrete"*
V. Morin, F. Cohen Tenoudj, A. Feylessoufi und P. Richard_ Cement and Concrete Research_ January 2001.
[47] *"Fused Filament Fabrication/FFF – 3D Printing Simply Explained"* _Herb Weiner_All3DDP_31-08-2018.
[48] *"The mini-conical slump flow test: Analysis and numerical study"*_Adrien Bouvet, Elhem Ghorbel, Rachid Bennacer_Cement and Concrete Research 10 October 2010.
[49] *"Composite Materials: Science and Engineering"* _Krishan Kumar Chawla, Professor & Chairman, Dept. of Materials & Mechanical Engineering, The University of Alabama at Birmingham, USA_1998 (116-130).
[50] *"Micro-CT_Molecular Imaging I"* _Marc Kachelrieß_ Institute of Medical Physics (IMP), Friedrich-Alexander-Universit¨at Erlangen-N¨urnberg, Henkestraße 9, 91052 Erlangen, Germany 2008 (23-48).
[51] *"X-ray computed tomography of planetary materials: A primer and review of recent studies"* _ Romy D. Hanna, Richard A. Ketcham. Chemie Erde – Geochemistry_2017.
[52] *"The Mathematics of Medical Imaging: A Beginner's Guide* "_Feeman Timothy G, Springer Undergraduate Texts in Mathematics and Technology. Springer_2010.
[53] *"Physical Properties of Foods: Novel Measurement Techniques and Applications"* _Ignacio Arana_CRC Press Taylor & Francis Group 600 Broken Sound Parkway NW, Suite 300 Boca Raton, FL_2012.
[54] "*Spatial distribution of synthetic fibers in concrete with X-ray computed tomography"* _Amanda Bordelon, Jeffery R. Roesler_ Cement and Concrete Composites_October 2014.
[55] *"Simple tools for fiber orientation prediction in industrial practice"* _L. Martinie, N. Roussel Université Paris Est, Laboratoire Central des Ponts et Chaussées, Paris, France Cement and Concrete Research_2010 (993-1000).
[56] *"Avizo – 3D visualization framework"* _ Westenberg Peter, geoinformatics conference, visualization sciences Group, Mercury Computer Systems, Wernigeroder Str. 129, Duesseldorf_2008.
[57] "*A non-local algorithm for image denoising*. *Computer Vision and Pattern Recognition"* _A. Buades, B. Coll, J.-M. Morel, IEEE Computer Society Conference on Computer Vision and Pattern Recognition_San Diego CA (USA)_2005.
[58] *"On image denoising methods"* _Antoni Buades, Bartomeu Coll, Jean Michel Morel_2004.
[59] *"Particle finding in electron micrographs using a fast local correlation algorithm"* _Alan M. Roseman MRC Laboratory of Molecular Biology, Hills Road, Cambridge, CB2 2QH, UK_2002.
[60] *"Automated segmentation of electron tomograms for a quantitative description of actin filament networks"* Alexander Rigort, David Günther, Reiner Hegerl, Daniel Baum, Britta Weber, Steffen Prohaska, Ohad Medalia, Wolfgang Baumeister, Hans-Christian Hege_ Institute of Biochemistry, Department of Structural Biology and Department of Visualization and Data Analysis, Germany. University of Zurich, Department of Biochemistry, Ben-Gurion. Department of Life Sciences and the National Institute for Biotechnology in Negev, Israel2011 (135-138).
[61] "*Compensation of Missing Wedge Effects with Sequential Statistical Reconstruction in Electron Tomography"* Lassi Paavolainen, Erman Acar, Uygar Tuna, Sari Peltonen, Toshio Moriya, Pan

Soonsawad, Varpu Marjomäki, R. Holland Cheng, Ulla Ruotsalainen_ October 3rd_2014.

[62] *"Automated tracing of microtubules in electron tomograms of plastic embedded samples of Caenorhabditis elegans embryos"* _ Britta Weber, Garrett Greenan, Steffen Prohaska, Daniel Baum, Hans-Christian Hege, Thomas Müller-Reichert, Anthony A. Hyman, Jean-Marc Verbavatz, Journal of Structural Biology German_2011.

[63] *"Affordable image analysis using NIH Image/ImageJ"* _ Girish V, Vijayalakshmi A. Indian J Cancer 2004.

[64] *"Java in the High Performance Computing Arena: Research, Practice and Experience"* _Guillermo L. Taboada, Sabela Ramos, Roberto R. Exposito, Juan Tourino, Ramon Doallo Computer Architecture Group University of A. Coruna (Spain)_2011.

[65] *"Towards a Next-Generation Matrix Library for Java"* _Holger Arndt, Markus Bundschus, Andreas Nägele Published in 33rd Annual IEEE International Computer Software_ 2009.

[66] *"NAS Parallel Benchmarks Implementation for Message-Passing in Java"* _D.A. Mallo´n, G.L. Taboada, J. Tourino, R. Doallo, NPB-MPJ. 17th Euromicro Intl. Conf. on Parallel, Distributed, and Network-Based Processing (PDP'09), Weimar, Germany_ 2009 (181–190).

[67] *"The elastic theory of bending and the moment of inertia"* _H. Werner Rosenthal The Polytechnic of Central London UK H. Werner Rosenthal 1972

[68] *"To what extent does the fiber orientation affect mechanical performance?"* _Irem Sanal, Nilufer Ozyurt Zihnioglu Construction and Building Materials Department of Civil Engineering, Bogaziçi University, Istanbul, Turkey_2013.

[69] *"The ParaView Guide: A Parallel Visualization Application"* _Utkarsh Ayachit Kitware, inc USA 2015.

[70] *"The ParaView Tutorial"* _Kenneth Moreland, Sandia National Laboratories Sandia is a multiprogram laboratory operated by Sandia Corporation, a Lockheed Martin Company, for the United States Department of Energy's National Nuclear Security Administration under contract_ 2008.

[71] *"Effects of fibre location and density on the flexural toughness in FRC beams"* _ Mirko Manca, Daniela Ciancio, Phil Dight Conference: ACMSM24, At Perth_ december 2016.

[72] *"Statistical evaluation of three and four-point bending tests of FRC"* _Adam Podstawka, Marek Foglar, Vladimir Kristek CTU in Prague, Faculty of civil engineering, Department of concrete and masonry structures, Thákurova 7, 166 29, Prague, Czech Republic_2015 (37-43).

[73] *"Double edge wedge splitting (DEWS): an indirect tension test to identify post-cracking behaviour of fibre reinforced cementitious composites"* _ Marco di Prisco, Liberato Ferrara, Marco G. L. Lamperti Materials and Structures 2013 (1893-1916).

[74] *"High mechanical performance of fibre reinforced cementitious composites: the role of ''casting-flow induced'' fibre orientation"* Liberato Ferrara, Nilufer Ozyurt, Marco di Prisco Materials and Structures 2011 (109–128).

[75] "*Guidelines for the design, manufacturing and control of SFRC structures"* (in Italian)CNR-DT204 (2006)

[76] "*Correlation of tensile and flexural responses of strain softening and strain hardening cement composites"* Soranakom C, Mobasher B (2008) "*Correlation of tensile and flexural responses of strain softening and strain hardening cement composites"*. Cem Concr Compos (465–477)